Poincaré Waves and Kelvin Waves in a Circular Lake

by

Wentao Liu

A thesis
presented to the University of Waterloo
in fulfillment of the
thesis requirement for the degree of
Master of Mathematics
in
Applied Mathematics

Waterloo, Ontario, Canada, 2009

I hereby declare that I am the sole author of this thesis. This is a true copy of the thesis, including any required final revisions, as accepted by my examiners.

I understand that my thesis may be made electronically available to the public.

Abstract

When wind blows over a stratified lake an interface tilt is often generated, and internal waves usually appear after the wind stops. Internal waves in lakes are studied in many literatures, but most assume a hydrostatic pressure balance. In this thesis we discuss the internal Poincaré waves and Kelvin waves in a rotating, continuously stratified, flat-bottom, circular lake with fully nonlinear and non-hydrostatic effects.

An analytical solution is derived for the linearized system and it provides initial conditions used in the MIT General Circulation Model (MITgcm). This model is chosen due to its non-hydrostatic capability. Both Poincaré waves and Kelvin waves are considered. The analytical solution of the linear system is verified numerically when the wave amplitude is small. As the wave amplitude increases the waves become more nonlinear. Poincaré waves steepen and generate solitary-like waves with shorter wavelengths, but most of the energy contained in these waves is transferred back and forth between the parent wave and the solitary-like waves. Kelvin waves, on the other hand, steepen and lose their energy to solitary-like waves. The appearance of the solitary-like waves is not absolutely clear and higher resolution is required to clear up the details of this process. This conclusion agrees with de la Fuente et al. (2008) who discussed the internal waves in a two-layer model. Moreover, in the Kelvin waves case, unexpected small waves are generated at the side boundaries and travel inwards. The wave amplitude and wavelength of these spurious waves become smaller as the horizontal resolution increases. One possible reason to explain these waves is the use of square grids to approximate the circular lake.

Acknowledgements

Contents

List of Tables

List of Figures

x

Chapter 1

Introduction

1.1 Physical Processes in Lakes

Geophysical fluid dynamics studies naturally occurring, large-scale flows in the atmosphere, oceans and lakes. Most of these problems are at the large-scale end, where either the ambient rotation of the Earth or density differences (warm and cold air or water, fresh and saline water) or both assume some importance. In this respect, geophysical fluid dynamics comprises rotating-stratified fluid dynamics.

In this thesis, we are going to study the internal waves in lakes. Most lakes in temperate regions, due to solar heating and wind-mixing of surface layers, undergo a seasonal pattern, alternating between a two-layer stratification and complete mixing. As a result, the temperature and oxygen levels of the lakes change accordingly, which affects lives of both human beings and living creatures in water.

1.1.1 Thermal Processes

The greatest source of heat to lakes is solar radiation and most is absorbed directly by the water (Wetzel 2001). As solar energy is converted to internal energy (heat), lakes become thermally stratified. During summer time, lakes are warmer at the top and cooler at the bottom. The warm surface layer is called the epilimnion, and the cooler bottom layer the hypolimnion. The zone of rapid temperature decline in the water column from shallow to deep water is called the thermocline or the metalimnion. The thermocline is barrier to the mixing of surface and bottom water. Energy is required for mixing, which is primarily provided by wind in the absence of inflows and outflows. In the late summer and fall, the epilimnion begins to cool down. As the thermocline fades away, lakes are mixed and reach a uniform temperature. This destratification process is often called fall overturn (Davenport 2008). Since density of water has a maximum value at $4\,°\mathrm{C}$, once water cools below this value in winter a weak stratification can occur. Subsequently, mixing can occur in spring.

1.1.2 Oxygen Levels

Oxygen levels are vital to the survival of fish and other animals in lakes. During the stratification in summer, the thermocline creates a strong barrier to mixing, which isolates the hypolimnion from gas exchanges with the atmosphere. Without an influx of oxygen, the hypolimnion becomes depleted of oxygen due to bacterial decomposition of organic matter. A system with low DO (dissolved oxygen) saturation, in the range between 1% and 30% DO saturation, is called hypoxic. When DO is reduced to 0, it is called anoxic. Most fish cannot live below 30% DO saturation.

1.2 Geophysical Fluid Dynamics Models

There are many numerical models developed in the geophysical fluid dynamics field, for instance POM, DieCAST, ELCOM, SUNTANS, IGW, and MITgcm. The Princeton Ocean Model (POM) is a sigma coordinate, free surface, three-dimensional, primitive equation ocean model, which includes a turbulence sub-model. It was developed in the late 1970's by Blumberg and Mellor, with subsequent contributions from other people. The model has been used for modeling of estuaries, coastal regions and open oceans. The Dietrich Center for Air Sea Technology model (DieCAST) is a z coordinate, hydrostatic, partially implicit, fully conservative, primitive equation ocean and lake model, which was developed by Dietrich in 1994. The Estuary and Lake Computer Model (ELCOM) is a z coordinate, hydrostatic, three-dimensional model used for predicting the velocity, temperature and salinity distribution in natural water bodies subjected to external environmental forcing such as wind stress, surface heating or cooling. It was developed by Hodges in 1997 at the Centre for Water Research, University of Western Australia. The Stanford Unstructured Nonhydrostatic Terrain-following Adaptive Navier-Stokes Simulator (SUNTANS) is a z coordinate, non-hydrostatic, unstructured-grid, parallel, three-dimensional, coastal ocean simulation tool that solves the Navier-Stokes equations under the Boussinesq approximation with a large-eddy simulation of the resolved motions. The formulation is based on the method outlined by Casulli in his 1999 papers. The Internal Gravity Waves model (IGW) is a two-dimensional, non-linear, incompressible and non-hydrostatic numerical model, using the Boussinesq and traditional f-plane approximations. The model uses a finite volume method based on the second-order projection technique developed by Bell et al. (1989a) and extended to stratified flows by Bell and Marcus (1992) and to quadrilateral grids by Bell et al. (1989b). The description of the model can be found in Lamb (1994). The MIT General Circulation Model (MITgcm) is a numerical model for studying both the ocean and atmosphere developed by Marshall, Hill, Adcroft along with others in 1997 at MIT. It has a non-hydrostatic capability and is thus able to simulate fluids at a wide range of scales. Because of these aspects of the model, we select MITgcm to perform the numerical simulations in this thesis. More details on MITgcm are presented in following chapters.

1.3 Internal Waves in Lakes

When wind blows over a stratified lake, an interface tilt is usually generated, causing the thermocline to rise upwind and fall downwind (Monismith 1986). When the wind stops blowing, the thermocline is released and adjusted through the generation of basin-scale waves which may then steepen nonlinearly and transfer energy to waves of higher frequencies and shorter wavelengths. Thereafter, internal waves are often generated. The internal waves are responsible for mixing and redistribution of nutrients, pollutants, and sediments in lakes (Ostrovsky et al. 1996; Imberger 1998). Internal waves in lakes are studied in many literatures, but most assume a hydrostatic pressure balance, which is only good for long waves with low frequencies. When the Earth's rotation is negligible, the internal waves in a non-rotating water body due to a surface shear stress were studied by Spigel and Imberger (1980), who extended the earlier analytic solution developed by Heaps and Ramsbottom (1966). The degeneration of internal waves was described by Fedorov and Melville (1995), Horn et al. (2001), and Boegman et al. (2005). In Horn et al. (2001), by assuming a simple two-layer model and comparing the timescales over which of these degeneration mechanism act, regimes are defined in which particular processes are expected to dominate. We will revisit the regimes plot in section 4.2.

The Earth's rotation starts to affect internal gravity waves when lake dimension approaches the internal Rossby radius of deformation, defined by c/f, where c is the non-rotating phase speed and f is the Coriolis parameter. The effect of rotation is to change the character of basin-scale internal waves, such that the crests begin to propagate around the boundaries of the lake, instead of across the lake center, as in the non-rotating case. When the gravity waves are affected by the rotation, they are called Poincaré waves or inertia-gravity waves. When the gravity waves are trapped against a topographic boundary such as a coastline, in the presence of rotation a new type of wave appears, namely Kelvin waves. The amplitude of these waves decays away from the boundary. The evolution of Poincaré waves and Kelvin waves is modified by nonlinear wave steepening (Bennett 1973; Farmer 1978), topography (Romea and Allen 1984; Thorpe 1998), wave-wave interaction (Phillips 1977), and dissipation (Hopfinger 1987; Ivey and Imberger 1991).

When the Earth's rotation is considered, the linear solution for a uniform, constant wind imposed suddenly over a circular homogeneous rotating lake with a flat bottom was derived by Csanady (1968). Beletsky et al. (1997) studied the problem of internal Kelvin waves and coastal upwelling both in a flat bottom and a parabolic bottom basin using POM and DieCAST. In the case of the flat bottom basin, the dynamical response to light wind forcing is a small amplitude internal Kelvin wave. For strong wind forcing, the thermocline intersects the surface (full upwelling) and a strong surface thermal front appears. After the wind ceases, the edges of this thermal front propagate cyclonically around the lake similar to an internal Kelvin wave. Hodges et al. (2000) used ELCOM to study Lake Kinneret, Israel. They provided a detailed description of a turbulence closure for the vertical Reynolds stress terms and vertical turbulent transport using a 3D mixed-layer model parameterized on

wind and shear energy fluxes instead of the conventional eddy viscosity/diffusivity assumption. Stocker and Imberger (2003) investigated the response of a stratified rotating lake to the release of a linearly tilted interface. Energy partitioning is studied as a function of the Burger number S (relative importance of stratification versus rotation), showing the dominance of a geostrophic component over the wave field for low S. For a stratified lake, a common model used is to approximate the stratification as two, three or more layers in Mortimer (1952), Spigel and Imberger (1980), Monismith (1985), and Munnich et al. (1992). de la Fuente et al. (2008) studied the evolution of internal waves in a two-layer, rotating, circular lake under nonlinear and weak non-hydrostatic effects. It is shown that a Kelvin wave evolves by imparting energy primarily to submodes of the parent cyclonic wave by steepening and to solitary-type waves. By contrast, a Poincaré wave is shown to evolve without shedding much of its energy to other waves, and only a small fraction of the wave energy goes to other submodes, and this is not lost from the parent wave but rather is periodically transferred back into the parent wave. In this thesis, we are going to investigate the internal waves in a flat bottom, continuously stratified, rotating, circular lake under fully nonlinear and non-hydrostatic effects.

1.4   Thesis Structure and Goals

Chapter 2 presents some theoretical background for the governing equations used in this thesis and for gravity waves. In chapter 3, the analytical solution in the linear theory of the governing equations is derived. We assume that the wave solution is propagating around the lake in the θ angular direction. After substituting the proposed solution into the governing equations, the method of separation of variables is applied, which introduces an constant C. Different signs of C lead to two cases to investigate: $C > 0$ giving internal Poincaré waves and $C < 0$ giving internal Kelvin waves. When $C = 0$ there appears to be no solutions of the linear problem. The numerical model is set up in MITgcm in chapter 4. One goal of applying the numerical model is to verify the analytical solutions we have obtained in the linear system, and the other is to investigate the nonlinear and non-hydrostatic properties of the waves. Chapter 5 and 6 present the results of numerical simulations, conclusions, and future works. The analytical solution for the linear system is verified in the "quasi-linear" setup (details in chapter 5). When the amplitude of the waves increases, nonlinear and non-hydrostatic effects are studied. Poincaré waves steepen and form solitary-like waves with shorter wavelengths, but most energy contained in these waves is transferred back and forth between the parent wave and the solitary-like waves. Kelvin waves, on the other hand, steepen and lose their energy to solitary-like waves which are formed after the steepening. This conclusion agrees with de la Fuente et al. (2008).

Chapter 2

Theoretical Background

In this chapter, the governing equations of geophysical fluids motion are briefly derived using several conservation laws, and simplified using the Boussinesq approximation. Surface and internal gravity waves are introduced in section 2.2, along with two special waves, namely Poincaré waves and Kelvin waves.

2.1 Governing Equations

In this section, the governing equations of geophysical fluids motion are briefly derived using several conservation laws, and simplified using the Boussinesq approximation. Later on, three types of boundary conditions are stated. This chapter is mainly based on Cushman-Roisin (1994) and Kundu and Cohen (2004) as references.

2.1.1 Mass Conservation

As a material element moves, its mass remains constant, while its volume may change, which leads to change of density. The equation relating the rate of change of density to the fluid motion is

$$\frac{\partial \rho}{\partial t} + \nabla \cdot (\rho \mathbf{u}) = 0, \tag{2.1}$$

where ρ is the density of the fluid (in kg/m^3), and $\mathbf{u} = (u, v, w)$ is the velocity vector (in m/s), and and $\nabla = (\partial/\partial x, \partial/\partial y, \partial/\partial z)$ is the divergence operator. This equation is often called continuity equation. Given the definition of material derivative D/Dt, which is the rate of change while moving along the fluid,

$$\frac{D}{Dt} = \frac{\partial}{\partial t} + \mathbf{u} \cdot \nabla, \tag{2.2}$$

the continuity equation can be rewritten as

$$\frac{1}{\rho}\frac{D\rho}{Dt} + \nabla \cdot \mathbf{u} = 0.$$ (2.3)

2.1.2 Momentum Conservation

Newton's second law of motion states that mass times acceleration equals the sum of the forces. Per unit volume, we have the following momentum budget in each direction,

$$\rho\left(\frac{Du}{Dt} - fv\right) = -\frac{\partial p}{\partial x} + \mu\nabla^2 u,$$ (2.4)

$$\rho\left(\frac{Dv}{Dt} + fu\right) = -\frac{\partial p}{\partial y} + \mu\nabla^2 v,$$ (2.5)

$$\rho\frac{Dw}{Dt} = -\frac{\partial p}{\partial z} - \rho g + \mu\nabla^2 w,$$ (2.6)

where f is the Coriolis parameter (in rad/s), p is the pressure (in Pa), μ is the dynamic viscosity (in kg/(m· s)), and ∇^2 is the Laplacian defined by

$$\nabla^2 = \frac{\partial^2}{\partial x^2} + \frac{\partial^2}{\partial y^2} + \frac{\partial^2}{\partial z^2}.$$ (2.7)

Here we assume the fluid is a Newtonian fluid, so we can use the viscous terms above. Also the traditional approximation has been applied in which only the vertical component of the Earth's angular velocity is used.

Currently, we have four equations (one continuity equation and three momentum equations) along with five unknowns (u, v, w, ρ, and p). To form a closed system of equations, we need one more equation.

2.1.3 Equation of State

The linearized equation of state gives us a relationship between density, temperature, and salinity for water,

$$\rho = \rho_0[1 - \alpha(T - T_0) + \beta(S - S_0)],$$ (2.8)

where T is the temperature (in °C or K), S is the salinity (defined in the past as grams of salt per kilogram of sea water and recently by a practical salinity unit "psu", derived from measurements of conductivity and having no units). The constant ρ_0, T_0, and S_0 are the reference density, temperature, and salinity. α and β are the coefficient of thermal expansion (in 1/°C) and the coefficient of salinity expansion (in 1/psu). More details can be found in Gill (1982). Although we add one equation to the system, we also introduce two more variables T and S.

6

2.1.4 Salt Conservation

The evolution of salt in sea water is governed by

$$\frac{DS}{Dt} = \kappa_S \nabla^2 S, \tag{2.9}$$

where κ_S is the coefficient of salt diffusion (in m^2/s). It states that a seawater parcel conserves its salt content except for diffusion.

2.1.5 Energy Conversation

Until now, we have six equations along with seven unknowns, so we still need one more equation. The first law of thermodynamics states,

$$\frac{de}{dt} = Q - W, \tag{2.10}$$

where e is the internal energy, Q is the rate of heat gain, and W is the rate of work done by the pressure around the fluid. From Cushman-Roisin (1994), we have the energy equation as follow,

$$\rho C_\nu \frac{DT}{Dt} + p\nabla \cdot \mathbf{u} = k_T \nabla^2 T, \tag{2.11}$$

where C_ν is the heat capacity at constant volume (in J/(Kg·K)) and k_T is the thermal conductivity (in J/(s·m·K)).

Finally we have a closed system with seven equations (one continuity equation, three momentum equations, one equation of state, one salt equation, and one energy equation) and seven unknowns (u, v, w, ρ, p, T, and S).

2.1.6 Boussinesq Approximation

In many geophysical systems, the fluid density varies by a small amount about a mean value ρ_0,

$$\rho = \rho_0 + \rho'(x, y, z, t), \quad |\rho'| \ll \rho_0, \tag{2.12}$$

where ρ' is the density perturbation. Substituting ρ into the continuity equation (2.1) gives

$$\rho_0 \left(\frac{\partial u}{\partial x} + \frac{\partial v}{\partial y} + \frac{\partial w}{\partial z} \right) + \rho' \left(\frac{\partial u}{\partial x} + \frac{\partial v}{\partial y} + \frac{\partial w}{\partial z} \right)$$
$$+ \left(\frac{\partial \rho'}{\partial t} + u\frac{\partial \rho'}{\partial x} + v\frac{\partial \rho'}{\partial y} + w\frac{\partial \rho'}{\partial z} \right) = 0. \tag{2.13}$$

For geophysical flows the relative variations of density in time and space are usually much less than the relative variations of the velocity field. This implies

that the terms in the third group are typically much smaller than those in the second. However, terms in this second group are always much less than those in the first because $|\rho'| \ll \rho_0$. So the continuity equation is simplified to

$$\frac{\partial u}{\partial x} + \frac{\partial v}{\partial y} + \frac{\partial w}{\partial z} = 0. \tag{2.14}$$

Using a similar procedure, we approximate the density in the horizontal momentum equations with the mean value ρ_0. However, in the vertical momentum equation ρ appears not only on the left hand side where we can approximate ρ by ρ_0, but also on the right hand side of equation, in front of the gravitational acceleration g, which we cannot apply the Boussinesq approximation to. In hydrostatic balance, we know density ρ_0 and pressure $p_0(z)$ have the following relation,

$$\frac{dp_0(z)}{dz} = -\rho_0 g. \tag{2.15}$$

Expressing the pressure as a sum of a mean value and perturbation

$$p = p_0(z) + p'(x, y, z, t), \tag{2.16}$$

the vertical momentum equation becomes

$$\left(1 + \frac{\rho'}{\rho_0}\right)\frac{Dw}{Dt} = -\frac{1}{\rho_0}\frac{\partial p'}{\partial z} - \frac{\rho' g}{\rho_0} + \nu\nabla^2 w, \tag{2.17}$$

where $\nu = \mu/\rho_0$ is the kinematic viscosity (in m^2/s). Given $|\rho'| \ll \rho_0$, the ratio ρ'/ρ_0 can be neglected as in the horizontal momentum equations. However, the buoyancy term $\rho' g/\rho_0$ is very important and cannot be neglected. For example, it is these density variations that drive the convective motion when a layer of fluid is heated from below. Then the vertical momentum equation is simplified to

$$\frac{Dw}{Dt} = -\frac{1}{\rho_0}\frac{\partial p'}{\partial z} - \frac{\rho' g}{\rho_0} + \nu\nabla^2 w, \tag{2.18}$$

While given $\partial p_0(z)/\partial x = \partial p_0(z)/\partial y = 0$, we can exchange the pressure in the horizontal momentum equations to the pressure perturbation p', that is, the pair of p and ρ and the pair of p' and ρ' are interchangeable in the governing equations. In short density ρ can be approximated by its mean value ρ_0 except when ρ is in front of gravitational acceleration g. This method is called the Boussinesq approximation.

Next we simplify the energy equation (2.11). Using the simplified continuity equation (2.14), the energy equation becomes

$$\frac{DT}{Dt} = \kappa_T \nabla^2 T, \tag{2.19}$$

where $\kappa_T = k_T/\rho_0 C_\nu$ is the kinematic diffusivity (in m^2/s). If we assume S is a constant, then salinity equation drops out. Using this equation for temperature (2.19) and the equation of state (2.8), we obtain

$$\frac{D\rho}{Dt} = \kappa_T \nabla^2 \rho, \tag{2.20}$$

8

which is often called density equation.

In summary, under the Boussinesq approximation we finally have the governing equations of motions,

$$\frac{Du}{Dt} - fv = -\frac{1}{\rho_0}\frac{\partial p}{\partial x} + \nu\nabla^2 u, \tag{2.21}$$

$$\frac{Dv}{Dt} + fu = -\frac{1}{\rho_0}\frac{\partial p}{\partial y} + \nu\nabla^2 v, \tag{2.22}$$

$$\frac{Dw}{Dt} = -\frac{1}{\rho_0}\frac{\partial p}{\partial z} - \frac{\rho g}{\rho_0} + \nu\nabla^2 w, \tag{2.23}$$

$$\frac{\partial u}{\partial x} + \frac{\partial v}{\partial y} + \frac{\partial w}{\partial z} = 0, \tag{2.24}$$

$$\frac{D\rho}{Dt} = \kappa_T\nabla^2\rho, \tag{2.25}$$

where p and ρ can be either total pressure and density or perturbation of pressure and density.

2.1.7   Boundary Conditions

In order to solve the governing differential equations, we need initial conditions and boundary conditions. On the solid bottom of the domain, the velocity must be tangent to the land boundary, that is, the normal vector to the boundary surface is orthogonal to the velocity vector. If we define the bottom as $z - b(x, y) = 0$, the boundary condition at the bottom is obtained,

$$w = u\frac{\partial b}{\partial x} + v\frac{\partial b}{\partial y}, \tag{2.26}$$

which can be rewritten as

$$\frac{D(z - b)}{Dt} = 0, \text{ at } z = b. \tag{2.27}$$

At the free surface $z = \eta(x, y)$, we have a similar boundary condition,

$$\frac{D(z - \eta)}{Dt} = 0, \text{ at } z = \eta(x, y). \tag{2.28}$$

Both boundary conditions are called kinematic boundary conditions.

In addition to the kinematic boundary condition at the surface, there is a dynamic boundary condition. We ignore surface tension because the scales of interest are far too large for surface tension to be important. Then the pressure just below the free surface is always equal to the ambient pressure.

9

If the viscosity is non-zero, another boundary condition must be imposed, too. At a solid boundary if the fluids have zero velocity relative to the boundary, that is, $\mathbf{u} \times \hat{n} = \mathbf{U} \times \hat{n}$, where $\mathbf{u}$ is the fluid velocity, $\mathbf{U}$ is the boundary velocity, and $\hat{n}$ is the unit vector normal to the boundary, we have the no-slip boundary condition. On the other hand, the free-slip condition has the form $\partial u / \partial y = \partial w / \partial y = 0$ for boundaries $y = $ constant, for instance.

2.2 Gravity Waves

One common wave motion that appears in everyday life is gravity waves. When waves occur at the surface of a liquid, with gravity providing the restoring force, they are called surface gravity waves. On the other hand, waves can also be generated in fluids with variable density and these are called internal gravity waves. In this section, we briefly derive the governing equations for the surface gravity waves and internal gravity waves. Two special waves, namely Poincaré waves and Kelvin waves, are introduced thereafter.

2.2.1 Surface Gravity Waves

In this section, we consider surface gravity waves in a constant density, inviscid fluid with a flat bottom having the following properties. The waves move slowly enough so that f is not negligible. The fluid is shallow, that is, the wavelength λ is much greater than the depth of the fluid H, so the vertical velocity w is much smaller than the horizontal velocities u and v. Then the acceleration Dw/Dt is negligible in the vertical momentum equation, and to a first approximation that the pressure distribution is hydrostatic. Ignoring the viscous terms, we have the following governing equations for a constant density fluid,

$$\frac{Du}{Dt} - fv = -\frac{1}{\rho_0}\frac{\partial p}{\partial x}, \tag{2.29}$$

$$\frac{Dv}{Dt} + fu = -\frac{1}{\rho_0}\frac{\partial p}{\partial y}, \tag{2.30}$$

$$0 = -\frac{1}{\rho_0}\frac{\partial p}{\partial z} - g, \tag{2.31}$$

$$\frac{\partial u}{\partial x} + \frac{\partial v}{\partial y} + \frac{\partial w}{\partial z} = 0. \tag{2.32}$$

Let z be measured upward from the bottom (Fig. 2.1), and η be the displacement of the free surface. Then the pressure at height z is given by

$$p = \rho_0 g(H + \eta - z) + P_0, \tag{2.33}$$

because it is hydrostatic, where the constant P_0 is the atmospheric pressure. The horizontal pressure gradients become

$$\frac{\partial p}{\partial x} = \rho_0 g \frac{\partial \eta}{\partial x}, \quad \frac{\partial p}{\partial y} = \rho_0 g \frac{\partial \eta}{\partial y}, \tag{2.34}$$

which are independent of z. Therefore, from the horizontal momentum equations, the horizontal velocities u and v are independent of z if they initially are.
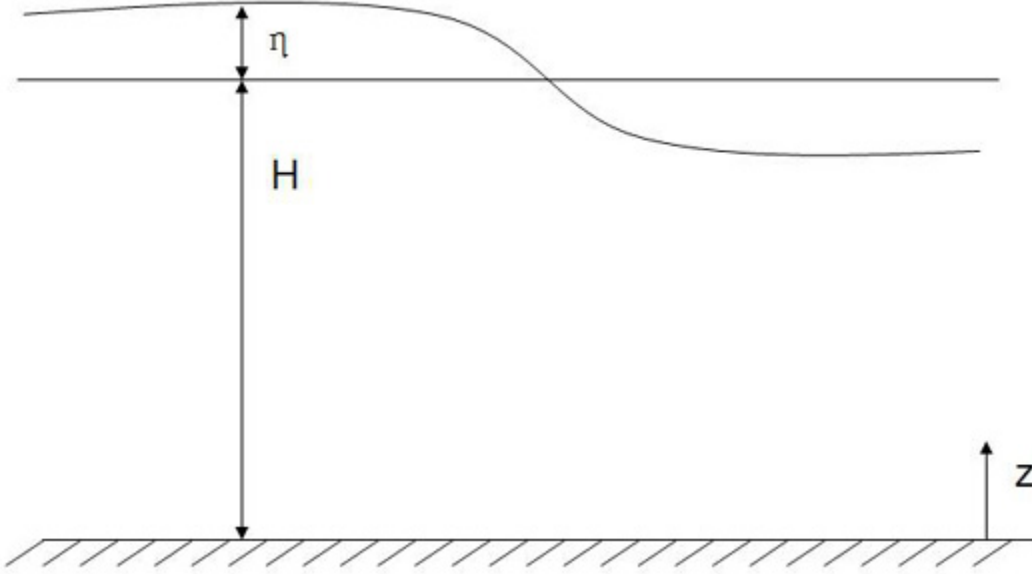
Figure 2.1: Shallow water over flat bottom

Next we consider the continuity equation (2.32). Since u and v are independent of z, w must linearly depend on z. Integrating vertically from $z = 0$ to $z = H + \eta$ gives,

$$(H + \eta)\frac{\partial u}{\partial x} + (H + \eta)\frac{\partial v}{\partial y} + w(\eta) - w(0) = 0, \tag{2.35}$$

where $w(\eta)$ is the vertical velocity at the free surface and $w(0) = 0$ is the vertical velocity at the flat bottom. From the kinematic boundary conditions we stated in the previous section, $w(\eta)$ is given by

$$w(\eta) = \frac{D\eta}{Dt} = \frac{\partial \eta}{\partial t} + u\frac{\partial \eta}{\partial x} + v\frac{\partial \eta}{\partial y}. \tag{2.36}$$

The governing equations then become,

$$\frac{\partial \eta}{\partial t} + \frac{\partial}{\partial x}[u(H + \eta)] + \frac{\partial}{\partial y}[v(H + \eta)] = 0, \tag{2.37}$$

$$\frac{Du}{Dt} - fv = -g\frac{\partial \eta}{\partial x}, \tag{2.38}$$

$$\frac{Dv}{Dt} + fu = -g\frac{\partial \eta}{\partial y}, \tag{2.39}$$

and this set of equations is often called shallow water equation.

11

2.2.2 Linear Internal Gravity Waves

Waves exist not only at the free surface, but also on the interface between two fluids of different densities. (The surface gravity waves are an extreme example of internal waves since they appear on the interface of air and liquid. As the density or movement of air is ignored this makes them somewhat different from internal waves in which density or movement of the upper layer is taken into account.) There is a well-known "dead water" phenomenon in which the ships experience unusually high drag. It was a mystery until Bjerknes, a Norwegian oceanographer, explained it as due to the internal waves generated at the interface between the lighter fresh layer and heavier salty layer by the motion of the ship (Fig. 2.2). The two-layer model is studied thoroughly in many fluid mechanics textbooks ,e.g., Kundu and Cohen (2004, Chpater 7), so we will not explain it here.
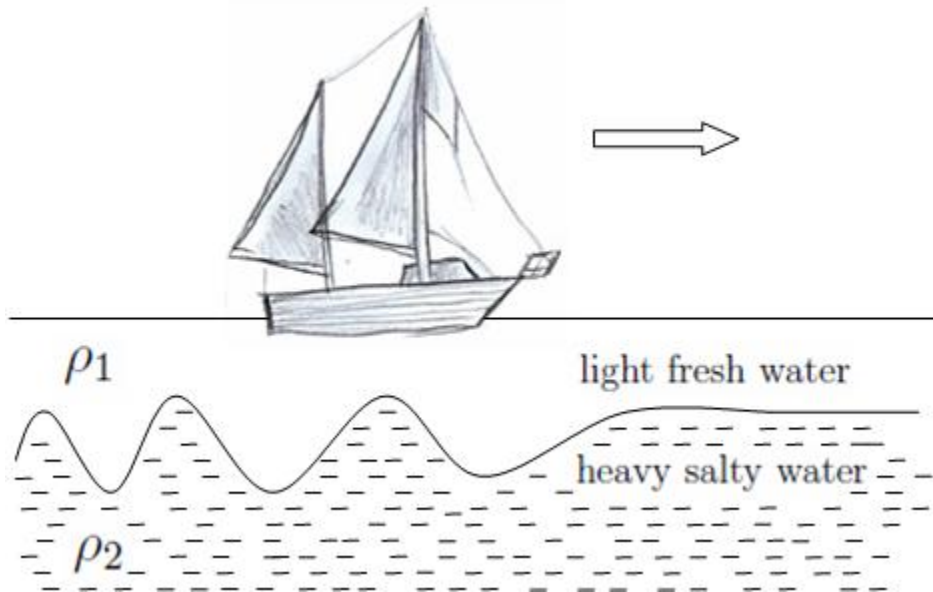
Figure 2.2: "Dead water" phenomenon

Internal waves also occur in continuously stratified fluids, in which the vertical density profile in a state of rest is a continuous function $\bar{\rho}(z)$. Recall the governing

equations if we assume the diffusivity $\kappa_T = 0$ and the viscosity $\nu = 0$,

$$\frac{Du}{Dt} - fv = -\frac{1}{\rho_0}\frac{\partial p}{\partial x}, \tag{2.40}$$

$$\frac{Dv}{Dt} + fu = -\frac{1}{\rho_0}\frac{\partial p}{\partial y}, \tag{2.41}$$

$$\frac{Dw}{Dt} = -\frac{1}{\rho_0}\frac{\partial p}{\partial z} - \frac{\rho g}{\rho_0}, \tag{2.42}$$

$$\frac{\partial u}{\partial x} + \frac{\partial v}{\partial y} + \frac{\partial w}{\partial z} = 0, \tag{2.43}$$

$$\frac{D\rho}{Dt} = 0. \tag{2.44}$$

We first express the equations in terms of perturbations from a state of rest.

$$p = \bar{p}(z) + p', \tag{2.45}$$

$$\rho = \bar{\rho}(z) + \rho', \tag{2.46}$$

where $\bar{p}(z)$ and $\bar{\rho}(z)$ are background pressure and density, and p' and ρ' are perturbations. $\bar{\rho}(z)$ and pressure $\bar{p}(z)$ are in hydrostatic balance,

$$\frac{d\bar{p}(z)}{dz} = -\bar{\rho}(z)g. \tag{2.47}$$

The density equation (2.44) then becomes

$$\frac{\partial}{\partial t}(\bar{\rho} + \rho') + u\frac{\partial}{\partial x}(\bar{\rho} + \rho') + v\frac{\partial}{\partial y}(\bar{\rho} + \rho') + w\frac{\partial}{\partial z}(\bar{\rho} + \rho') = 0. \tag{2.48}$$

Here $\partial\bar{\rho}/\partial t = \partial\bar{\rho}/\partial x = \partial\bar{\rho}/\partial y = 0$, and the nonlinear terms $u\partial\rho'/\partial x$, $v\partial\rho'/\partial y$, and $w\partial\rho'/\partial z$ are negligible in small amplitude motions. Then the density equation reduces to

$$\frac{\partial\rho'}{\partial t} + w\frac{d\bar{\rho}}{dz} = 0, \tag{2.49}$$

which states that the density perturbation is generated only by the vertical advection of the background density. Next we define

$$N^2 \equiv -\frac{g}{\rho_0}\frac{d\bar{\rho}}{dz}, \tag{2.50}$$

where $N(z)$ is called the buoyancy frequency and it has units of rad/s.

In summary, the governing equations for linear internal gravity waves are,

$$\frac{Du}{Dt} - fv = -\frac{1}{\rho_0}\frac{\partial p}{\partial x}, \tag{2.51}$$

$$\frac{Dv}{Dt} + fu = -\frac{1}{\rho_0}\frac{\partial p}{\partial y}, \tag{2.52}$$

$$\frac{Dw}{Dt} = -\frac{1}{\rho_0}\frac{\partial p}{\partial z} - \frac{\rho g}{\rho_0}, \tag{2.53}$$

$$\frac{\partial u}{\partial x} + \frac{\partial v}{\partial y} + \frac{\partial w}{\partial z} = 0, \tag{2.54}$$

$$\frac{\partial \rho}{\partial t} - \frac{N^2(z)\rho_0}{g}w = 0. \tag{2.55}$$

Note that p and ρ are pressure perturbation and density perturbation respectively. We will analyze this set of equations in detail in Chapter 3.

2.2.3   Poincaré Waves

Given the shallow water equation,

$$\frac{\partial \eta}{\partial t} + \frac{\partial}{\partial x}[u(H+\eta)] + \frac{\partial}{\partial y}[v(H+\eta)] = 0, \tag{2.56}$$

$$\frac{\partial u}{\partial t} - fv = -g\frac{\partial \eta}{\partial x}, \tag{2.57}$$

$$\frac{\partial v}{\partial t} + fu = -g\frac{\partial \eta}{\partial y}, \tag{2.58}$$

we now look for progressive waves of the form

$$(u, v, \eta) = (\hat{u}, \hat{v}, \hat{\eta})e^{i(kx+ly-\omega t)}, \tag{2.59}$$

where k and l are the wavenumber in x and y direction. After substituting and solving, we obtain the dispersion relation,

$$\omega^2 = f^2 + gHK^2, \tag{2.60}$$

where $K = \sqrt{k^2 + l^2}$ is the magnitude of the horizontal wavenumber. Waves affected by Coriolis forces are called Poincaré Waves. The quantity $\sqrt{gH}/f$ is called Rossby radius of deformation or simply radius of deformation. It is the length scale at which rotational effects become as important as buoyancy effects.

When there is no rotation $f = 0$, the frequency is $\omega = K\sqrt{gH}$, and the phase speed is $c = \sqrt{gH}$. The waves become classic shallow water surface gravity waves without the effect of rotation. In the limit of large wavenumber $K^2 \gg f^2/gH$, i.e., wavelengths are much shorter than the radius of deformation, we also obtain the wave frequency $\omega = K\sqrt{gH} \gg f$. Then the wave speed $c \approx \sqrt{gH}$ and the waves become classical gravity waves, too. It is not surprising since the wave is too short and fast to feel the rotation of Earth.

2.2.4 Kelvin Waves

The Kelvin wave is a traveling wave that requires the support of a lateral boundary, which we can see along the coastlines (Fig. 2.3). Consider a semi-infinite layer of
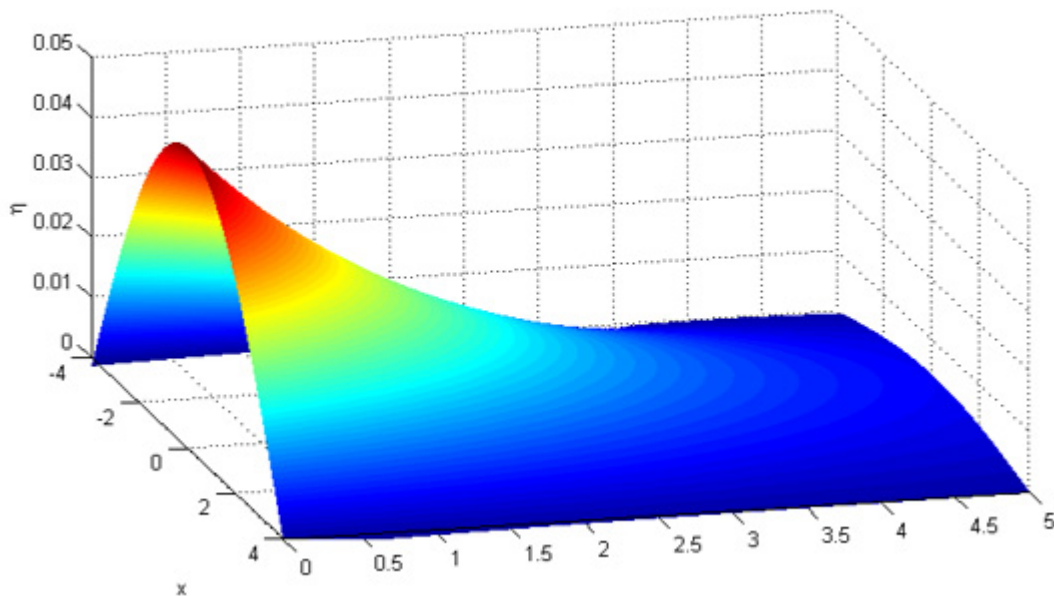
Figure 2.3: Kelvin waves propagating in x direction

fluid bounded below by a horizontal bottom, above by a free surface, and on one side by a vertical wall, say $y = 0$ plane, with waves propagating in x direction. Using the boundary condition we presented before, v needs to be zero at the side wall. Lord Kelvin thought that the vanishing of v at the side wall suggested the possibility of v being zero everywhere. Let us assume $v \equiv 0$, then the shallow water equations give the governing equations,

$$\frac{\partial \eta}{\partial t} + H\frac{\partial u}{\partial x} = 0, \tag{2.61}$$

$$\frac{\partial u}{\partial t} = -g\frac{\partial \eta}{\partial x}, \tag{2.62}$$

$$fu = -g\frac{\partial \eta}{\partial y}, \tag{2.63}$$

where H is the depth of the fluid. Assuming a solution is in the form of

$$[u, \eta] = [\hat{u}(y), \hat{\eta}(y)]e^{i(kx-\omega t)}, \tag{2.64}$$

where k is the wavenumber (in 1/m) and ω (in 1/s) is the wave frequency. Substituting them into the governing equations and solving the system gives

$$\eta = \eta_0 e^{-fy/c} \cos k(x - ct), \tag{2.65}$$

$$u = \eta_0 \sqrt{\frac{g}{H}} e^{-fy/c} \cos k(x - ct), \tag{2.66}$$

$$v = 0, \tag{2.67}$$

where $c = \sqrt{gH}$ is the propagation speed of the Kelvin wave, η_0 is the amplitude at the coast, which is defined by maximum displacement by which the wave is going above or below its resting position. In the Northern Hemisphere ($f > 0$), the wave travels with the coast on its right, while in the Southern Hemisphere, with the coast on its left. We can see Kelvin waves in the English Channel (Fig. 2.4). The North Atlantic tide enters the Channel from the west to the east. With the effect of rotation and coast boundary, we expect the Kelvin waves appear and travel against the coast on its right, namely, France. This explains why tides are higher along the French coast than along the British coast.

Analogous to the surface Kelvin waves, we also have the internal Kelvin waves at the interface between two fluids of different densities. If the lower layer is very deep, then the speed of propagation is

$$c_i = \sqrt{g'h_1}, \tag{2.68}$$

where h_1 is the thickness of the upper layer and $g' = g(\rho_2 - \rho_1)/\rho_2$ is the reduced gravity acceleration, and ρ_1 and ρ_2 are the density of upper and lower layer respectively. the quantity c_i/f is called internal radius of deformation. It is the length scale at which rotational effects become important in internal waves.
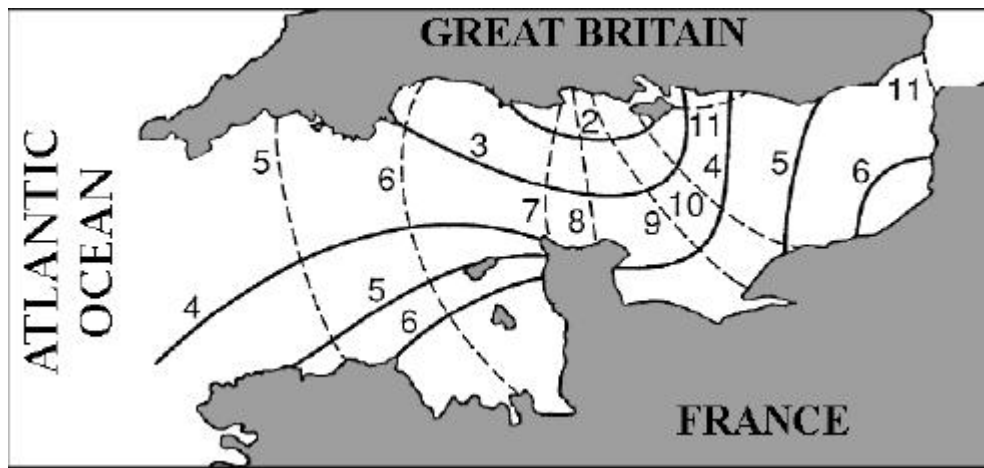
Figure 2.4: Cotidal lines (dashed) with time in lunar hours for the tide in the English channel showing the eastward progression of the tide from the North Atlantic Ocean. Lines of equal tidal range (solid, with values in meters) reveal larger amplitudes along the French coast, namely to the right of the wave progression in accordance with Kelvin waves. (From Cushman-Roisin 1994)

Chapter 3

Analytical Solutions: Linear Theory

3.1 Problem Introduction

When wind blows over a stratified lake, an interface tilt is usually generated, causing the thermocline to rise upwind and fall downwind (Monismith 1986). When the wind stops blowing, the thermocline is released and adjusts through the generation of internal basin-scale waves which may then steepen nonlinearly and transfer energy to waves of higher frequencies and shorter wavelengths. The solution for a uniform, constant wind imposed suddenly over a circular homogeneous rotating lake with a flat bottom was studied by Csanady (1968). When the Earth's rotation is considered, Beletsky et al. (1997) studied the problem of internal Kelvin waves and coastal upwelling both in a flat bottom and a parabolic bottom basin using POM and DIECAST. Stocker and Imberger (2003) investigated the response of a stratified rotating lake to the release of a linearly tilted interface. Energy partitioning was studied as a function of the Burger number S. de la Fuente et al. (2008) discussed the evolution of internal waves in a two-layer, rotating, circular lake under nonlinear and weak non-hydrostatic effects. They showed that Poincaré waves steepen and generate solitary-like waves with shorter wavelengths, but most of the energy contained in these waves is transferred back and forth between the parent wave and the solitary-like waves. Kelvin waves, on the other hand, steepen and lose their energy to solitary-like waves. In this thesis, we discuss internal waves in a rotating, continuously stratified, flat-bottom, circular lake with fully nonlinear and non-hydrostatic effects, which is different than most previous studies in the literature where hydrostatic balance is assumed. In this chapter, an analytical solution for the linearized governing equations is derived.

3.2 Governing Equations

In section 2.2.2, the governing equations for internal gravity waves are presented. If we assume the fluid is inviscid, i.e. the viscosity $\nu = 0$, and neglect the nonlinear advection term $\mathbf{u} \cdot \nabla \mathbf{u}$ when the wave amplitude is small, we obtain the linearized governing equations which can be solved analytically,

$$u_t - fv = -p_x, \tag{3.1}$$

$$v_t + fu = -p_y, \tag{3.2}$$

$$w_t = -p_z - \rho g, \tag{3.3}$$

$$\rho_t = \frac{N^2(z)}{g} w, \tag{3.4}$$

$$u_x + v_y + w_z = 0, \tag{3.5}$$

where p and ρ are the pressure perturbation and density perturbation, and both have been scaled by the reference density ρ_0. Since we are studying waves in a circular lake, we will use polar coordinates. The governing equations then become,

$$\frac{\partial u_r}{\partial t} - fu_\theta = -\frac{\partial p}{\partial r}, \tag{3.6}$$

$$\frac{\partial u_\theta}{\partial t} + fu_r = -\frac{1}{r}\frac{\partial p}{\partial \theta}, \tag{3.7}$$

$$w_t = -p_z - \rho g, \tag{3.8}$$

$$\rho_t = \frac{N^2(z)}{g} w, \tag{3.9}$$

$$\frac{1}{r}\frac{\partial}{\partial r}(r u_r) + \frac{1}{r}\frac{\partial u_\theta}{\partial \theta} + \frac{\partial w}{\partial z} = 0. \tag{3.10}$$

If we assume a rigid lid instead of the free surface, then the boundary conditions on the surface and bottom are $w = 0$ at $z = 0$ and $z = -H$, where z is measured upward from the surface and H is the depth of the lake. At the side wall $r = r_0$, where r_0 is the radius, no fluid through the wall. The side boundary condition then is $u_r = 0$ at $r = r_0$.

3.3 Analytical Solutions in Linear Theory

Taking the divergence of the horizontal momentum equations (3.6) and (3.7), and using the continuity equation (3.10) gives

$$\frac{1}{r}\frac{\partial u_r}{\partial \theta} - \frac{1}{r}\frac{\partial}{\partial r}(r u_\theta) = \frac{1}{f}(w_{zt} - \nabla_h^2 p), \tag{3.11}$$

where

$$\nabla_h^2 = \frac{1}{r}\frac{\partial}{\partial r}\left(r\frac{\partial}{\partial r}\right) + \frac{1}{r^2}\frac{\partial^2}{\partial \theta^2}, \tag{3.12}$$

19

is the horizontal Laplacian. Next taking the curl of (3.6) and (3.7), and using (3.10) leads to

$$\frac{\partial}{\partial t}\left(\frac{1}{r}\frac{\partial u_r}{\partial \theta} - \frac{1}{r}\frac{\partial}{\partial r}(ru_\theta)\right) + fw_z = 0. \tag{3.13}$$

Substituting (3.11) into (3.13) yields

$$w_{ztt} + f^2 w_z = \nabla_h^2 p_t. \tag{3.14}$$

Taking the partial derivative of (3.8) with respect to t and using (3.9) results in a single equation for w,

$$w_{tt} + N^2(z)w = -p_{zt}. \tag{3.15}$$

Eliminating p from (3.14) and (3.15) gives

$$\frac{\partial^2}{\partial t^2}\nabla^2 w + N^2(z)\nabla_h^2 w + f^2 w_{zz} = 0. \tag{3.16}$$

We now look for waves propagating around the lake in the θ direction of the form

$$w(r,\theta,z,t) = \hat{w}(r)\sin(n\theta - \omega t)\phi(z), \tag{3.17}$$

for $0 \leq r \leq r_0$ and $-H \leq z \leq 0$. Substituting the proposed solution (3.17) into (3.16) gives

$$\phi(z)\big(N^2(z) - \omega^2\big)\left[\hat{w}''(r) + \frac{\hat{w}'(r)}{r} - \frac{n^2}{r^2}\hat{w}(r)\right] + \phi''(z)(f^2 - \omega^2)\hat{w}(r) = 0, \tag{3.18}$$

which can be rewritten as

$$\frac{\hat{w}''(r) + \frac{1}{r}\hat{w}'(r) - \frac{n^2}{r^2}\hat{w}(r)}{\hat{w}(r)} = \frac{\phi''(z)(\omega^2 - f^2)}{\phi(z)\big(N^2(z) - \omega^2\big)} = C, \tag{3.19}$$

where C is a constant, with boundary conditions

$$\phi(0) = \phi(-H) = 0, \tag{3.20}$$
$$u_r = 0 \quad \text{at } r = r_0. \tag{3.21}$$

To get the side boundary condition in terms of w, eliminating u_θ from (3.6) and (3.7) gives,

$$\left(\frac{\partial^2}{\partial t^2} + f^2\right)u_r = -\frac{f}{r}\frac{\partial p}{\partial \theta} - \frac{\partial}{\partial t}\left(\frac{\partial p}{\partial r}\right). \tag{3.22}$$

From equation (3.8) and (3.9) we have

$$w_{tt} + N^2(z)w = -p_{zt}. \tag{3.23}$$

Eliminating p from (3.22) and (3.23) yields

$$\left(\frac{f}{r}\frac{\partial}{\partial \theta} + \frac{\partial^2}{\partial t\partial r}\right)\big(w_{tt} + N^2(z)w\big) = \left(\frac{\partial^2}{\partial t\partial z}\right)\left(\frac{\partial^2}{\partial t^2} + f^2\right)u_r. \tag{3.24}$$

20

Then at the boundary $r = r_0$, applying the boundary condition $u_r = 0$ results in

$$\left(\frac{f}{r}\frac{\partial}{\partial\theta} + \frac{\partial^2}{\partial t\partial r}\right)\left(w_{tt} + N^2(z)w\right) = \left(N^2(z) - \omega^2\right)\left(\frac{f}{r}\frac{\partial}{\partial\theta} + \frac{\partial^2}{\partial t\partial r}\right)w = 0, \quad (3.25)$$

after substituting w from (3.17). The boundary condition is then simplified to

$$\left(\frac{f}{r}\frac{\partial}{\partial\theta} + \frac{\partial^2}{\partial t\partial r}\right)w = 0, \quad r = r_0. \quad (3.26)$$

Three cases will be considered in turn, $C < 0$, $C > 0$, and $C = 0$.

3.3.1 Case I: $C = -\alpha^2 < 0$

From (3.19) we obtain equations for w and ϕ

$$\hat{w}''(r) + \frac{\hat{w}'(r)}{r} - \frac{n^2}{r^2}\hat{w}(r) + \alpha^2\hat{w}(r) = 0, \quad (3.27)$$

$$\phi''(z) + \alpha^2\frac{N^2(z) - \omega^2}{\omega^2 - f^2}\phi(z) = 0, \quad (3.28)$$

with boundary conditions

$$\left(\frac{f}{r}\frac{\partial}{\partial\theta} + \frac{\partial^2}{\partial t\partial r}\right)w = 0, \quad \text{at } r = r_0, \quad (3.29)$$

$$\phi(0) = \phi(-H) = 0. \quad (3.30)$$

Equation (3.28) with boundary condition (3.30) gives an eigenvalue problem for ϕ and ω if α is given.

Defining $r = x/\alpha$ and $\tilde{w}(x) = \hat{w}(r)$, (3.27) leads to

$$x^2\tilde{w}''(x) + x\tilde{w}'(x) + (x^2 - n^2)\tilde{w}(x) = 0, \quad (3.31)$$

which is Bessel's Equation of order n. The general solution is

$$\tilde{w}(x) = AJ_n(x) + BY_n(x), \quad (3.32)$$

where A and B are arbitrary constants. $J_n(x)$ is the Bessel function of the first kind, which has the Taylor Series expansion,

$$J_n(x) = \sum_{j=0}^{\infty}\frac{(-1)^j}{j!\Gamma(j + n + 1)}\left(\frac{x}{2}\right)^{2j+n}, \quad (3.33)$$

where Γ is the Gamma function, defined by

$$\Gamma(x) = \int_0^{\infty} t^{x-1}e^{-t}dt. \quad (3.34)$$

If x is an positive integer, the Gamma function is reduced to

$$\Gamma(x) = (x-1)!. \tag{3.35}$$

$Y_n(x)$ is the Bessel function of the second kind, defined by

$$Y_n(x) = \frac{J_n(x)\cos(n\pi) - J_{-n}(x)}{\sin(n\pi)}. \tag{3.36}$$

At the origin $x = 0$, we need $\tilde{w}(x)$ to be finite. Since $Y_n(x) \to \infty$ as $x \to 0$, we must have $B = 0$, which gives

$$w(r, \theta, z, t) = AJ_n(\alpha r)\sin(n\theta - \omega t)\phi(z). \tag{3.37}$$

Substituting w into boundary condition (3.29) gives the following problem,

$$\frac{fn}{r_0}J_n(\alpha r_0) - \omega\alpha J_n'(\alpha r_0) = 0. \tag{3.38}$$

In summary, we obtain the following eigenvalue problem for α and ω,

$$\frac{fn}{r_0}J_n(\alpha r_0) - \omega\alpha J_n'(\alpha r_0) = 0,$$
$$\phi''(z) + \alpha^2 \frac{N^2(z) - \omega^2}{\omega^2 - f^2}\phi(z) = 0, \tag{3.39}$$

with $\phi(0) = \phi(-H) = 0$.

Given the eigenvalues α and ω, and the expression for w we can proceed to find the density, pressure and horizontal velocities. Equation (3.9) immediately gives ρ,

$$\rho = \hat{\rho}(r)\cos(n\theta - \omega t)N^2(z)\phi(z), \tag{3.40}$$

where

$$\hat{\rho}(r) = \frac{1}{\omega g}\hat{w}(r). \tag{3.41}$$

The continuity equation (3.10) implies that the z component of u_r and u_θ are $\phi'(z)$. Equation (3.6) and (3.7) tells that p, u_r, and u_θ have the same z component, which is $\phi'(z)$. From (3.8) we solve for p,

$$p = \hat{p}(r)\cos(n\theta - \omega t)\phi'(z). \tag{3.42}$$

Substituting p into (3.8) yields

$$\hat{p}(r)\phi''(z) = \omega\hat{w}(r)\phi(z) - \hat{\rho}(r)N^2(z)\phi(z). \tag{3.43}$$

Recalling equation (3.19)

$$\frac{\phi''(z)(\omega^2 - f^2)}{\phi(z)\big(N^2(z) - \omega^2\big)} = -\alpha^2, \tag{3.44}$$

22

and combining (3.43) and (3.44), we obtain

$$\hat{p}(r) = \frac{\omega^2 - f^2}{\omega \alpha^2} \hat{w}(r). \tag{3.45}$$

From (3.6) and (3.7), we can easily solve for u_r and u_θ.

In summary, we have the following solution of the linearized system,

$$w = \hat{w}(r) \sin(n\theta - \omega t)\phi(z), \tag{3.46}$$
$$\rho = \hat{\rho}(r) \cos(n\theta - \omega t)N^2(z)\phi(z), \tag{3.47}$$
$$p = \hat{p}(r) \cos(n\theta - \omega t)\phi'(z), \tag{3.48}$$
$$u_r = \hat{u}_r(r) \sin(n\theta - \omega t)\phi'(z), \tag{3.49}$$
$$u_\theta = \hat{u}_\theta(r) \cos(n\theta - \omega t)\phi'(z), \tag{3.50}$$

where

$$\hat{w}(r) = AJ_n(\alpha r), \tag{3.51}$$

$$\hat{\rho}(r) = \frac{1}{\omega g}\hat{w}(r), \tag{3.52}$$

$$\hat{p}(r) = \frac{\omega^2 - f^2}{\omega \alpha^2}\hat{w}(r), \tag{3.53}$$

$$\hat{u}_r(r) = \frac{\frac{nf}{r}\hat{p}(r) - \omega\hat{p}'(r)}{f^2 - \omega^2}, \tag{3.54}$$

$$\hat{u}_\theta(r) = \frac{-\frac{n\omega}{r}\hat{p}(r) + f\hat{p}'(r)}{f^2 - \omega^2}. \tag{3.55}$$

We also need to solve the following eigenvalue problem for ω and α,

$$\frac{fn}{r_0}J_n(\alpha r_0) - \omega\alpha J_n'(\alpha r_0) = 0, \tag{3.56}$$

$$\phi''(z) + \alpha^2 \frac{N^2(z) - \omega^2}{\omega^2 - f^2}\phi(z) = 0, \tag{3.57}$$

with boundary conditions $\phi(0) = \phi(-H) = 0$.

In the MITgcm model, the temperature is used instead of the density, so we need to find an expression for the temperature. The linear equation of state is

$$\rho_{\text{total}} = \rho_0[1 - \alpha_T(T - T_0) + \beta_S(S - S_0)]. \tag{3.58}$$

Since we are interested in lakes, the salinity is constant S_0. Then the equation of state becomes

$$\rho_{\text{total}} = \rho_0\left(1 - \alpha_T(T - T_0)\right). \tag{3.59}$$

Next we express the temperature T as the sum of background temperature $\bar{T}(z)$ and a perturbation T_p,

$$T = \bar{T}(z) + T_p. \tag{3.60}$$

23

We assume the undisturbed temperature has a tanh distribution,

$$\bar{T}(z) = T_b + \left(\frac{T_s - T_b}{2}\right)\left[1 + \tanh\left(\frac{z - z_0}{d}\right)\right], \tag{3.61}$$

where T_s is the surface temperature, T_b is the bottom temperature, z_0 is the rest position of the thermocline, and d is the thickness of the thermocline. From this we obtain

$$N^2(z) = g\alpha_T \frac{d\bar{T}(z)}{dz} = g\alpha_T \frac{T_s - T_b}{2d}\text{sech}^2\left(\frac{z - z_0}{d}\right). \tag{3.62}$$

Fig. 3.1 shows typical distributions of $\bar{T}(z)$ and $N(z)$. From the linear equation of state, we obtain T_p

$$T_p = -\frac{\rho_{\text{total}} - \rho_0}{\rho_0}\frac{1}{\alpha_T} = -\frac{\rho}{\alpha_T}. \tag{3.63}$$

Note that $\rho = (\rho_{\text{total}} - \rho_0)/\rho_0$ is the density perturbation scaled by ρ_0.
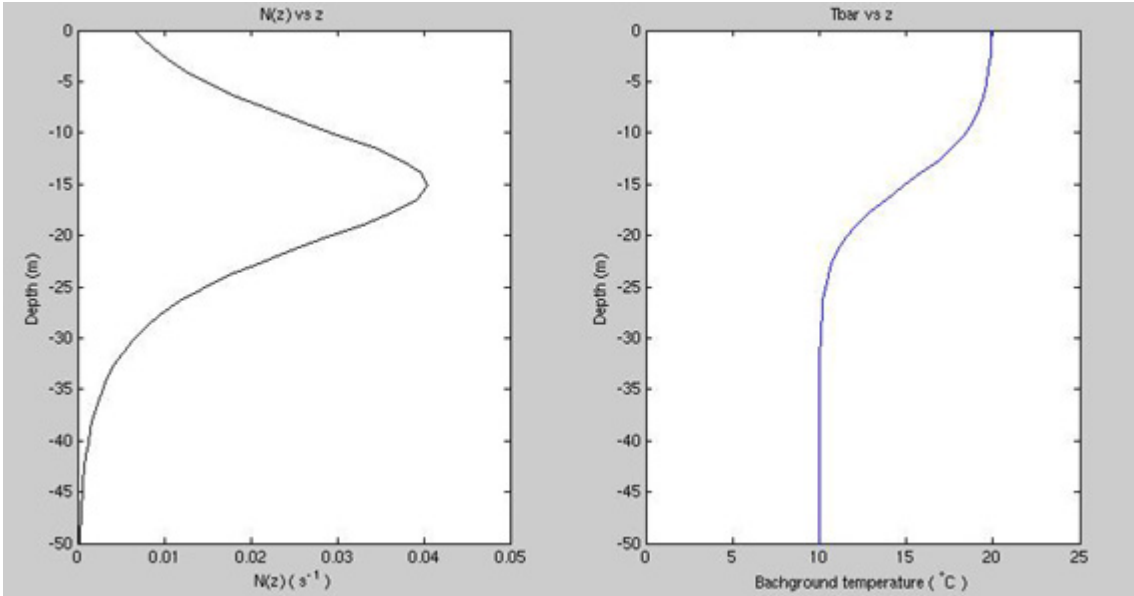
Figure 3.1: Typical distributions of $\bar{T}(z)$ and $N(z)$

3.3.2   Case II: $C = \beta^2 > 0$

Case II can be obtained from case I by allowing α to be imaginary. In the analysis of previous subsection, if $\alpha^2 > 0$ we get case I, and if $\alpha^2 < 0$ we get case II with $\alpha = i\beta$ where β is real. Using the property $J_n(ix) = i^n I_n(x)$, we will have the eigenvalue problem for case II,

$$\frac{fn}{r_0}I_n(\beta r_0) - \omega\beta I_n'(\beta r_0) = 0, \tag{3.64}$$

$$\phi''(z) - \beta^2 \frac{N^2(z) - \omega^2}{\omega^2 - f^2}\phi(z) = 0, \tag{3.65}$$

with boundary conditions $\phi(0) = \phi(-H) = 0$. Here $I_n(x)$ is the modified Bessel function of the first kind, defined by

$$I_n(x) = i^{-n} J_n(ix). \tag{3.66}$$

The solution for case II now has the form

$$w = \hat{w}(r) \sin(n\theta - \omega t)\phi(z), \tag{3.67}$$
$$p = \hat{p}(r) \cos(n\theta - \omega t)\phi'(z), \tag{3.68}$$
$$u_r = \hat{u}_r(r) \sin(n\theta - \omega t)\phi'(z), \tag{3.69}$$
$$u_\theta = \hat{u}_\theta(r) \cos(n\theta - \omega t)\phi'(z), \tag{3.70}$$
$$\rho = \hat{\rho}(r) \cos(n\theta - \omega t)N^2(z)\phi(z), \tag{3.71}$$
$$T = \bar{T}(z) + T_p, \tag{3.72}$$
$$T_p = -\frac{\rho}{\alpha_T}, \tag{3.73}$$
$$\tag{3.74}$$

where

$$\hat{w}(r) = BI_n(\beta r), \tag{3.75}$$

$$\hat{p}(r) = -\frac{\omega^2 - f^2}{\omega\beta^2}\hat{w}(r), \tag{3.76}$$

$$\hat{u}_r(r) = \frac{\frac{nf}{r}\hat{p}(r) - \omega\hat{p}'(r)}{f^2 - \omega^2}, \tag{3.77}$$

$$\hat{u}_\theta(r) = \frac{-\frac{n\omega}{r}\hat{p}(r) + f\hat{p}'(r)}{f^2 - \omega^2}, \tag{3.78}$$

$$\hat{\rho}(r) = \frac{1}{\omega g}\hat{w}(r). \tag{3.79}$$

3.3.3 Case III: $C = 0$

Again from (3.19) we get two equations for w and ϕ,

$$\hat{w}''(r) + \frac{\hat{w}'(r)}{r} - \frac{n^2}{r^2}\hat{w}(r) = 0, \tag{3.80}$$
$$(\omega^2 - f^2)\phi''(z) = 0, \tag{3.81}$$

with $\phi(0) = \phi(-H) = 0$. If $\phi''(z) = 0$, the boundary conditions gives $\phi(z) \equiv 0$. Well we are not interested in the trivial solution, hence $\phi''(0) \neq 0$, which gives $\omega^2 = f^2$, and as a result $\phi(z)$ can take any form as long as it satisfies the boundary conditions. Equation (3.80) is an Euler type ODE, and the solution is

$$\hat{w}(r) = Er^n + Fr^{-n}, \tag{3.82}$$

where E and F are constants. We need $\hat{w}(0)$ to be finite, so $F = 0$.

Recall the relation between w and u_r in (3.24),

$$\left(\frac{f}{r}\frac{\partial}{\partial\theta} + \frac{\partial^2}{\partial t \partial r}\right)\left(w_{tt} + N^2(z)w\right) = \left(\frac{\partial^2}{\partial t \partial z}\right)\left(\frac{\partial^2}{\partial t^2} + f^2\right)u_r. \tag{3.83}$$

Then the right hand side of (3.83) is zero knowing $\omega^2 = f^2$ and we have

$$\left(\frac{f}{r}\frac{\partial}{\partial\theta} + \frac{\partial^2}{\partial t \partial r}\right)\left(w_{tt} + N^2(z)w\right) = 0. \tag{3.84}$$

Substituting w from (3.82) gives

$$\frac{fn}{r}r^n - \omega n r^{n-1} = 0, \tag{3.85}$$

therefore $\omega = f$. Following the same procedure we used early, we cannot find analytical solutions as similar as the ones in case I and II due to the uncertainty of $\phi(z)$. In our thesis, we will not analyze more about case III, and instead we focus on the first two cases more.

3.4 Eigenvalue Problem

3.4.1 Case I: $C = -\alpha^2 < 0$

Recall that the eigenvalue problem for case I is

$$\frac{fn}{r_0}J_n(\alpha r_0) - \omega\alpha J_n'(\alpha r_0) = 0, \tag{3.86}$$

$$\phi''(z) + \alpha^2 \frac{N^2(z) - \omega^2}{\omega^2 - f^2}\phi(z) = 0, \tag{3.87}$$

with boundary conditions $\phi(0) = \phi(-H) = 0$. We continue our analysis by first considering the case of constant N and subsequently the case of non-constant $N(z)$.

Constant N

When the temperature is distributed linearly, N is constant. We can easily obtain the value of N from the distribution of the temperature profile,

$$N^2 = g\alpha_T \frac{d\bar{T}(z)}{dz}. \tag{3.88}$$

For a constant N, we define

$$K = \alpha^2 \frac{N^2 - \omega^2}{\omega^2 - f^2}. \tag{3.89}$$

If $(N^2 - \omega^2)/(\omega^2 - f^2) < 0$, the general solution of (3.87) is

$$\phi(z) = c_1 e^{\sqrt{-K}z} + c_2 e^{-\sqrt{-K}z}, \tag{3.90}$$

where c_1 and c_2 are arbitrary constants. Applying the boundary conditions $\phi(0) = \phi(-H) = 0$ gives the solution $\phi(z) \equiv 0$, which we are not interested in. If $(N^2 - \omega^2)/(\omega^2 - f^2) > 0$, by defining

$$m = \sqrt{K} = \alpha\sqrt{\frac{N^2 - \omega^2}{\omega^2 - f^2}}, \tag{3.91}$$

we can easily solve (3.87) and the solution is

$$\phi(z) = \sin(mz). \tag{3.92}$$

For the first vertical mode $m = \pi/H$, and this gives us the relationship between α and ω. The eigenvalue problem is now reduced to

$$\frac{fn}{r_0} J_n(\alpha r_0) - \omega\alpha J_n'(\alpha r_0) = 0. \tag{3.93}$$

Defining dimensionless variables $\Omega = \omega/f$, $N^* = N/f$, (3.93) can be nondimensionalized as follows,

$$nJ_n(\alpha r_0) - \Omega\alpha r_0 J_n'(\alpha r_0) = 0, \tag{3.94}$$

where $\alpha = m\sqrt{\frac{\Omega^2 - 1}{(N^*)^2 - \Omega^2}}$. Defining the function

$$G(\Omega) = nJ_n(\alpha r_0) - \Omega\alpha r_0 J_n'(\alpha r_0), \tag{3.95}$$

we plot $G(\Omega)$ versus Ω for different values of N^* and r_0. For $H = 50$ m, $m = \pi/H$, $f = 10^{-4}$ s^{-1}, $N^* = 198$, we plot $G(\Omega)$ using $r_0 = 5, 10, 20, 40$ km, (Fig. 3.2). The zeros of $G(\Omega)$ decrease when r_0 increases in $\Omega \in (1, 5)$. With values of H, m, and f unchanged, we fix $r_0 = 20$ km, and vary $N^* = 50$, $N^* = 100$, $N^* = 500$ and $N^* = 1000$ (Fig. 3.3). The zeros of $G(\Omega)$ decrease when N^* increases in $\Omega \in (1, 5)$.

Non-constant $N(z)$

When $N(z)$ is not a constant we have two eigenvalues, ω and α, to find. In the limit of the thermocline thickness d going to zero, a two-layer model is obtained, for which the boundary value problem can be solved analytically. The solution gives an initial guess of our eigenvalues, which will be especially useful when we deal with a thin thermocline.

We start with the background temperature distribution,

$$\bar{T}(z) = T_b + \left(\frac{T_s - T_b}{2}\right)\left[1 + \tanh(\frac{z - z_0}{d})\right], \tag{3.96}$$
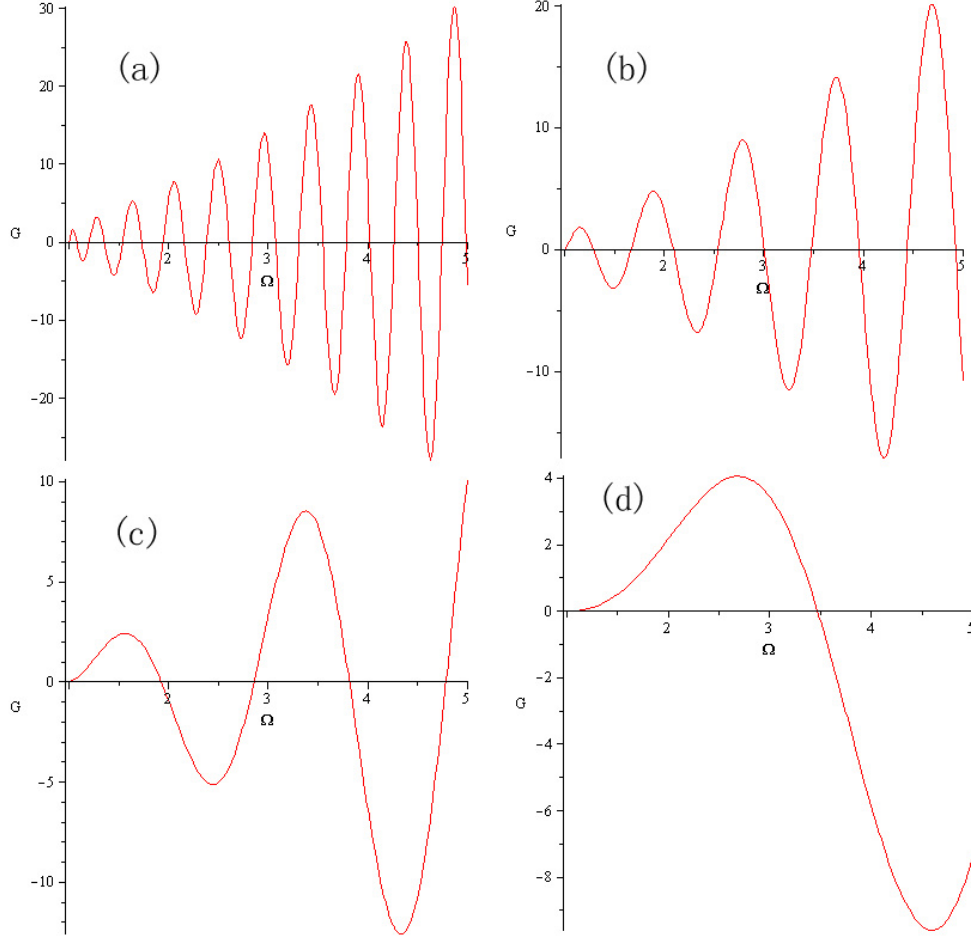
Figure 3.2: $G(\Omega)$ plots in the eigenvalue problem in case I with a constant $N^* = 198$, for different r_0 values: (a) $r_0 = 40$ km, (b) $r_0 = 20$ km, (c) $r_0 = 10$ km, and (d) $r_0 = 5$ km.

and

$$N^2(z) = g\alpha_T \frac{d\bar{T}(z)}{dz} = g\alpha_T \frac{T_s - T_b}{2d}\text{sech}^2\left(\frac{z - z_0}{d}\right). \tag{3.97}$$

As $d \to 0$,

$$\bar{T}(z) \to T_b + (T_s - T_b)H(z - z_0),$$

where $H(z)$ is Heaviside step function, and

$$N^2(z) \to g'\delta(z - z_0),$$

where $\delta(z)$ is the delta function which is the derivative of the Heaviside step function, and g' is defined as $g' = g\alpha_T(T_s - T_b)$. Substituting $N^2(z)$ into equation (3.87) leads to

$$\phi''(z) + \alpha^2 \frac{g'\delta(z - z_0) - \omega^2}{\omega^2 - f^2}\phi(z) = 0, \tag{3.98}$$

28
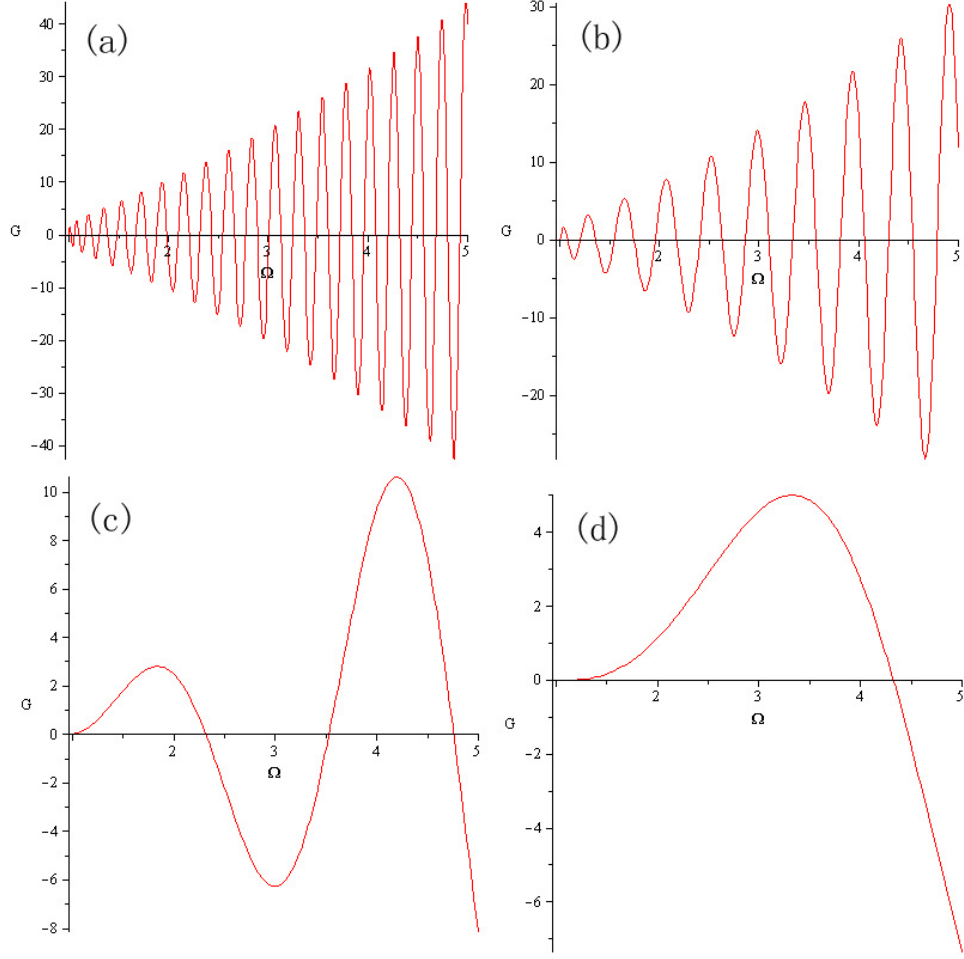
Figure 3.3: $G(\Omega)$ plots in the eigenvalue problem in case I with a constant $r_0 = 20$ km, for different N^* values: (a) $N^* = 50$, (b) $N^* = 100$, (c) $N^* = 500$, and (d) $N^* = 1000$.

with $\phi(0) = \phi(-H) = 0$.

When $-H \leq z < z_0$, $\delta(z - z_0) = 0$, we get

$$\phi''(z) - \frac{\alpha^2 \omega^2}{\omega^2 - f^2} \phi(z) = 0, \tag{3.99}$$

with $\phi(-H) = 0$. The solution of this ODE is

$$\phi(z) = a \sinh(M(z + H)), \tag{3.100}$$

where $M^2 = \frac{\alpha^2 \omega^2}{\omega^2 - f^2}$ and a is an arbitrary constant. For now we assume $\omega > f$. When $z_0 < z \leq 0$, $\delta(z - z_0) = 0$, we obtain

$$\phi''(z) - \frac{\alpha^2 \omega^2}{\omega^2 - f^2} \phi(z) = 0, \tag{3.101}$$

29

with $\phi(0) = 0$. The general solution of this ODE is

$$\phi(z) = b\sinh(Mz), \tag{3.102}$$

where b is an arbitrary constant. Since $\phi(z)$ is continuous at $z = z_0$, we have

$$a\sinh(M(z_0 + H)) = b\sinh(Mz_0). \tag{3.103}$$

If we define $z_0 = -h_1$, $H = h_1 + h_2$, where h_1 and h_2 are the thickness of upper and lower layer, we can write this as

$$b = -\frac{\sinh(Mh_2)}{\sinh(Mh_1)}a. \tag{3.104}$$

From (3.100) and (3.102) we write $\phi(z)$ as

$$\phi(z) = a\sinh(M(z + H)) + [b\sinh(Mz) - a\sinh(M(z + H))]H(z - z_0). \tag{3.105}$$

Differentiating equation (3.100) and (3.102) with respect to z yields,

$$\phi'(z) = \begin{cases} aM\cosh(M(z + H)) & \text{if } -H \le z < z_0, \\ bM\cosh(Mz) & \text{if } z_0 < z \le 0. \end{cases} \tag{3.106}$$

Then we rewrite $\phi'(z)$ as

$$\phi'(z) = aM\cosh(M(z + H)) + [bM\cosh(Mz) - aM\cosh(M(z + H))]H(z - z_0). \tag{3.107}$$

Differentiating this with respect to z gives,

$$\begin{aligned} \phi''(z) =& aM^2\sinh(M(z + H)) + [bM^2\sinh(Mz) - aM^2\sinh(M(z + H))]H(z - z_0) \\ &+ [bM\cosh(Mz) - aM\cosh(M(z + H))]\delta(z - z_0). \end{aligned} \tag{3.108}$$

Note that the sum of the first two parts is $M^2\phi(z)$, hence (3.108) becomes,

$$\phi''(z) = M^2\phi(z) + [bM\cosh(Mz) - aM\cosh(M(z + H))]\delta(z - z_0). \tag{3.109}$$

Substituting $\phi''(z)$ into equation (3.98) leads to,

$$[bM\cosh(Mz) - aM\cosh(M(z + H))]\delta(z - z_0) + \frac{M^2 g'}{\omega^2}\delta(z - z_0)\phi(z) = 0, \tag{3.110}$$

which implies that,

$$bM\cosh(Mz_0) - aM\cosh(M(z_0 + H)) + \frac{M^2 g'}{\omega^2}\phi(z_0) = 0. \tag{3.111}$$

We know

$$\phi(z_0) = a\sinh(M(z_0 + H)) = a\sinh(Mh_2). \tag{3.112}$$

30

Substituting b from (3.104) results of

$$\frac{g'M}{\omega^2}\sinh(Mh_1)\sinh(Mh_2) = \sinh(MH), \tag{3.113}$$

where $M = \frac{\alpha\omega}{\sqrt{\omega^2 - f^2}}$ with $\omega > f$.

Therefore, if $\omega > f$ the eigenvalue problem (3.86) and (3.87) becomes a system of equations

$$\frac{fn}{r_0}J_n(\alpha r_0) - \omega\alpha J'_n(\alpha r_0) = 0, \tag{3.114}$$

$$\frac{g'M}{\omega^2}\sinh(Mh_1)\sinh(Mh_2) - \sinh(MH) = 0, \tag{3.115}$$

where $M = \frac{\alpha\omega}{\sqrt{\omega^2 - f^2}}$ with $\omega > f$ and $g' = g\alpha_T(T_s - T_b)$.

Next we will solve the system numerically. Defining F_1 and F_2 as the left hand sides of (3.114) and (3.115) respectively, zero contour plots of F_1 and F_2 are made in the domain $\omega \in [1.01 \times 10^{-4}, 4 \times 10^{-4}]$ and $\alpha \in [10^{-4}, 10^{-3}]$. From these, the intersections give the desired solutions. If $f = 10^{-4}$ s^{-1}, $n = 1$, $H = 50$ m, $h_1 = 15$ m, and $h_2 = 35$ m, we plot the zero contours of both functions for different values of r_0 (Fig. 3.4). In the plots, the zero contour of function F_2 does not depend on r_0, which is trivial since there is no r_0 in (3.115). For large values of r_0 the zero contours of F_1 are nearly independent of ω, and there are more intersections between the two sets of contours.

While if $\omega < f$, we can use the results to find out the new eigenvalue problem by defining $M = iM^\star$. Substituting M into equation (3.113), and using the relation $\sinh(ix) = i\sin(x)$, we obtain

$$-\frac{g'M^\star}{\omega^2}\sin(M^\star h_1)\sin(M^\star h_2) = \sin(M^\star H), \tag{3.116}$$

where $M^\star = \frac{\alpha\omega}{\sqrt{f^2 - \omega^2}}$ with $\omega < f$. Hence the eigenvalue problem becomes,

$$\frac{fn}{r_0}J_n(\alpha r_0) - \omega\alpha J'_n(\alpha r_0) = 0, \tag{3.117}$$

$$\frac{g'M^\star}{\omega^2}\sin(M^\star h_1)\sin(M^\star h_2) + \sin(M^\star H) = 0, \tag{3.118}$$

where $M^\star = \frac{\alpha\omega}{\sqrt{f^2 - \omega^2}}$ with $\omega < f$ and $g' = g\alpha_T(T_s - T_b)$.

Now using the same method as $\omega > f$ case, we try to find the numerical solutions for $\omega < f$ case. It turns out that we cannot find any solution for this case numerically. Therefore, for case I, only $\omega > f$ is permitted.

31
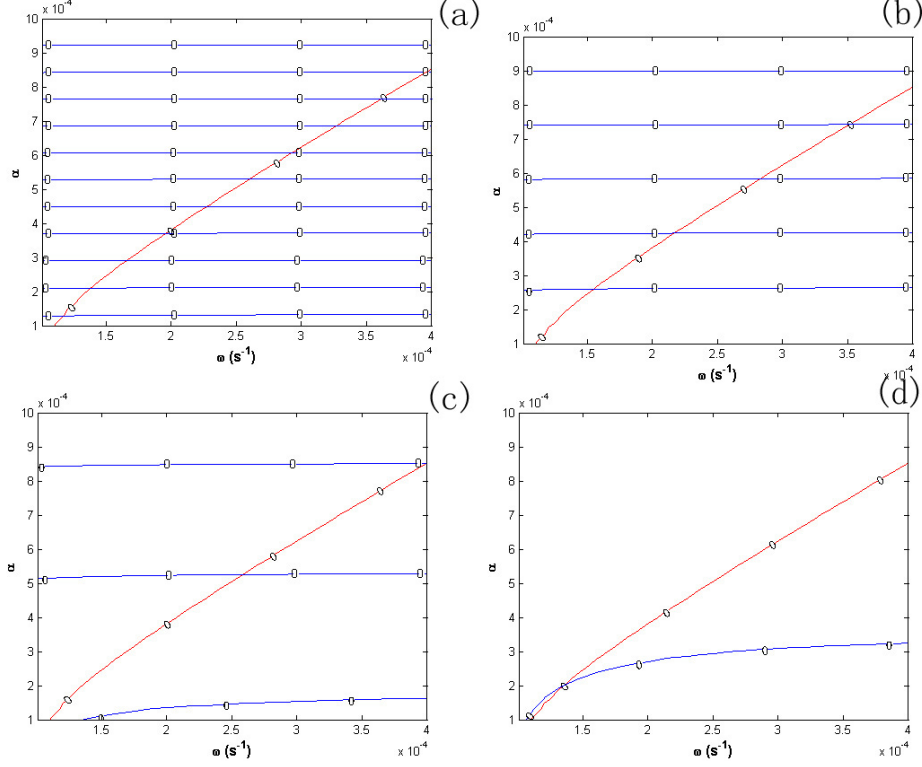
Figure 3.4: Zero contours plots in case I with non-constant $N(z)$ for different r_0 values: (a) $r_0 = 40$ km, (b) $r_0 = 20$ km, (c) $r_0 = 10$ km, and (d) $r_0 = 5$ km. Zero contours of function F_1 is in blue, while the ones for F_2 is in red.

3.4.2   Case II: $C = \beta^2 > 0$

For case II, we are solving the eigenvalue problem

$$\frac{fn}{r_0}I_n(\beta r_0) - \omega\beta I_n'(\alpha r_0) = 0, \tag{3.119}$$

$$\phi''(z) - \beta^2\frac{N^2(z) - \omega^2}{\omega^2 - f^2}\phi(z) = 0, \tag{3.120}$$

with boundary conditions $\phi(0) = \phi(-H) = 0$.

Constant N

If $(N^2 - \omega^2)/(\omega^2 - f^2) > 0$, (3.120) with the boundary conditions gives the trivial solution $\phi(z) \equiv 0$. If $(N^2 - \omega^2)/(\omega^2 - f^2) < 0$, we solve equation (3.120) and obtain

$$\phi(z) = \sin(\tilde{m}z), \tag{3.121}$$

where $\tilde{m} = \beta\sqrt{\frac{N^2-\omega^2}{f^2-\omega^2}}$. For the first vertical mode, we have $\tilde{m} = \pi/H$. Similarly to case I define dimensionless variables $\Omega = \omega/f$, $N^* = N/f$, and

$$G(\Omega) = nI_n(\beta r_0) - \Omega\beta r_0 I_n'(\beta r_0), \tag{3.122}$$

where $\beta = \tilde{m}\sqrt{\frac{1-\Omega^2}{(N^*)^2-\Omega^2}}$.

We now plot $G(\Omega)$ versus Ω for different values of N^* and r_0. For $H = 50$ m, $\tilde{m} = \pi/H$ m^{-1}, $f = 10^{-4}$ s^{-1}, $N^* = 198$, we plot $G(\Omega)$ using $r_0 = 40$ km, $r_0 = 20$ km, $r_0 = 10$ km, and $r_0 = 5$ km (Fig. 3.5). The zero of $G(\omega)$ moves towards 1 when r_0 increases in $\Omega \in (0.01, 0.9)$. In fact, approximately when $r_0 < 4.5$ km, there is no solution for Ω. With values of H, m, and f unchanged, we fix $r_0 = 20$ km, and vary $N^* = 50$, $N^* = 100$, $N^* = 500$, and $N^* = 1000$ (Fig. 3.6). The solution of $G(\omega) = 0$ moves towards 1 when N^* increases in $\Omega \in (0.01, 0.9)$. After a simple check by Maple, there is no solution for Ω when $N^* > 900$ approximately.
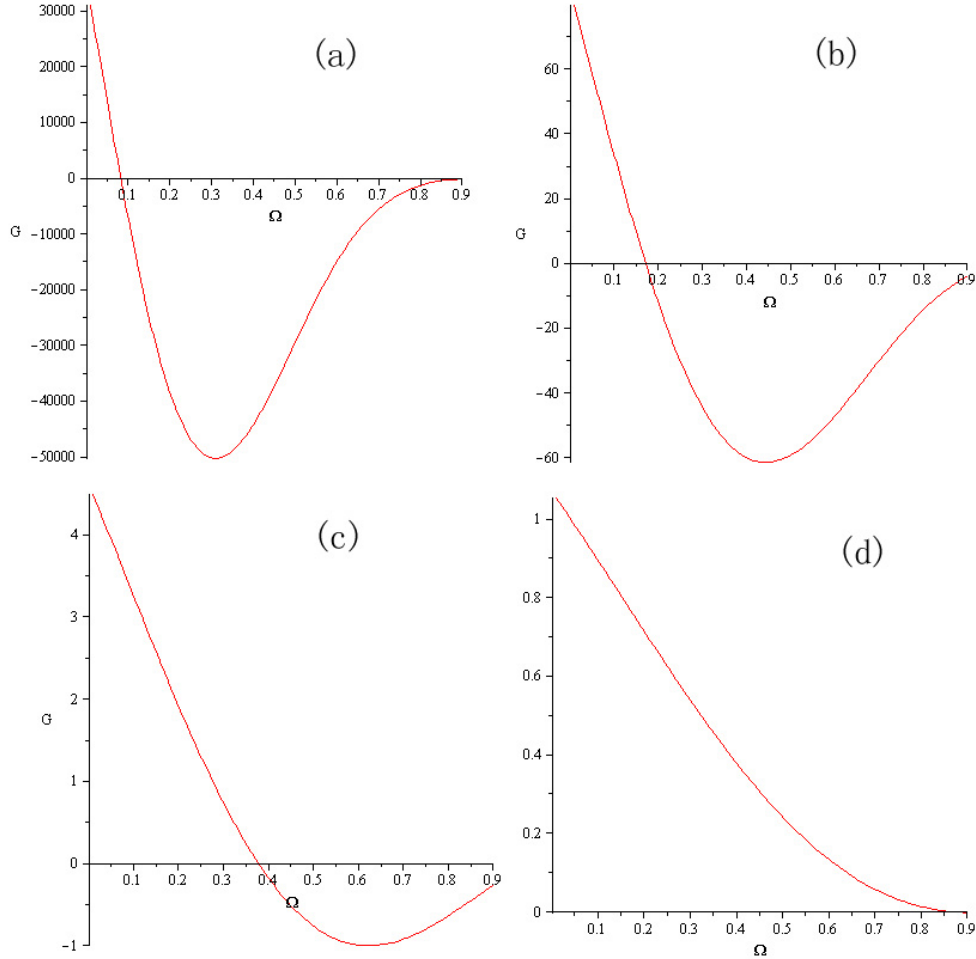
Figure 3.5: $G(\Omega)$ plots in the eigenvalue problem in case II with constant $N^* = 198$, for different r_0 values: (a) $r_0 = 40$ km, (b) $r_0 = 20$ km, (c) $r_0 = 10$ km, and (d) $r_0 = 5$ km.
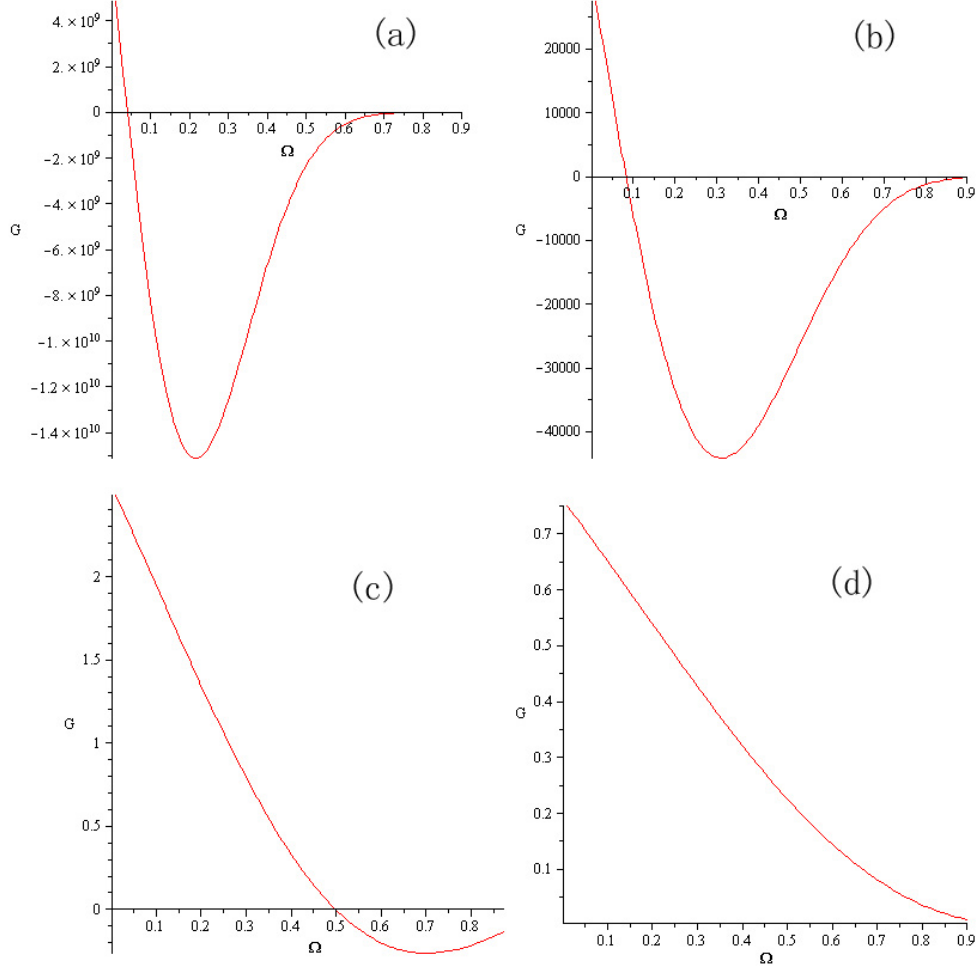
Figure 3.6: $G(\Omega)$ plots in the eigenvalue problem in case II with a constant $r_0 = 20$ km, for different N^* values: (a) $N^* = 50$, (b) $N^* = 100$, (c) $N^* = 500$, and (d) $N^* = 1000$.

Non-constant $N(z)$

Similar to case I, we start with two-layer analysis. It basically follows the same steps as case I with $\beta^2 = -\alpha^2$. Let $\alpha = \beta i$, then in the results of case I (3.114) to (3.118), $M = \frac{i\beta\omega}{\sqrt{\omega^2 - f^2}} = i\gamma$, with definition

$$\gamma = \frac{\beta\omega}{\sqrt{\omega^2 - f^2}}, \tag{3.123}$$

and $M^\star = \frac{i\beta\omega}{\sqrt{f^2 - \omega^2}} = i\gamma^\star$, with definition

$$\gamma^\star = \frac{\beta\omega}{\sqrt{f^2 - \omega^2}}, \tag{3.124}$$

Substituting $\alpha = i\beta$, $M = i\gamma$, and $M^\star = i\gamma^\star$ into equation (3.114) to (3.118), and using the property $J_n(ix) = i^n I_n(x)$, $\sinh(ix) = i\sin(x)$, and $\sin(ix) = i\sinh(x)$,

34

we have the two-layer approximation of eigenvalue problem for case II as follows. If $\omega > f$,

$$\frac{fn}{r_0} I_n(\beta r_0) - \omega\beta I_n'(\beta r_0) = 0, \tag{3.125}$$

$$\frac{g'\gamma}{\omega^2} \sin(\gamma h_1) \sin(\gamma h_2) + \sin(\gamma H) = 0, \tag{3.126}$$

where $\gamma = \frac{\beta\omega}{\sqrt{\omega^2 - f^2}}$ and $g' = g\alpha_T(T_s - T_b)$.
While if $\omega < f$,

$$\frac{fn}{r_0} I_n(\beta r_0) - \omega\beta I_n'(\beta r_0) = 0, \tag{3.127}$$

$$\frac{g'\gamma^\star}{\omega^2} \sinh(\gamma^\star h_1) \sinh(\gamma^\star h_2) - \sinh(\gamma^\star H) = 0, \tag{3.128}$$

where $\gamma^\star = \frac{\beta\omega}{\sqrt{f^2 - \omega^2}}$ and $g' = g\alpha_T(T_s - T_b)$.

Using the same method as case I, next we try to find the numerical solutions of the system. If $\omega < f$, again defining G_1 and G_2 is the left hand side of (3.127) and (3.128) respectively, zero contour plots of G_1 and F_2 are made in the domain $\omega \in (10^{-6}\ 9.9 \times 10^{-5})$ and $\beta \in (10^{-5}, 10^{-3})$. Given $f = 10^{-4}$ s^{-1}, $n = 1$, $H = 50$ m, $h_1 = 15$ m, and $h_2 = 35$ m, we plots the zero contours of both functions for different values of r_0 (Fig. 3.7). As r_0 decreases, eigenvalue ω moves towards to $f = 10^{-4}$ s^{-1}. When $r_0 = 5$ km, there is no solution for the system. On the other hand, when $\omega > f$, we cannot find any solution numerically using the method we described. Therefore, for case II, only $\omega < f$ is permitted, as opposite to case I.
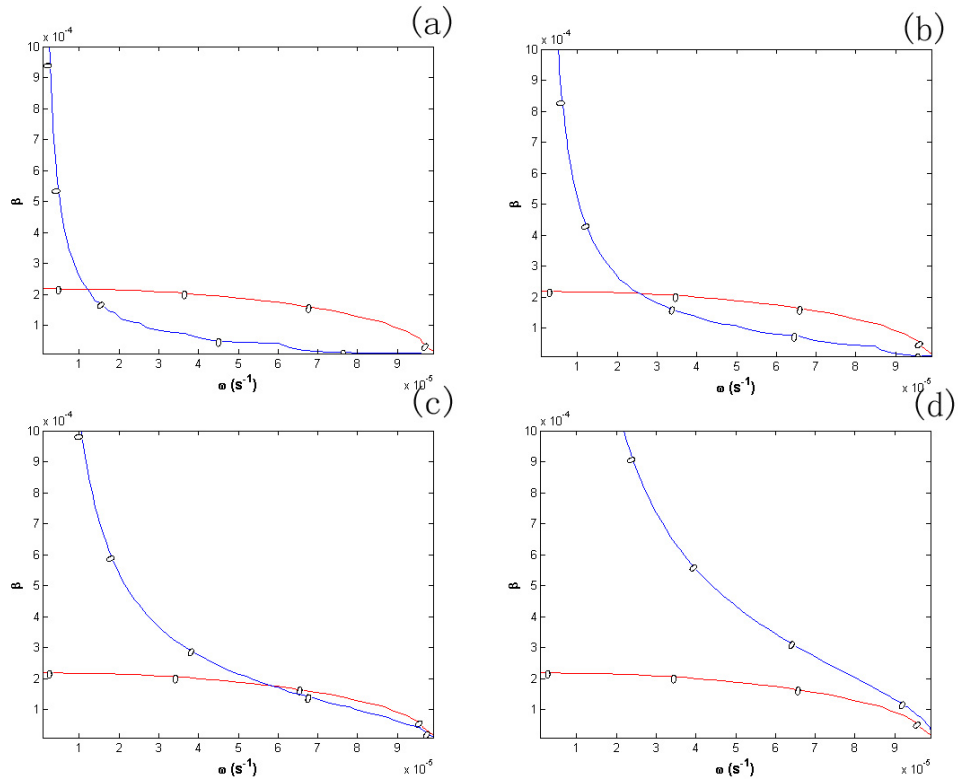
Figure 3.7: Zero contours plots in case II with non-constant $N(z)$ for different r_0 values: (a) $r_0 = 40$ km, (b) $r_0 = 20$ km, (c) $r_0 = 10$ km, and (d) $r_0 = 5$ km. Zero contours of function G_1 is in blue, while the ones for G_2 is in red.

Chapter 4

Numerical Model

4.1   Introduction to MITgcm

The MITgcm (MIT General Circulation Model) is a numerical model designed for the study of the atmosphere, ocean, and climate. The MITgcm has a number of novel aspects. It can be used to study both atmospheric and oceanic phenomena (Fig. 4.1). It has a non-hydrostatic capability and so can be used to study both
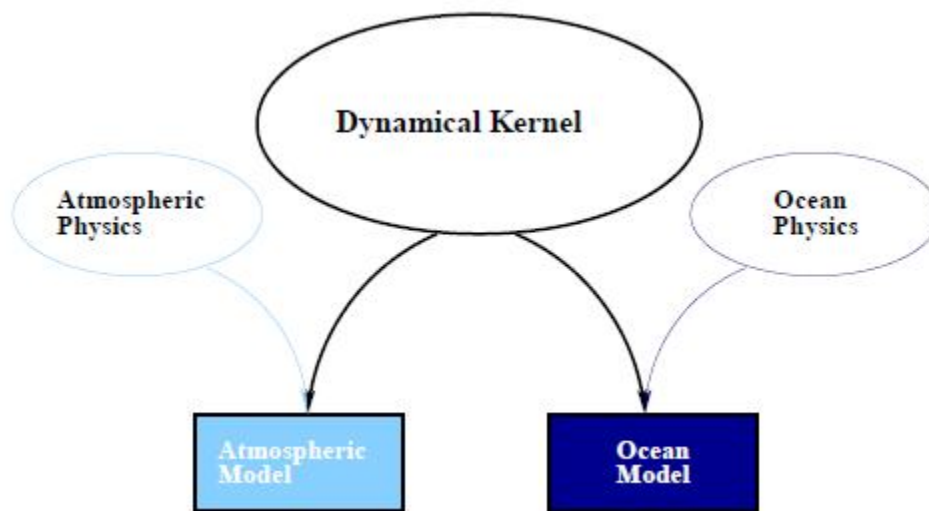
Figure 4.1: MITgcm has a single dynamical kernel that can perform either oceanic or atmospheric simulations (from Adcroft et al. 2008).

small-scale and large-scale processes (Fig. 4.2). Finite volume techniques are employed yielding an intuitive discretization and support for the treatment of irregular geometries. Also the model is developed to perform efficiently on a wide variety of computational platforms. There are many key publications on the development of the model, e.g., Marshall et al. (1997a,b), Adcroft et al. (1997) and Marshall et al. (2004) etc.
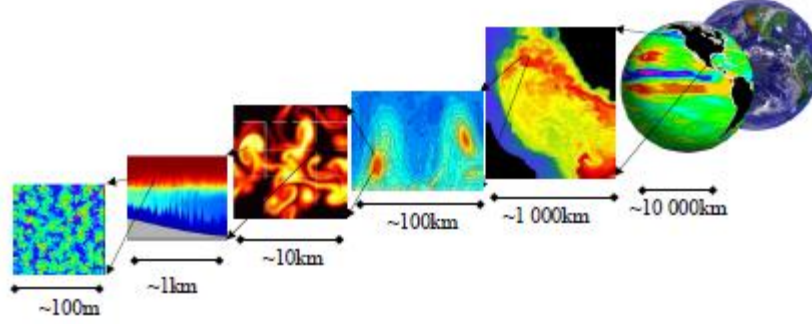
Figure 4.2: MITgcm has non-hydrostatic capabilities, allowing the model to address a wide range of phenomenon – from convection on the left, all the way through to global circulation patterns on the right (from Adcroft et al. 2008).

4.2   First Application of MITgcm: Tilted Tank

We begin our applications of MITgcm model with a tilted tank simulation. This has been studied in detail in many references e.g. Horn et al. (2001) and Boegman et al. (2005). The results are compared with the simulations done by Dr. Kevin Lamb's Internal Gravity Waves model (IGW).

The tank we choose is 12 meter long, 0.3 meter high, and 0.06 meter wide. It is fully filled with water of different densitie, using a layer of warm water overlying a layer of cold water. The titled thermocline has the form

$$T(x,z) = T_b + \frac{T_s - T_b}{2}\Big[1 + \tanh\Big(\frac{z - z_0 - \gamma x}{d}\Big)\Big], \tag{4.1}$$

where $T_b = 10\,°C$ and $T_s = 20\,°C$ are the temperatures of the bottom water and surface water, $z_0 = -0.1$ m is the position of the thermocline at $x = 0$ and and $d = 0.02$ m is the the thickness of the thermocline, z ranges from 0 to -0.3 m, x ranges from 0 to 12 m, and $\gamma = 0.005$ is a parameter to determine the slope of the thermocline. Fig. 4.3 shows the initial temperature distribution.

The fluid is initially tilted at rest and then evolves freely. In Horn et al. (2001), by assuming a two-layer model and comparing the timescales over which each of these degeneration mechanisms acts, regimes are defined in Fig. 4.4. The boundaries of these regimes are expressed in terms of two length scale ratios: the ratio of the amplitude of the initial wave to the depth of the thermocline, and the ratio of the depth of the thermocline to the overall depth of the lake. In our run it is easy to work out the amplitude $\eta_0 \approx 0.03$ m, the thickness of the upper layer $h_1 \approx 0.07$ m, and the lower layer $h_2 \approx 0.23$ m. Hence $W^{-1} = \eta_0/h_1 \approx 0.43$ and $h_1/H \approx 0.23$, where W^{-1} is the Wedderburn number (Thompson and Imberger 1980). From the regime plot in Fig. 4.4, we expect solitary waves from the simulations. The problem is 2D, while we are using a 3D simulation with each layer in y direction being identical. The resolution is $800 \times 5 \times 80$ in x, y, and z direction, and the
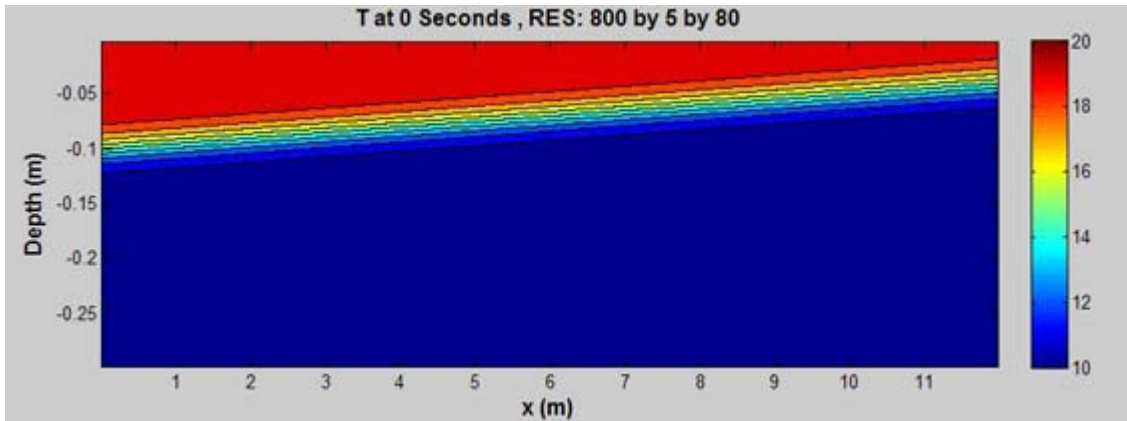
Figure 4.3: The initial temperature profile of the tilted tank simulation in x-z plane
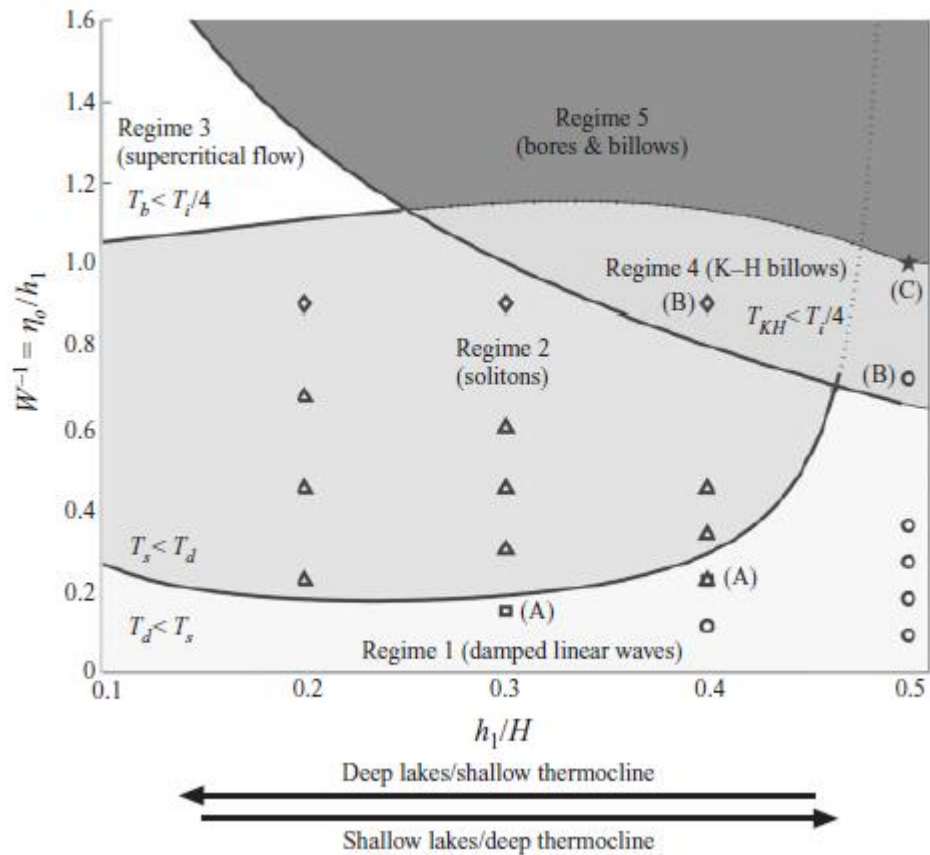
Figure 4.4: The regimes of the degeneration of internal waves in two-layer fluids. (from Horn et al. 2001)

time step is 0.1 s. The viscosity and diffusivity are both zero. In order to make the comparison of the schemes, we do not use any turbulence models and numerical filters here. Fig. 4.5 and Fig. 4.6 show the time evolution of the tilted interface from 0 to 2000 s with temperature advection scheme code set to be 2. There are several temperature advection schemes in MITgcm model. The comparison is made in Table 4.1, with the results for each schemes at $t = 1000$ s and 2000 s from Fig. 4.7 to Fig. 4.10. Here the horizontal and vertical schemes have the same code, i.e., if we set TempAdvScheme = 1 in the model, then both horizontal and vertical scheme codes are 1 by default, and we do not test mixed schemes here.

In summary, schemes 2 and 33 provide good results in our tank simulation in the absence of viscosity and diffusivity, and the results using schemes 3 and 4 are OK, while schemes 1, 20, 30, and 77 give unreasonable output.

Next, we run the same simulation in the IGW model. The numerical scheme in IGW uses a second-order Godunov upwind scheme with a monotonized slope computation which provides selective numerical dissipation and diffusion near sharp gradients. Fig. 4.11 and 4.12 show the time evolution of the tilted interface from 0 to 2000 s. Comparing to Fig. 4.5 and 4.6, two results are almost the same except that the wave speed in the MITgcm seems a bit larger than in the IGW. We will continue to investigate the difference of the speeds in future work.

Table 4.1: Advection schemes comparison in the MITgcm in the tilted tank simulation

code	Scheme	MITgcm Manual	MITgcm Run
1	1st upwind	It is very diffusive and does not provide more useful results than the positive higher order schemes.	It is very diffusive as expected.
2	2nd centered	It is noisy and must be used with finite amount of diffusion.	The result is not noisy through the first 2000 s, but some noise appears after that.
3	3rd upwind	It is relatively good compromise between accuracy and smoothness.	The result is almost identical to scheme 2 except that there is noise at the top and bottom near $t = 2000$ s.
4	4th centered	It is the most accurate scheme. Like scheme 2, it is noisy and must be used with some finite amount of diffusion.	It is almost identical to scheme 2, except it is noisier.
20	2nd DST	2nd DST (direct space time) deals with space and time discretization together.	It is one of the worst in all simulations because it is very noisy.
30	3rd DST	3rd order direct space time scheme.	It is very noisy and has overshoots.
33	3rd DST with flux limiting.	The flux limiting is to avoid the spurious oscillations that would otherwise occur with high order spatial discretization schemes due to shocks, discontinuities or sharp changes in the solution domain. The overshoots in 3rd order DST can be controlled with a flux limiter.	With the flux limiting, there is no noise compared to scheme 30. The problem with overshoots is solved as expected.
77	2nd flux limiter	2nd order with flux limiter	The result is unusual because the thermocline is shrinking instead of diffusing.
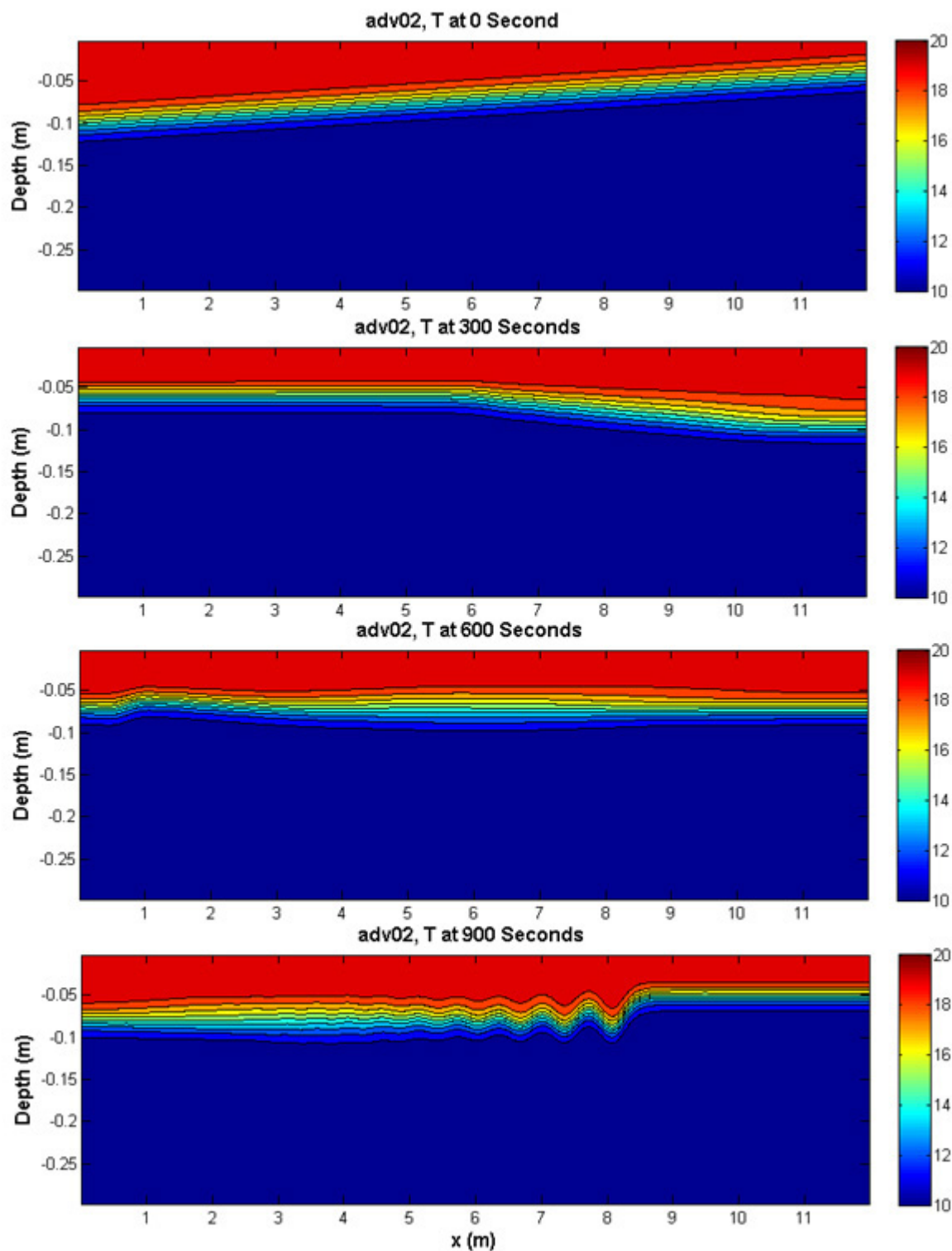
Figure 4.5: Temperature distribution on x-z plane at $t = 0$ s, 300 s, 600 s and 900 s using scheme 2
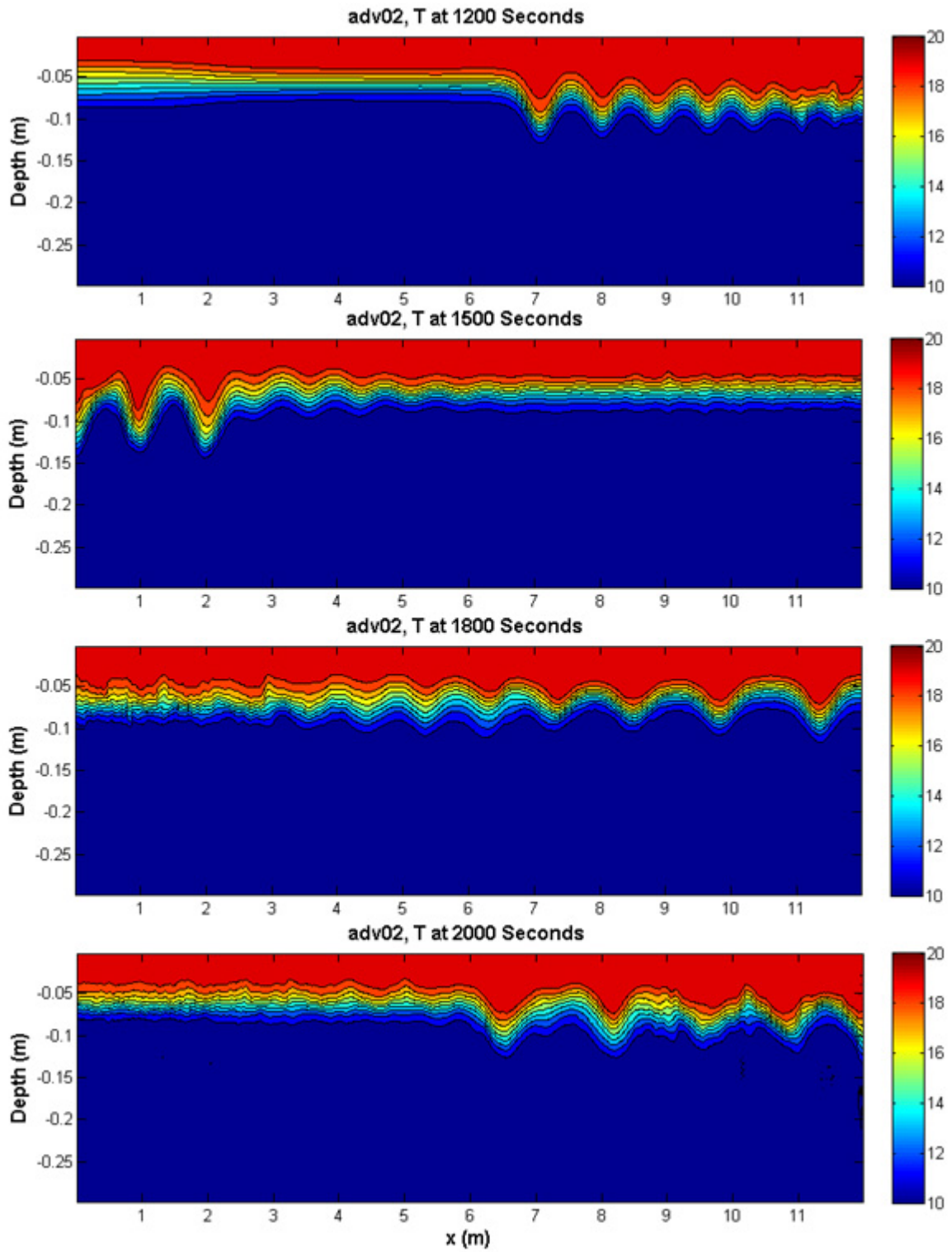
Figure 4.6: Temperature distribution on x-z plane at $t = 1200$ s, 1500 s, 1800 s and 2000 s using scheme 2
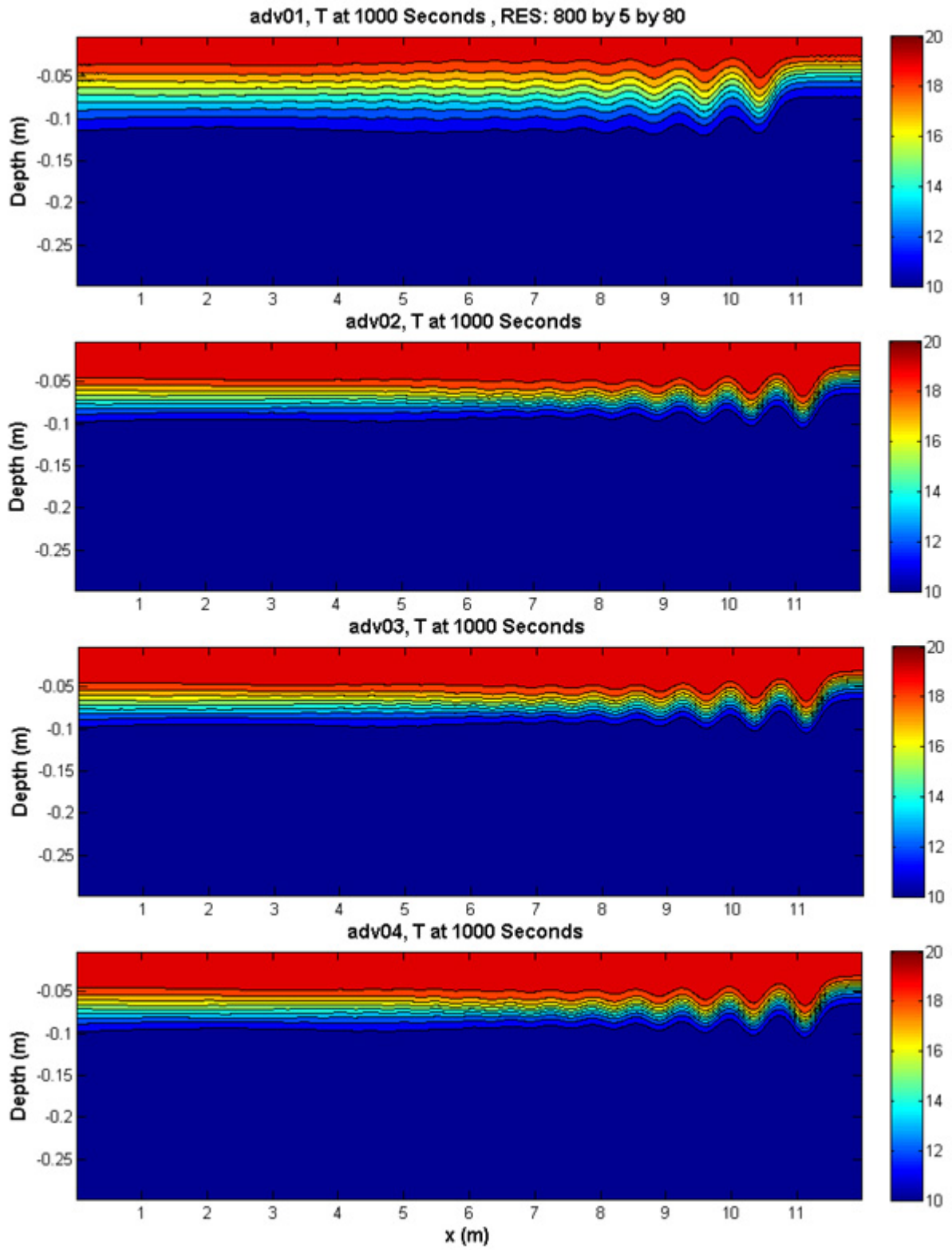
Figure 4.7: Temperature advection schemes comparison at $t = 1000$ s (schemes 1, 2, 3, 4)
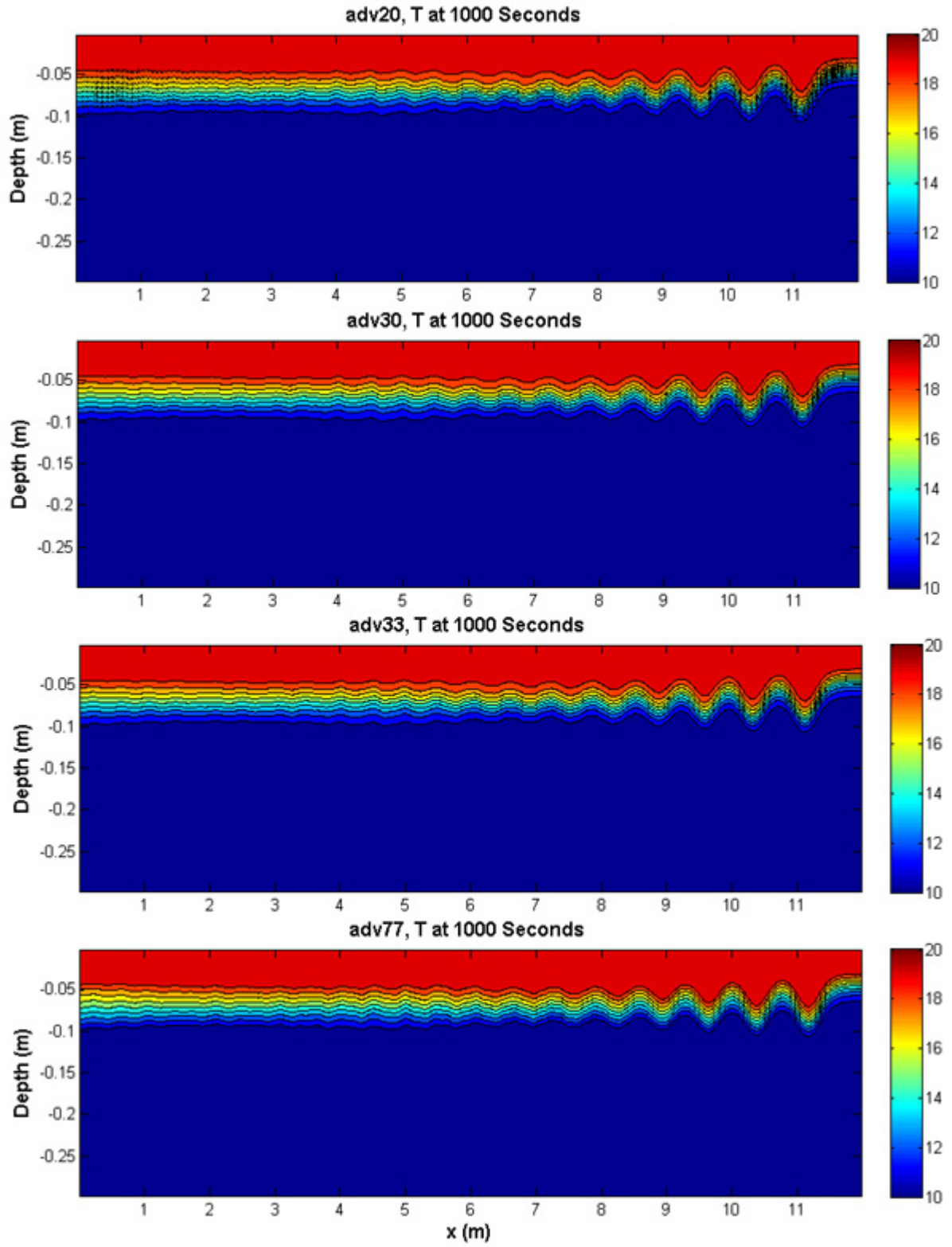
Figure 4.8: Temperature advection schemes comparison at $t = 1000$ s (schemes 20, 30, 33, 77)
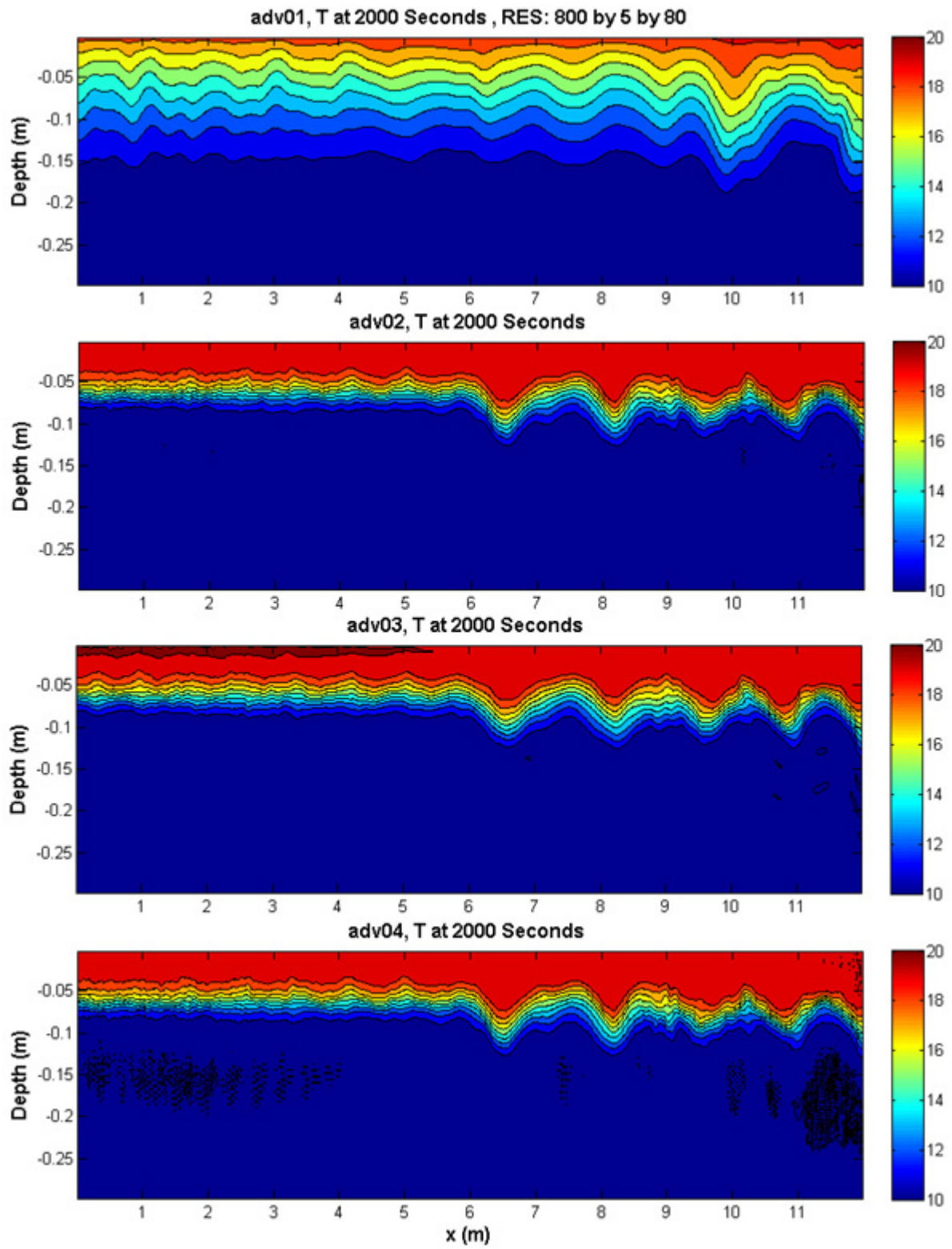
Figure 4.9: Temperature advection schemes comparison at $t = 2000$ s (schemes 1, 2, 3, 4)
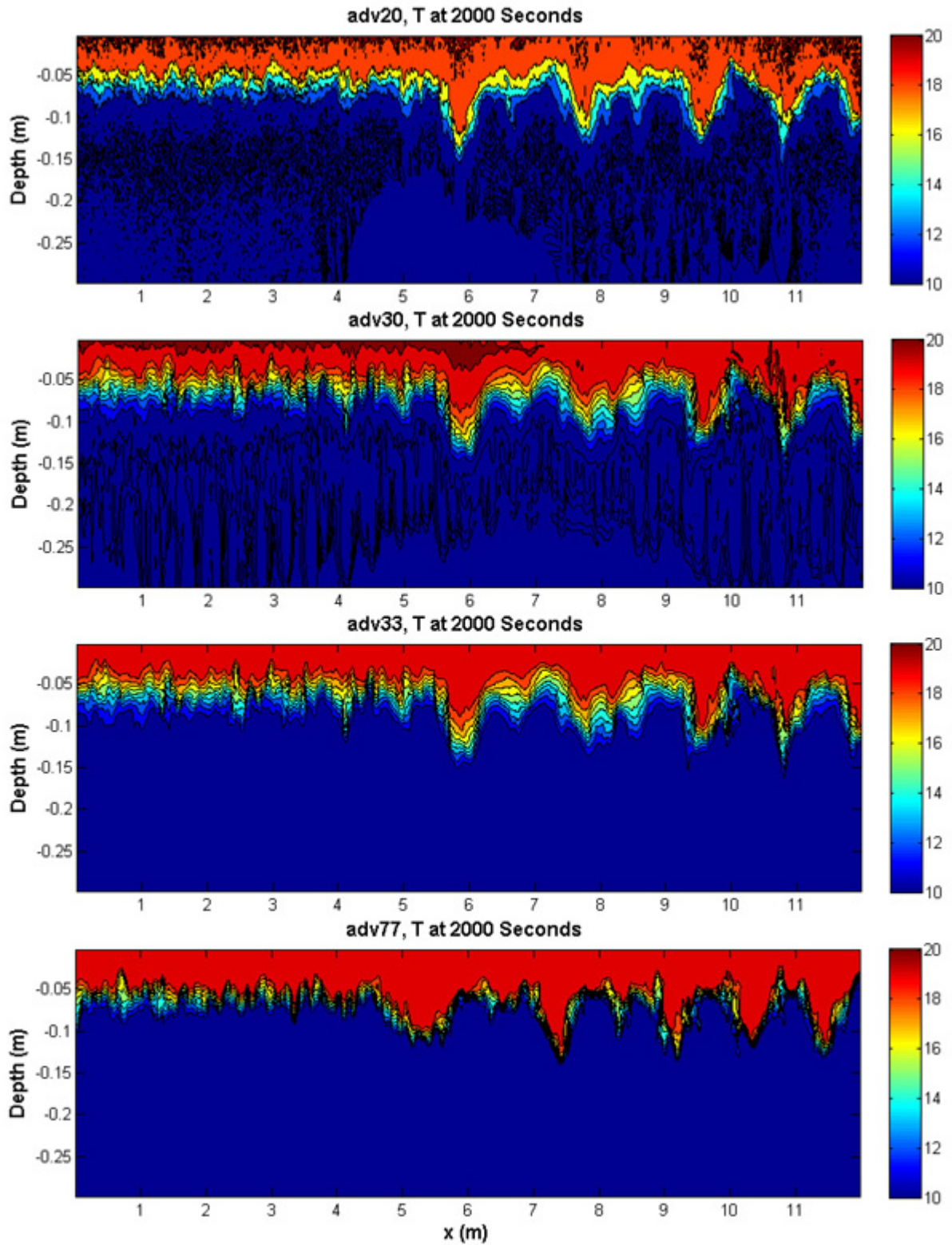
Figure 4.10: Temperature advection schemes comparison at $t = 2000$ s (schemes 20, 30, 33, 77)
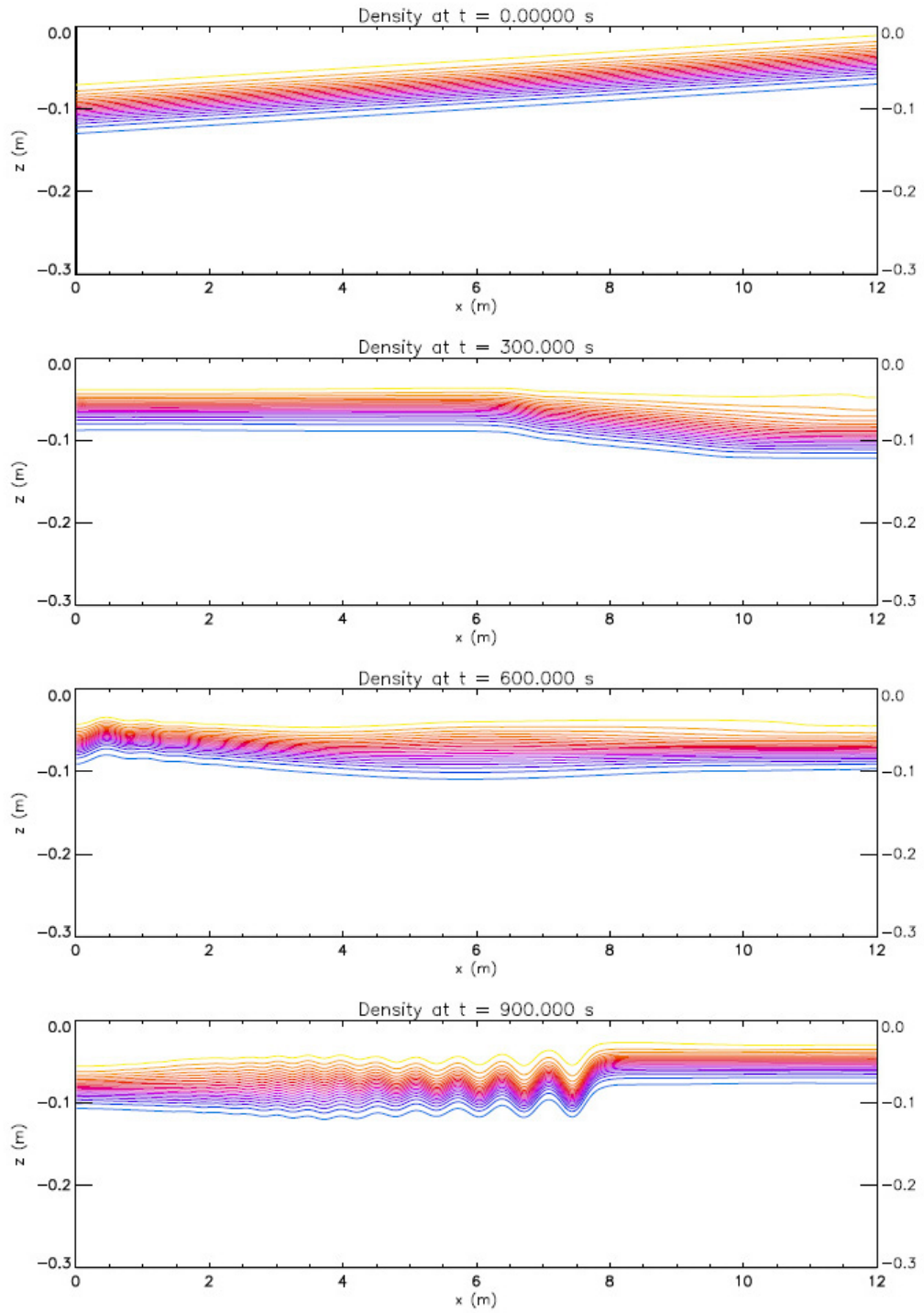
Figure 4.11: Temperature on x-z plane at $t = 0$ s, 300 s, 600 s and 900 s using the IGW model
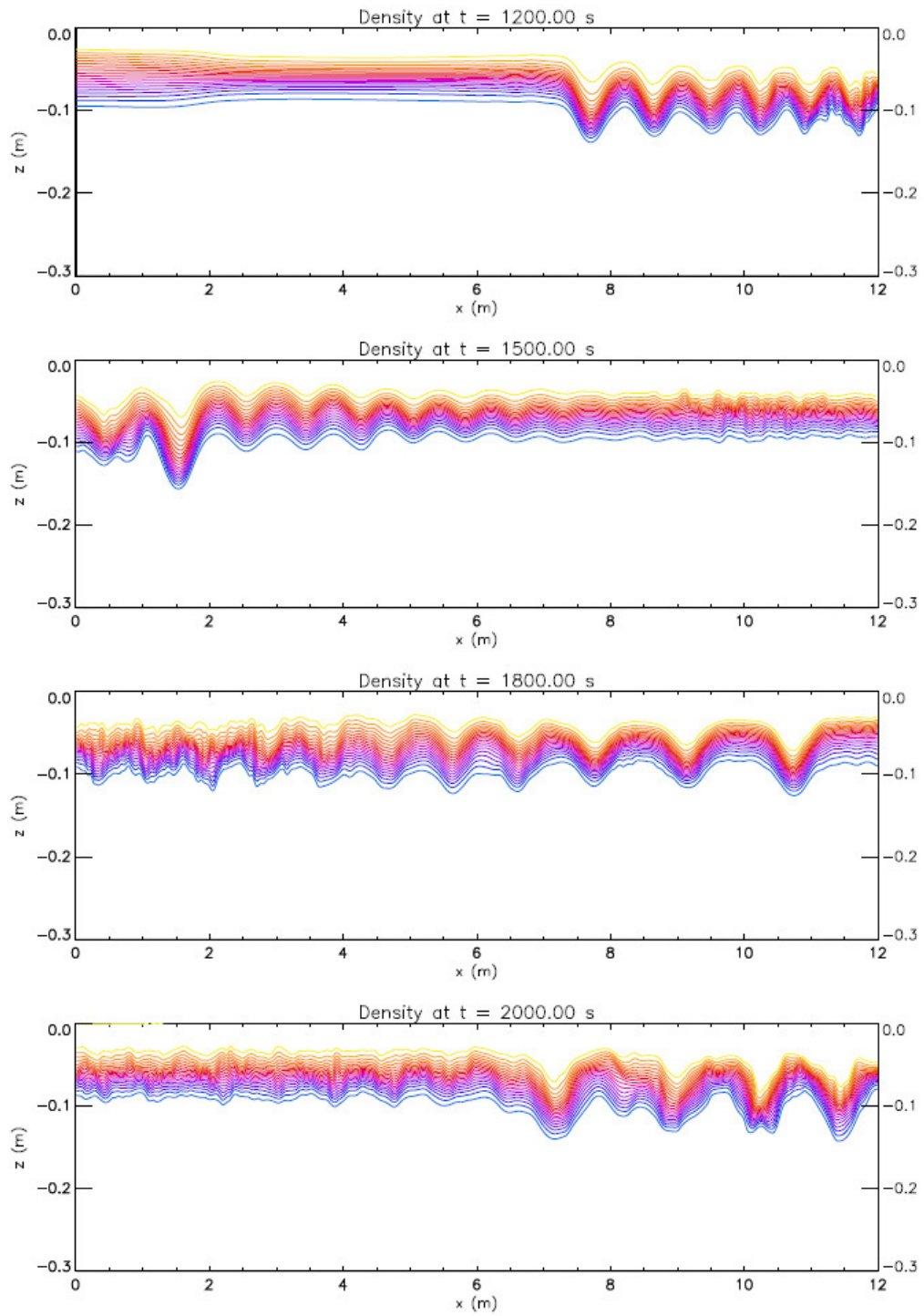
Figure 4.12: Temperature on x-z plane at $t = 1200$ s, 1500 s, 1800 s and 2000 s using the IGW model

49

4.3 Grid

The MITgcm uses the Arakawa C-grid and our grids are set up using a Cartesian co-ordinate system. In the horizontal plane, the Matlab command G=numgrid('D',nx) is used to generate the approximate circular lake (Fig. 4.13). In a C-grid, within the same horizontal plane, the external forcing F is applied at the grid cell corners, temperature T at the centre, zonal velocity u on sides $x = $ constant, and meridional velocity v on on sides $y = $ constant (Fig. 4.14). In the vertical plane, T, F, u, and v are initialized at the centre of the grid, while w is on the top and bottom sides, centred of horizontal. (Fig. 4.15).

nz = 276
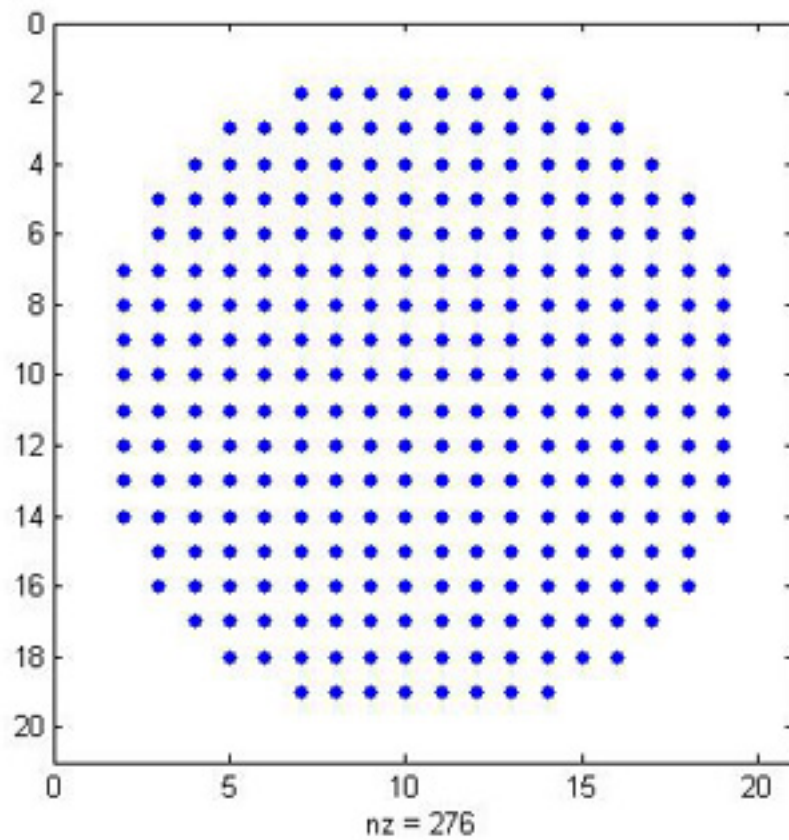
Figure 4.13: Horizontal grid setup

50
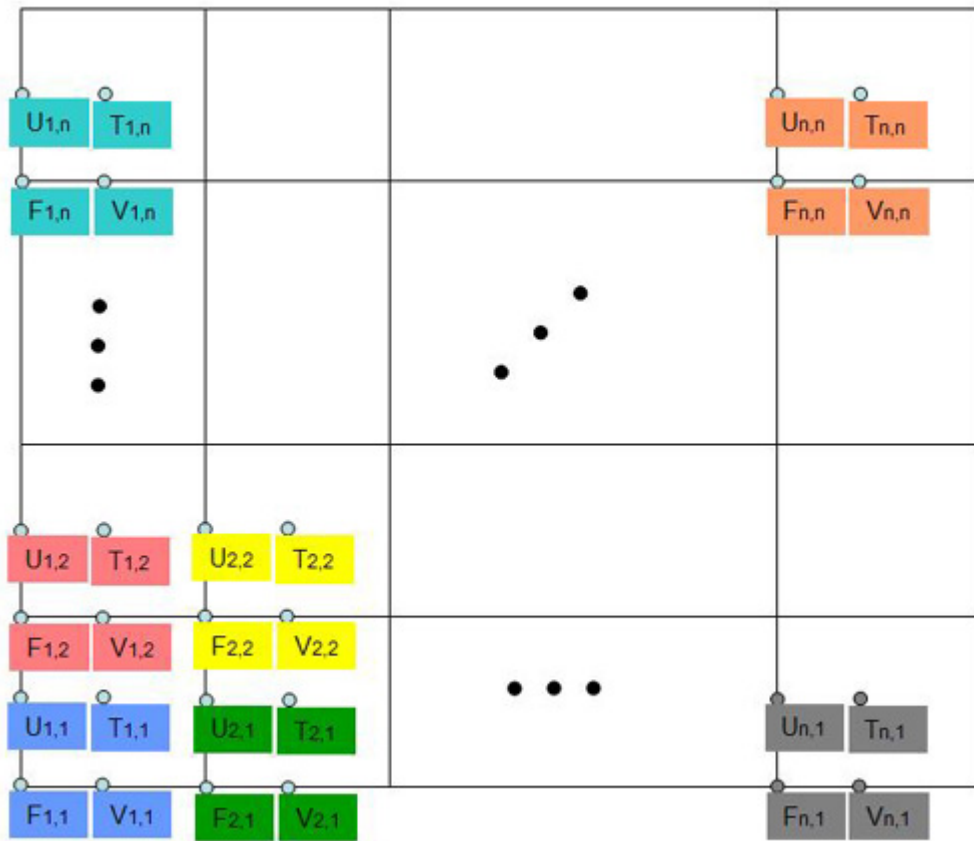
Figure 4.14: C-grid initialization in the horizontal plane
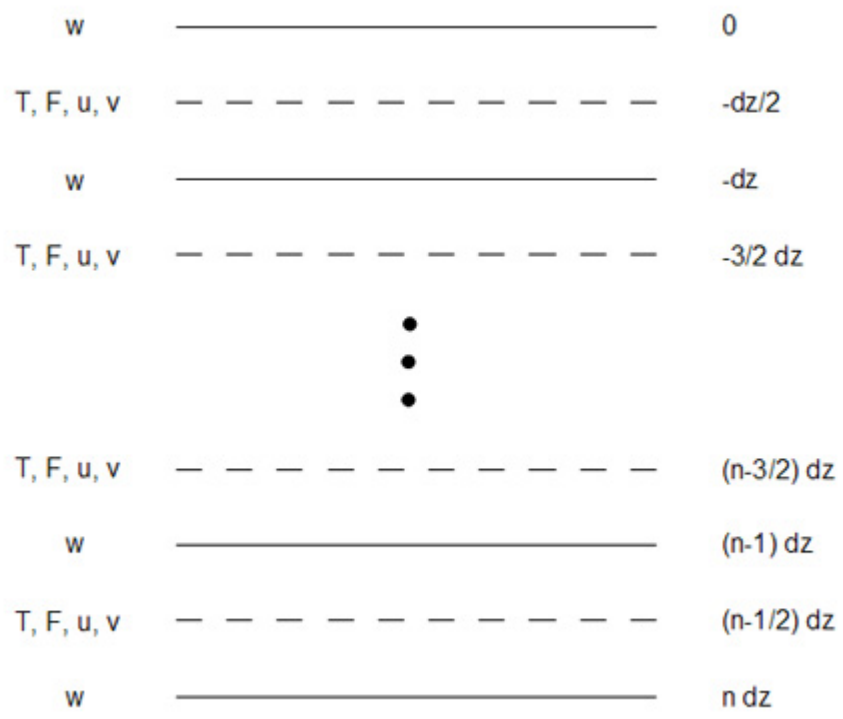
Figure 4.15: C-grid initialization in the vertical plane

4.4 Initialization in the MITgcm

Recall that the internal Rossby radius of deformation for a two-layer model R is defined by

$$R = \sqrt{g'h_1}/f, \tag{4.2}$$

where h_1 is the thickness of the upper layer, f is the Coriolis parameter, and g' is the reduced gravity which is defined by

$$g' = \frac{\rho_2 - \rho_1}{\rho_2}g, \tag{4.3}$$

where ρ_1 and ρ_2 are the density of top and bottom layer, and g is the gravitational acceleration. In the MITgcm, temperature is used instead of density and recall the linear equation of state,

$$\rho = \rho_0(1 - \alpha_T(T - T_0)). \tag{4.4}$$

Then $g' \approx -\alpha_T(T_2 - T_1)g$ if $\rho_2 \approx \rho_0$. Assuming we are interested a lake at mid-latitude with $f = 10^{-4}$ s^{-1}, $T_1 = 20\,°$C, $T_2 = 10\,°$C, and $h_1 = 15$ m. Then $R \approx 5.4$ km given that the thermal expansion coefficient is $2 \times 10^{-4}(°$C$)^{-1}$. Therefore, we choose a lake of radius 20 km in order to investigate the effect of Earth's rotation. In the MITgcm model, the initial vertical velocity w is not required since it is automatically calculated in the model given the horizontal velocities u and v. In addition to u and v, the initial distribution of the temperature T is required.

4.4.1 Case I: $C = -\alpha^2 < 0$

Recall $\hat{w}(r)$ for case I in Chapter 3,

$$\hat{w}(r) = AJ_n(\alpha r). \tag{4.5}$$

Substituting $\hat{w}(r)$ into the solutions we obtained $(3.46) - (3.55)$ and letting $t = 0$ we get the initial conditions,

$$w = \hat{w}(r)\sin(n\theta)\phi(z), \tag{4.6}$$
$$\rho = \hat{\rho}(r)\cos(n\theta)\phi(z)N^2(z), \tag{4.7}$$
$$p = \hat{p}(r)\cos(n\theta)\phi'(z), \tag{4.8}$$
$$u_r = \hat{u}_r(r)\sin(n\theta)\phi'(z), \tag{4.9}$$
$$u_\theta = \hat{u}_\theta(r)\cos(n\theta)\phi'(z), \tag{4.10}$$
$$T = \bar{T}(z) + T_p, \tag{4.11}$$
$$T_p = -\frac{\rho}{\alpha_T}, \tag{4.12}$$

where

$$\hat{w}(r) = A J_n(\alpha r), \tag{4.13}$$

$$\hat{\rho}(r) = \frac{A J_n(\alpha r)}{\omega g}, \tag{4.14}$$

$$\hat{p}(r) = A \frac{(\omega^2 - f^2)}{\omega \alpha^2} J_n(\alpha r), \tag{4.15}$$

$$\hat{u}_r(r) = \frac{A}{r \omega \alpha^2} \Big((\omega - f) n J_n(\alpha r) - \omega \alpha r J_{n+1}(\alpha r) \Big), \tag{4.16}$$

$$\hat{u}_\theta(r) = \frac{A}{r \omega \alpha^2} \Big((\omega - f) n J_n(\alpha r) + f \alpha r J_{n+1}(\alpha r) \Big). \tag{4.17}$$

In our simulation, a Cartesian coordinate system is used and the initial velocities needed by the model are u and v, so we need to transform u_r and u_θ into u and v. Using the simple relation,

$$u = u_r \cos \theta - u_\theta \sin \theta, \tag{4.18}$$

$$v = u_r \sin \theta + u_\theta \cos \theta. \tag{4.19}$$

we obtain the initial velocities u and v,

$$u = \Big[\hat{u}_r \sin(n\theta) \cos \theta - \hat{u}_\theta \cos(n\theta) \sin \theta \Big] \phi'(z), \tag{4.20}$$

$$v = \Big[\hat{u}_r \sin(n\theta) \sin \theta + \hat{u}_\theta \cos(n\theta) \cos \theta \Big] \phi'(z), \tag{4.21}$$

From (4.16) and (4.17), we notice that $\hat{u}_r$ and $\hat{u}_\theta$ contain the $1/r$ term which are not defined at $r = 0$. Now we are going to use the asymptotic behavior of the Bessel functions to define those values at $r = 0$. First we know that as $x \to 0$,

$$J_n(x) \sim \frac{1}{\Gamma(n+1)} \left(\frac{x}{2} \right)^n, \tag{4.22}$$

with $0 < x \le \sqrt{n+1}$. $\Gamma(n+1)$ is the Gamma function, and $\Gamma(n+1) = n!$ when n is an non-negative integer. Therefore, as $\alpha r \to 0$

$$J_0(\alpha r) \sim 1, \quad J_1(\alpha r) \sim \frac{1}{2} \alpha r, \quad J_2(\alpha r) \sim \frac{1}{2} \left(\frac{\alpha r}{2} \right)^2,$$

For $n = 1$ applying the asymptotic approximation yields

$$\hat{u}_r(0) = \frac{A}{2} \frac{\omega - f}{\omega \alpha}, \tag{4.23}$$

$$\hat{u}_\theta(0) = \frac{A}{2} \frac{\omega - f}{\omega \alpha}. \tag{4.24}$$

Substituting these into the u, v equation gives

$$u(r = 0) = 0,$$

$$v(r = 0) = \frac{A}{2} \frac{\omega - f}{\omega \alpha} \phi'(z). \tag{4.25}$$

54

At the origin u and v are independent of θ, which is the result we are looking for. The rest of the terms in the initial conditions do not contain the $1/r$ term, which means they are defined at $r = 0$, and the values are

$$w(r = 0) = 0, \quad \rho(r = 0) = 0, \quad p(r = 0) = 0, \quad T_p(r = 0) = 0. \tag{4.26}$$

Constant N

We use the following parameters for the constant N problem in case I in Table 4.2,

Table 4.2: Values of parameters for constant N for case I

H	depth of the lake	50 m
r_0	radius of the lake	20 km
T_s	temperature at the surface	20 °C
T_b	temperature at the bottom	10 °C
η	wave amplitude	2.5 m
α_T	coefficient of thermal expansion	$2 \times 10^{-4} (°C)^{-1}$
f	Coriolis parameter	10^{-4} rad $\cdot$ s^{-1}
N	buoyancy frequency	1.98×10^{-2} rad $\cdot$ s^{-1}
n	wave number in θ direction	1
m	wave number in z direction	$\pi/50$ m^{-1}
$nx \times ny \times nz$	resolution	$200 \times 200 \times 20$

The temperature is linearly distributed if N is a constant. Given $T_s = 20\,°C$ and $T_b = 10\,°C$, N can be easily calculated

$$N = \sqrt{g\alpha_T \frac{d\bar{T}(z)}{dz}} = 1.98 \times 10^{-2}(\text{rad} \cdot \text{s}^{-1}),$$

Recall that the solution of $\phi(z)$ for constant N is

$$\phi(z) = \sin(mz), \tag{4.27}$$

where $m = \alpha\sqrt{\frac{N^2-\omega^2}{\omega^2-f^2}}$. For a mode-one wave, $m = \pi/H$, and the eigenvalue problem (4.28) can be easily solved,

$$\frac{fn}{r_0}J_n(\alpha r_0) - \omega\alpha J_n'(\alpha r_0) = 0. \tag{4.28}$$

One pair of eigenvalues is $\omega = 1.29075 \times 10^{-4}$ s^{-1} and $\alpha = 2.58982 \times 10^{-4}$ m^{-1}. With all the values of parameters, we have the following plots for initial conditions (Fig. 4.16).
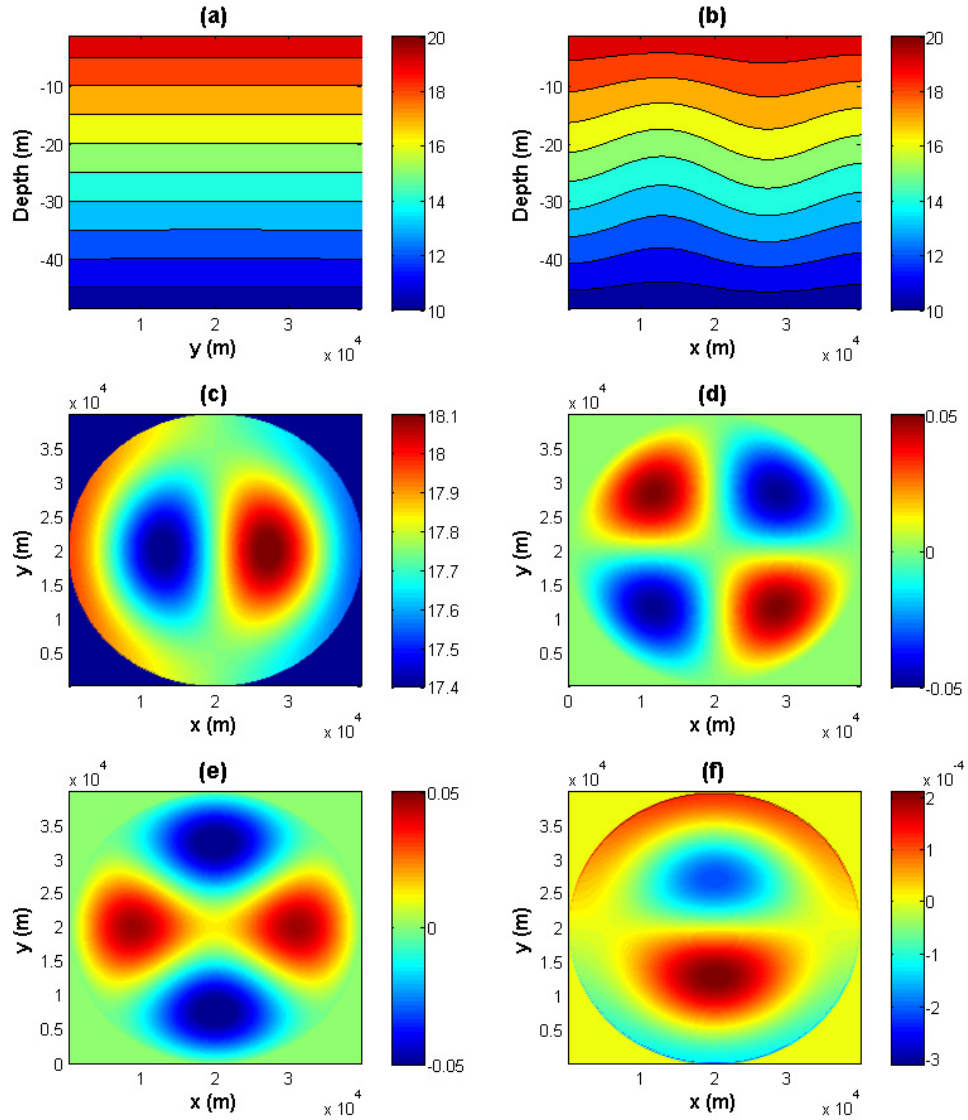
Figure 4.16: Initial profiles of T, u, and v in case I with a constant N. (a): T in $x = 20$ km cross-section (y-z plane); (b): T in $y = 20$ km cross-section (x-z plane); (c): T in $z = -11.25$ m cross-section (x-y plane); (d): u in $z = -11.25$ m cross-section (x-y plane); (e): v in $z = -11.25$ m cross-section (x-y plane); (f): w in $z = -10$ m (different depth than u and v due to use of C-grid) cross-section (x-y plane);

Non-constant $N(z)$

We use the following setup for the non-constant $N(z)$ problem in Table 4.3,

Table 4.3: Values of parameters for non-constant $N(z)$ for case I

H	depth of the lake	50 m
r_0	radius of the lake	20 km
T_s	temperature at the surface	20 °C
T_b	temperature at the bottom	10 °C
z_0	position of the thermocline at rest	−15 m
d	thickness of the thermocline	2 m
α_T	coefficient of thermal expansion	$2 \times 10^{-4} (°\mathrm{C})^{-1}$
η	wave amplitude	1.9 m
f	Coriolis parameter	10^{-4} rad $\cdot$ s^{-1}
n	wave number in θ direction	1
$nx \times ny \times nz$	resolution	$200 \times 200 \times 50$

First of all we need to solve the eigenvalue problem numerically. Recall that the eigenvalue problem is

$$\frac{fn}{r_0} J_n(\alpha r_0) - \omega \alpha J'_n(\alpha r_0) = 0, \tag{4.29}$$

$$\phi''(z) + \alpha^2 \frac{N^2(z) - \omega^2}{\omega^2 - f^2} \phi(z) = 0, \tag{4.30}$$

with boundary conditions $\phi(0) = \phi(-H) = 0$.

We begin with the two-layer limit analyzed in Section 3.4 to find an initial guess for the eigenvalues. Recall that ω and α can be only found when $\omega > f$ in case I. The system of equations (3.114) and (3.115), which is the approximate eigenvalue problem in the two-layer limit, can be easily solved numerically,

$$\frac{fn}{r_0} J_n(\alpha r_0) - \omega \alpha J'_n(\alpha r_0) = 0, \tag{4.31}$$

$$\frac{g'M}{\omega^2} \sinh(Mh_1) \sinh(Mh_2) - \sinh(MH) = 0, \tag{4.32}$$

where $M = \frac{\alpha \omega}{\sqrt{\omega^2 - f^2}}$ and $g' = g\alpha_T(T_s - T_b)$. Defining F_1 and F_2 as the left hand side of (4.31) and (4.32), zero contours plots of F_1 and F_2 are made using the given values of parameters (Fig. 4.17). The intersections give the solution of the system. In case I constant N, the initialization plots suggest that $\alpha = 2.5 \times 10^{-4}$ m^{-1} is a good value for a better view of horizontal structures. Hence, we choose the zero near $\alpha = 2.5 \times 10^{-4}$ m^{-1} and $\omega = 1.6 \times 10^{-4}$ s^{-1}.

Given the initial guessing eigenvalues, we choose an interval of ω and α containing the initial guess and plot the zero contours of the left hand side of (4.29),
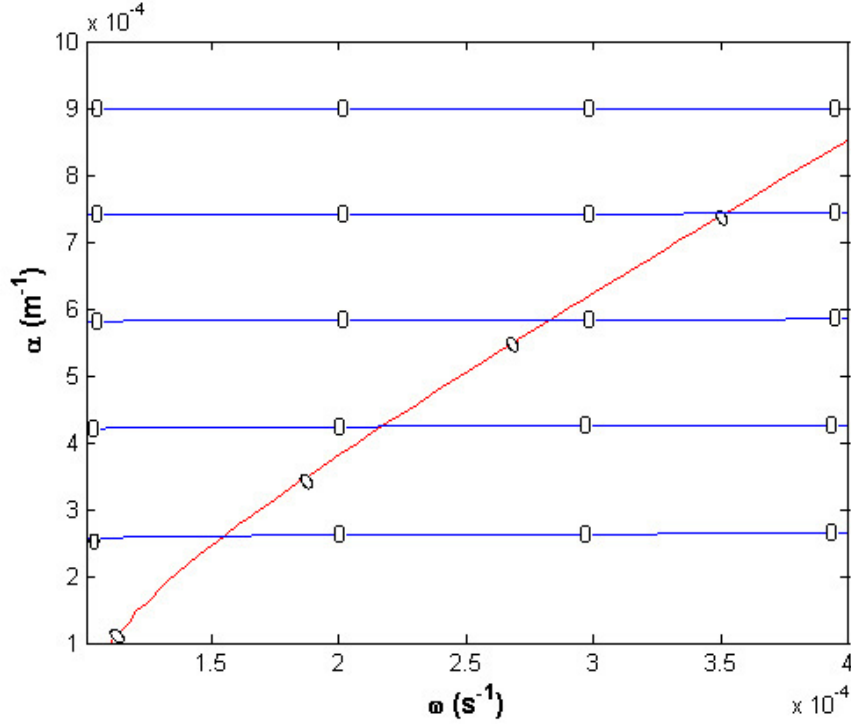
Figure 4.17: Zero contours plots in case I two-layer model. Zero contours of function F_1 is in blue, while the ones for F_2 is in red.

say G. For the ODE, we solve for $\phi(z)$ given ω and α and the boundary condition $\phi(0) = 0$, then plot the zero contours of $\phi(-H)$. The intersections of two contours give the eigenvalues. Fig.4.18 shows the zero contours for ω from $1.01 \times 10^{-4}\text{s}^{-1}$ to $4 \times 10^{-4}\text{s}^{-1}$ and α from 1×10^{-4} m^{-1} to 9×10^{-4} m^{-1}. By refining the ω and α intervals one pair of mode-one eigenvalue is obtained, $\omega = 1.50459 \times 10^{-4}$ s^{-1} and $\alpha = 2.60062 \times 10^{-4}$ m^{-1}.

Given all the parameters, we have the initializations as follows, see Fig. 4.19 and Fig. 4.20. The initial profiles have similar structures as in the constant N case. However, there are some problems in the initialization. First, in Fig. 4.19 (b), there are two circles representing points at which the density field is statically unstable. Moreover, we know the horizontal velocities over and under a traveling wave are opposite in direction. In the $y = 20$ km cross-section (Fig. 4.20), there is no sign of this phenomena since the wave is flattened by linearization. For small amplitude waves, this is acceptable, however, when we study the nonlinearity of large amplitude waves the exact structure has to be presented. In order to solve these problems, we introduce a Lagrangian formulation in next section.
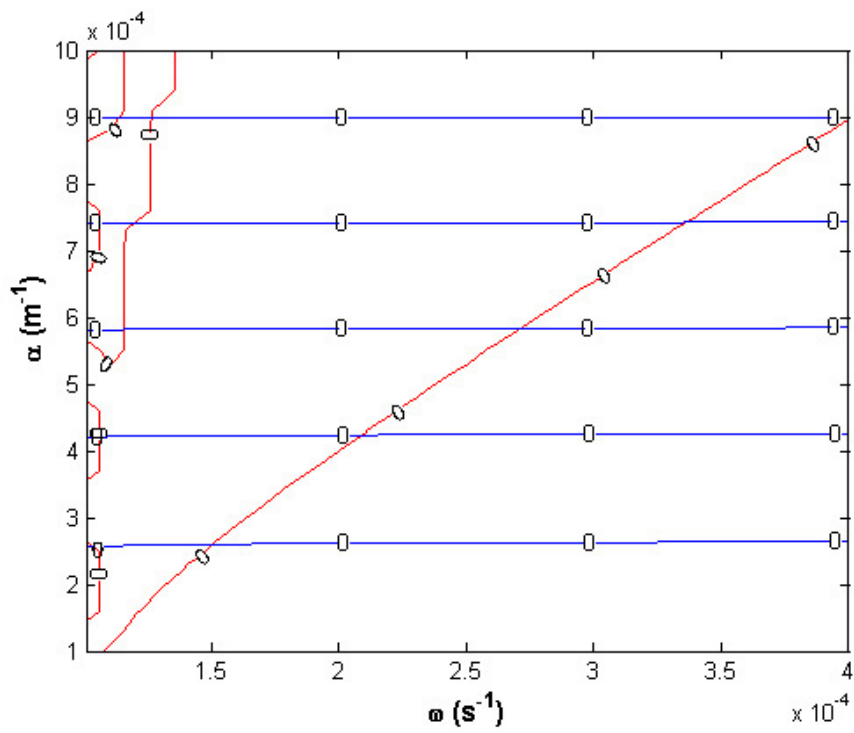
Figure 4.18: Zero contours for G in blue and $\phi(-H)$ in red for case I.

Figure 4.19: Initial temperature profile in case I with non-constant $N(z)$ (Eulerian formulation). (a): T in $x = 20$ km cross-section (y-z plane); (b): T in $y = 20$ km cross-section (x-z plane); (c): T in $z = -11.25$ m cross-section (x-y plane).

Figure 4.20: Initial horizontal velocities profiles in case I with non-constant $N(z)$ (Eulerian formulation). (a): u in $z = -11.25$ m cross-section (x-y plane); (b): v in $z = -11.25$ m cross-section (x-y plane); (c): v in $x = 20$ km cross-section (y-z plane); (d): v in $y = 20$ km cross-section (x-z plane); (u is zero at $x = 20$ km and $y = 20$ km cross-section)

4.4.2 Lagrangian Formulation

In the previous section, we encountered two problems: one is that the density profile has regions of static instability, and the other is incorrect velocities distributions over and under the traveling waves. In this section, we use a Lagrangian formulation to generate the initial profiles, which helps us to solve these problems.

Define z^* so that the density profile can be expressed as $\rho = \bar{\rho}(z^*)$, where $\bar{\rho}$ is the background density function. In the z^* plane, $z = z^* + \eta$ where η is the amplitude of the wave. Given the expression of w from (4.6), η is obtained by integration

$$\eta = \int w \, dt = \frac{A}{\omega} J_n(\alpha r) \cos(n\theta - \omega t) \phi(z^*). \tag{4.33}$$

z^* can be solved numerically using the following expression,

$$z = z^* + \frac{A}{\omega} J_n(\alpha r) \cos(n\theta - \omega t) \phi(z^*). \tag{4.34}$$

Then in the Lagrangian formulation the velocities u_r and u_θ are

$$u_r = \hat{u}_r \sin(n\theta - \omega t) \frac{d\phi(z^*)}{dz^*} \tag{4.35}$$

$$= \hat{u}_r \sin(n\theta - \omega t) \frac{d\phi(z^*)}{dz} \left(1 + \frac{A}{\omega} J_n(\alpha r) \cos(n\theta) \frac{d\phi(z^*)}{dz} \right), \tag{4.36}$$

$$u_\theta = \hat{u}_\theta \cos(n\theta - \omega t) \frac{d\phi(z^*)}{dz} \left(1 + \frac{A}{\omega} J_n(\alpha r) \cos(n\theta) \frac{d\phi(z^*)}{dz} \right). \tag{4.37}$$

Using the same parameters as the Euler formulation in Table 4.3 and the same pair of eigenvalues $\omega = 1.50459 \times 10^{-4} \text{s}^{-1}$ and $\alpha = 2.60062 \times 10^{-4}$ m^{-1}, the initialization using the Lagrangian formulation is shown in Fig. 4.21 and Fig. 4.22. The temperature profile in Fig. 4.21 no longer have overshoots. In Fig. 4.22, we see the velocity profiles are initialized along the thermocline.
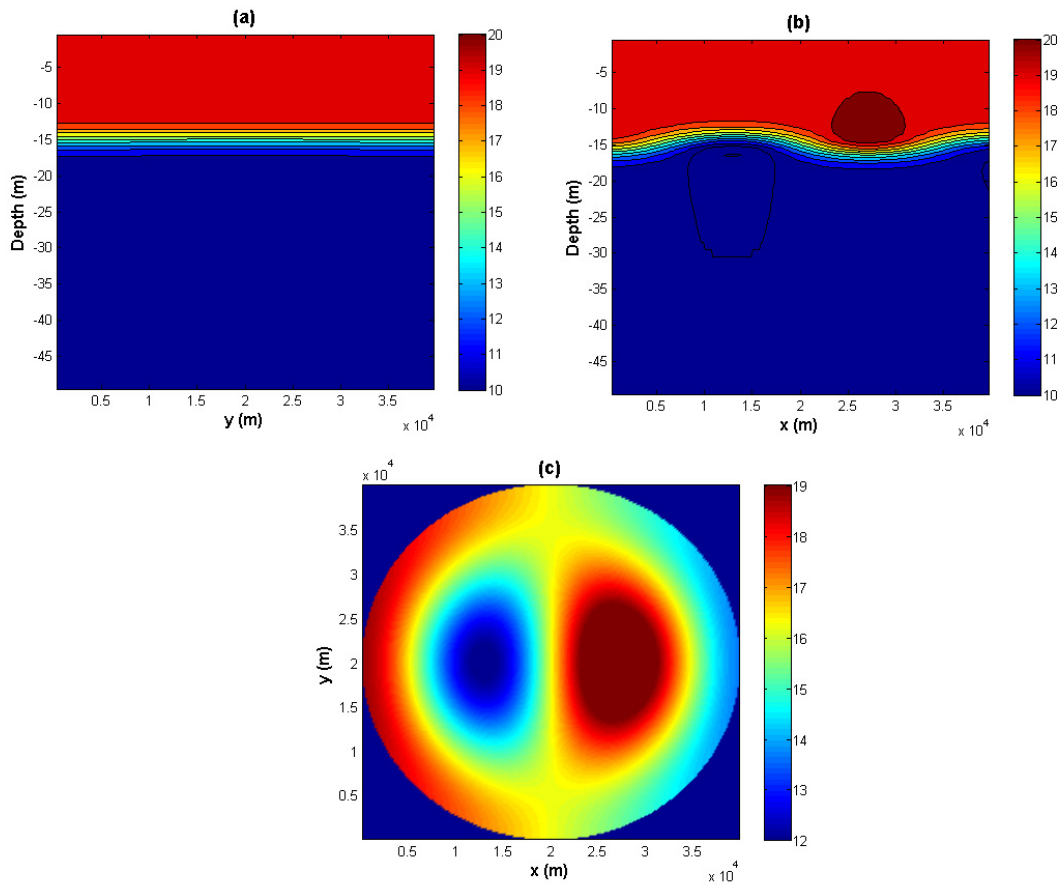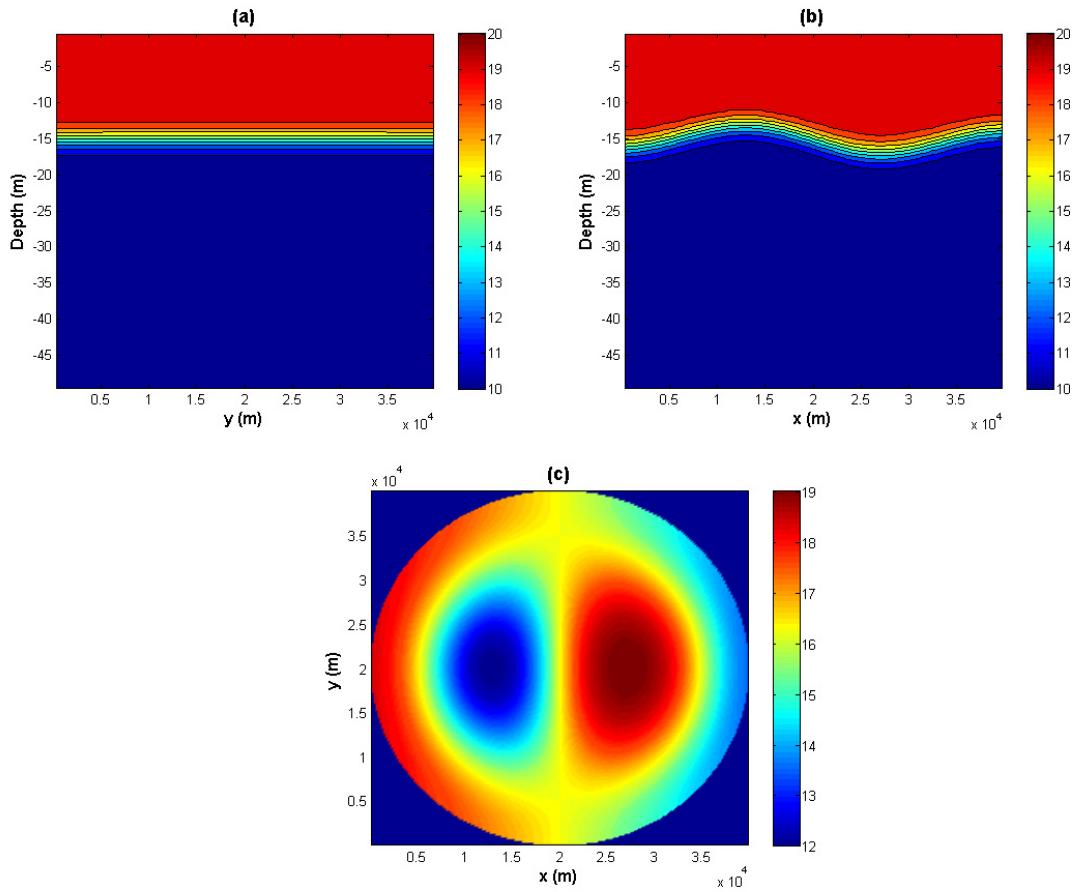
Figure 4.21: Initial temperature profile in case I with non-constant $N(z)$ (Lagrangian formulation). (a): T in $x = 20$ km cross-section (y-z plane); (b): T in $y = 20$ km cross-section (x-z plane); (c): T in $z = -11.25$ m cross-section (x-y plane).

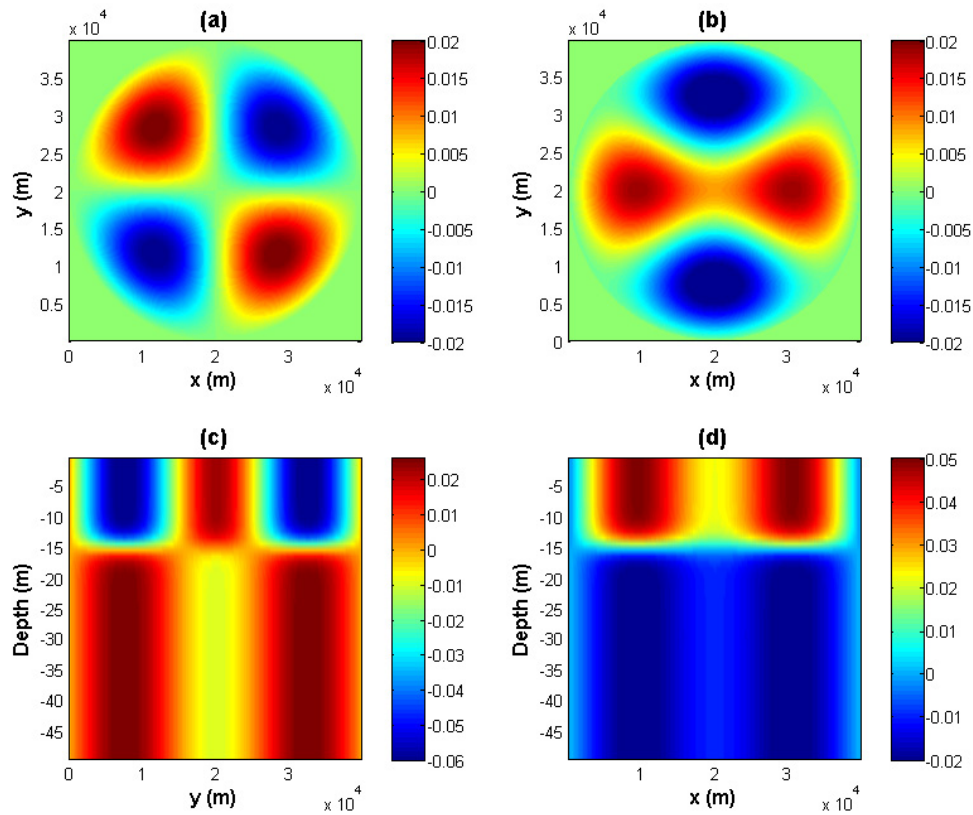Figure 4.22: Initial horizontal velocities profiles in case I with non-constant $N(z)$ (Lagrangian formulation). (a): u in $z = -11.25$ m cross-section (x-y plane); (b): v in $z = -11.25$ m cross-section (x-y plane); (c): v in $x = 20$ km cross-section (y-z plane); (d): v in $y = 20$ km cross-section (x-z plane); (u is zero at $x = 20$ km and $y = 20$ km cross-section)

4.4.3 Case II: $C = \beta^2 > 0$

Similar to case I, we have the initial conditions as follows,

$$w = \hat{w}(r)\sin(n\theta)\phi(z), \tag{4.38}$$

$$p = \hat{p}(r)\cos(n\theta)\phi'(z), \tag{4.39}$$

$$u_r = \hat{u}_r(r)\sin(n\theta)\phi'(z), \tag{4.40}$$

$$u_\theta = \hat{u}_\theta(r)\cos(n\theta)\phi'(z), \tag{4.41}$$

$$\rho = \hat{\rho}(r)\cos(n\theta)N^2(z)\phi(z), \tag{4.42}$$

$$T = \bar{T}(z) + T_p, \tag{4.43}$$

$$T_p = -\frac{\rho}{\alpha_T}, \tag{4.44}$$

$$\tag{4.45}$$

where

$$\hat{w}(r) = BI_n(\beta r), \tag{4.46}$$

$$\hat{\rho}(r) = \frac{BI_n(\beta r)}{\omega g}, \tag{4.47}$$

$$\hat{p}(r) = -B\frac{(\omega^2 - f^2)}{\omega\beta^2}I_n(\beta r), \tag{4.48}$$

$$\hat{u}_r(r) = \frac{B}{r\omega\beta^2}\Big((f - \omega)nI_n(\beta r) - \omega\beta r I_{n+1}(\beta r)\Big), \tag{4.49}$$

$$\hat{u}_\theta(r) = \frac{B}{r\omega\beta^2}\Big((f - \omega)nI_n(\beta r) + f\beta r I_{n+1}(\beta r)\Big). \tag{4.50}$$

Again asymptotic analysis is used to define the value of u_r and u_θ at the origin $r = 0$. As $x \to 0$,

$$I_n(x) = \frac{1}{\Gamma(n+1)}\left(\frac{x}{2}\right)^n, \tag{4.51}$$

with $0 < x \le \sqrt{n+1}$. For $n = 1$, the asymptotic approximation gives,

$$\hat{u}_r(0) = \frac{B}{2}\frac{f - \omega}{\omega\beta}, \tag{4.52}$$

and

$$\hat{u}_\theta(0) \sim \frac{B}{2}\frac{f - \omega}{\omega\beta}. \tag{4.53}$$

Substituting se into u and v gives,

$$u(r = 0) = 0,$$

$$v(r = 0) = \frac{B}{2}\frac{f - \omega}{\omega\beta}\phi'(z). \tag{4.54}$$

The rest of terms in the initial conditions do not contain the $1/r$ term, which means they are defined at $r = 0$, and the values are

$$w(r = 0) = 0, \rho(r = 0) = 0, p(r = 0) = 0, T_p(r = 0) = 0. \tag{4.55}$$

Constant N

For the constant N problem in case II, the parameters are shown in Table 4.4.

Table 4.4: Values of setup parameters for constant N in case II

H	depth of the lake	50 m
r_0	radius of the lake	20 km
T_s	temperature at the surface	$20\,°C$
T_b	temperature at the bottom	$10\,°C$
η	wave amplitude	2 m
α_T	coefficient of thermal expansion	$2 \times 10^{-4}(°C)^{-1}$
f	Coriolis parameter	10^{-4} rad $\cdot$ s^{-1}
N	buoyancy frequency	1.98×10^{-2} rad $\cdot$ s^{-1}
n	wave number in θ direction	1
m	wave number in z direction	$\pi/50$ m^{-1}
$nx \times ny \times nz$	resolution	$200 \times 200 \times 20$

One pair of eigenvalue are easily to obtain using Maple as before, $\omega = 1.716748 \times 10^{-5}$ s^{-1} and $\alpha = 3.126215 \times 10^{-4}$ m^{-1}. Fig. 4.23 shows the initial profiles of T, u, v, and w.
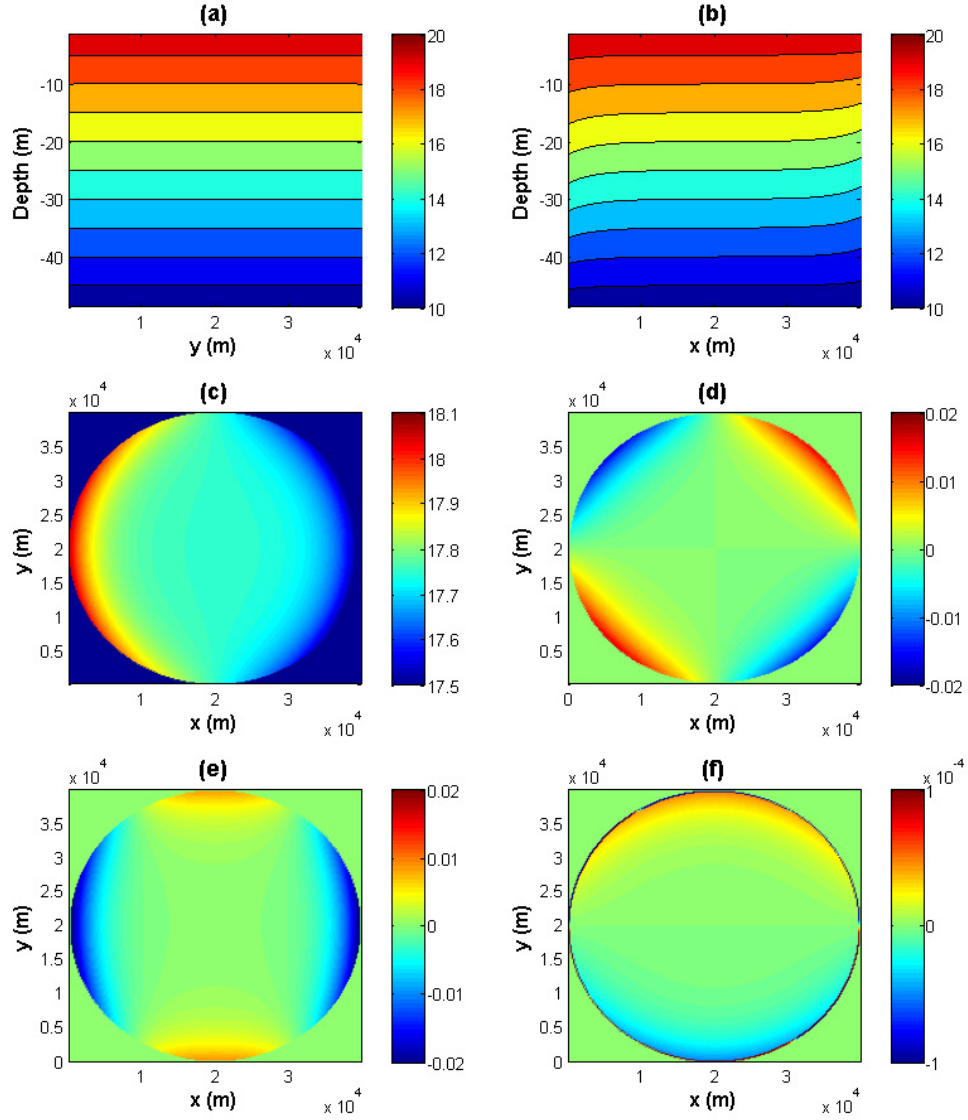
Figure 4.23: Initial profiles of $T, u,$ and v in case II with constant N. (a): T in $x = 20$ km cross-section (y-z plane); (b): T in $y = 20$ km cross-section (x-z plane); (c): T in $z = -11.25$ m cross-section (x-y plane); (d): u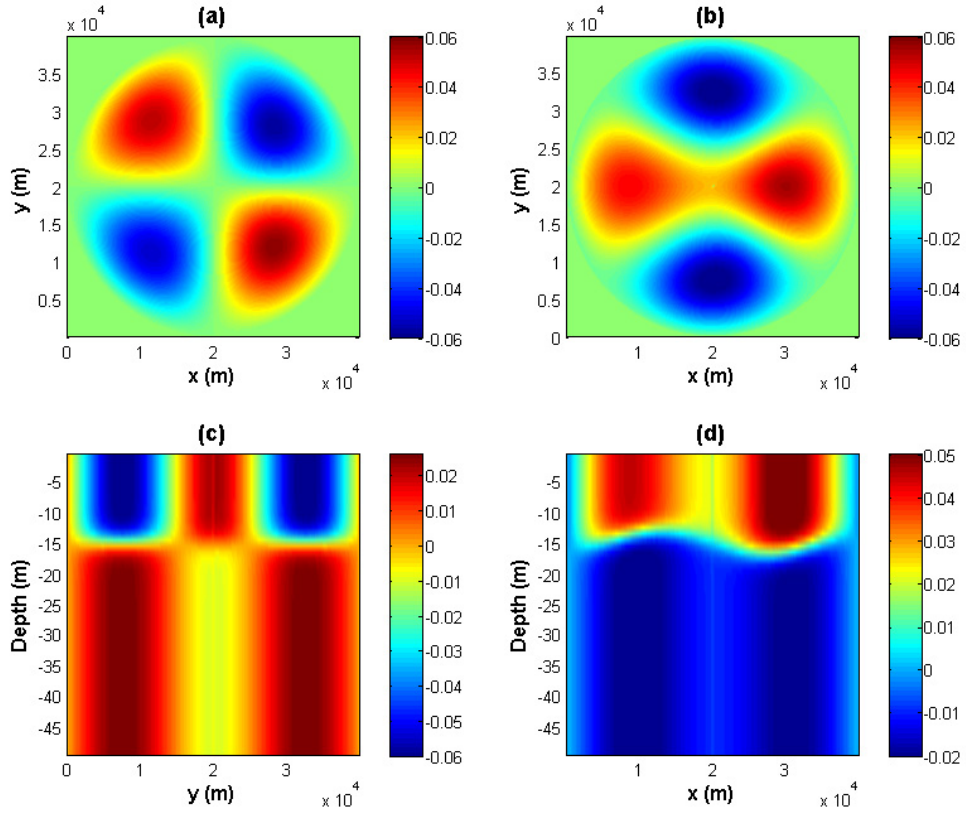 in $z = -11.25$ m cross-section (x-y plane); (e): v in $z = -11.25$ m cross-section (x-y plane); (f): w in $z = -10$ m cross-section (x-y plane);

Non-constant $N(z)$

For non-constant $N(z)$ problem in case II, the parameters are in Table 4.5.

Table 4.5: Values of setup parameters for non-constant $N(z)$ in case II

H	depth of the lake	50 m
r_0	radius of the lake	20 km
T_s	temperature at the surface	20 °C
T_b	temperature at the bottom	10 °C
z_0	position of the thermocline at rest	-15 m
d	thickness of the thermocline	2 m
α_T	coefficient of thermal expansion	$2 \times 10^{-4} (°C)^{-1}$
η	wave amplitude	5.5 m
f	Coriolis parameter	10^{-4} rad $\cdot$ s^{-1}
n	wave number in θ direction	1
$nx \times ny \times nz$	resolution	$200 \times 200 \times 50$

Again, we begin with the eigenvalue problem,

$$\frac{fn}{r_0} I_n(\beta r_0) - \omega \beta I_n'(\beta r_0) = 0, \tag{4.56}$$

$$\phi''(z) - \beta^2 \frac{N^2(z) - \omega^2}{\omega^2 - f^2} \phi(z) = 0, \tag{4.57}$$

with $\phi(0) = \phi(-H) = 0$. We begin with the two-layer limit analyzed in Section 3.4 to find an initial guess for the solution. Recall that the eigenvalues ω and β can only be found when $\omega < f$ in case II. The system of equations (3.127) and (3.128) can be easily solved numerically,

$$\frac{fn}{r_0} I_n(\beta r_0) - \omega \beta I_n'(\beta r_0) = 0, \tag{4.58}$$

$$\frac{g'\tilde{\gamma}}{\omega^2} \sinh(\tilde{\gamma} h_1) \sinh(\tilde{\gamma} h_2) - \sinh(\tilde{\gamma} H) = 0, \tag{4.59}$$

where $\tilde{\gamma} = \frac{\beta\omega}{\sqrt{f^2 - \omega^2}}$ and $g' = g\alpha_T(T_s - T_b)$. As before, defining $\tilde{F}_1$ and $\tilde{F}_2$ as the left hand side of (4.58) and (4.59), zero contour plots are made using the chosen parameters values (Fig. 4.24).

Given the initial guesses, the eigenvalues are obtained numerically. Defining $\tilde{G}$ as the left hand side of (4.56), Fig. 4.25 shows zero contours plots of $\tilde{G}$ and $\phi(-H)$ and the intersections are the eigenvalues. One pair of eigenvalues are $\omega = 2.43961 \times 10^{-5}$s^{-1} and $\beta = 2.24343 \times 10^{-4}$ m^{-1}. Given all the parameters, the initializations in Lagrangian formulation are presented in Fig. 4.26 and Fig. 4.27. Fig. 4.26 shows that the waves are trapped at the boundaries, which are Kelvin waves. In Fig. 4.27 (d), the velocities are initialized along the thermocline, which is what we expect when the Lagrangian formulation is used.
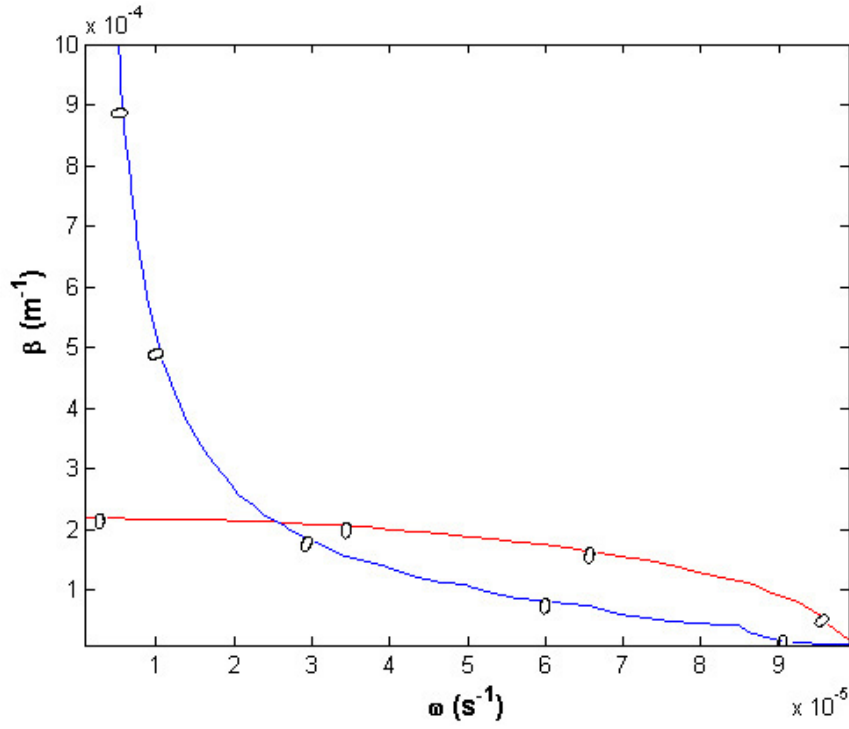
Figure 4.24: Zero contour plots in case II two-layer model. Zero contours of function $\tilde{F}_1$ is in blue, while the ones for $\tilde{F}_2$ is in red.
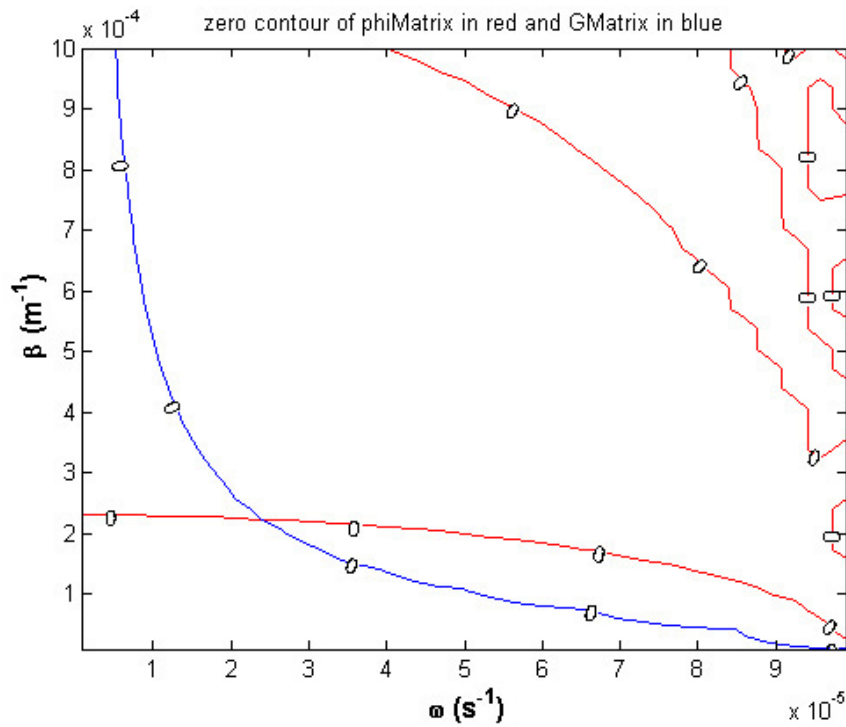
Figure 4.25: Zero contours for $\tilde{G}$ in blue and $\phi(-H)$ in red in case II.

69
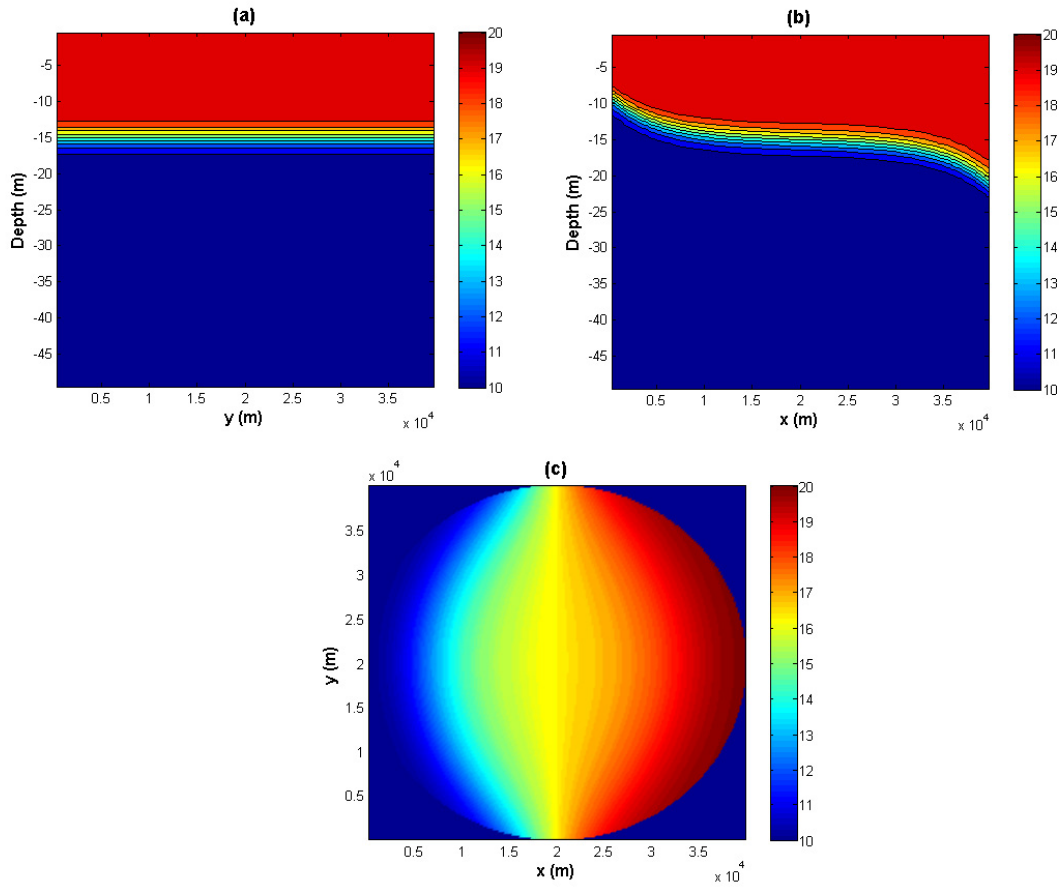
Figure 4.26: Initial temperature profile in case II with non-constant $N(z)$ (Lagrangian formulation). (a): T in $x = 20$ km cross-section (y-z plane); (b): T in $y = 20$ km cross-section (x-z plane); (c): T in $z = -11.25$ m cross-section (x-y plane).
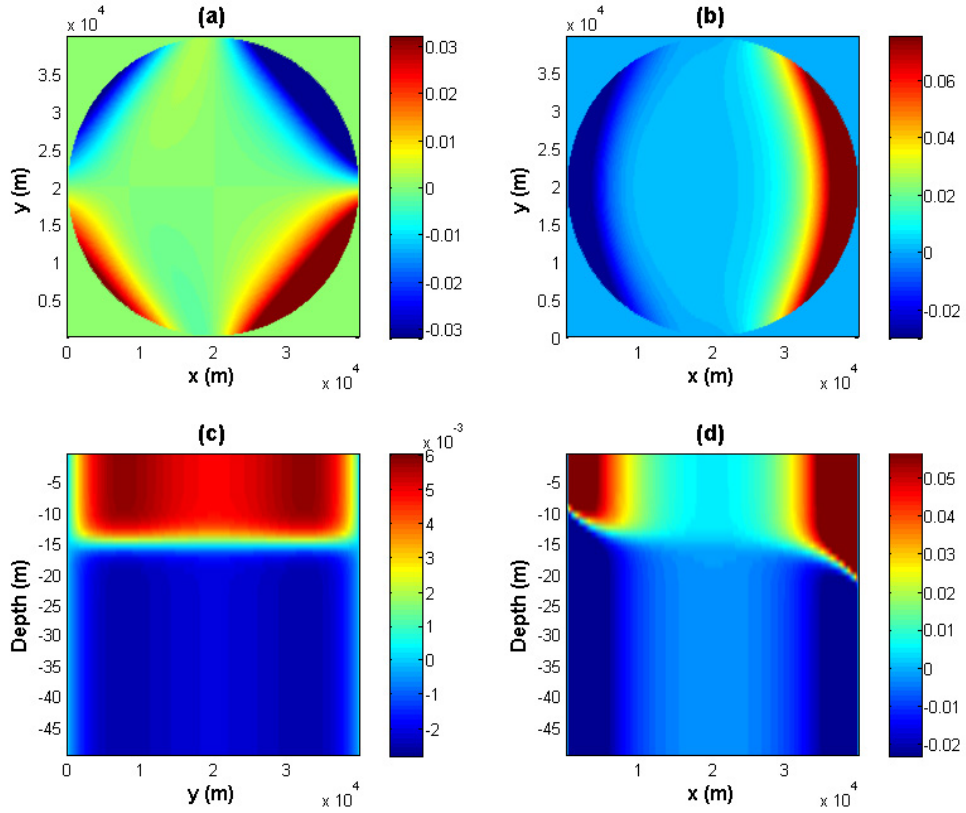
Figure 4.27: Initial horizontal velocities profiles in case II with non-constant $N(z)$ (Lagrangian formulation). (a): u in $z = -11.25$ m cross-section (x-y plane); (b): v in $z = -11.25$ m cross-section (x-y plane); (c): v in $x = 20$ km cross-section (y-z plane); (d): v in $y = 20$ km cross-section (x-z plane); (u is zero at $x = 20$ km and $y = 20$ km cross-section)

Chapter 5

Results

In this chapter, the results of the numerical simulations using the MITgcm are presented. Appendix A gives brief instructions about how to run the MITgcm. The analytical solution for the linear system is verified for Poincaré waves and Kelvin waves with the buoyancy frequency N either a constant or dependent on z. The result of Poincaré waves simulations is what we expected. However, in the Kelvin wave case, small waves are generated at the boundary and observed to propagate in the radial direction. When the horizontal resolution is increased, both the amplitude and wavelength of these small waves decrease. As the wave amplitude increases the waves become more nonlinear. Poincaré waves steepen and generate solitary-like waves with shorter wavelengths, but most of the energy contained in these waves is transferred back and forth between the parent wave and the solitary-like waves. Kelvin waves, on the other hand, steepen and lose their energy to solitary-like waves. This conclusion agrees with de la Fuente et al. (2008).

We used one of the high performance machines in the Fluids group (winisk) as well as SHARCNET (Shared Hierarchical Academic Research Computing Network) to run the MITgcm model. "Winisk" is an Altix 350 with 16 Itanium2 processors and 96 GB of memory which was upgraded to 32 CPUs and 192 GB of memory recently. In SHARCNET, we used the machine "whale" because of the large number of processors. It has 768 nodes with 4 Opteron processors and 4 GB of memory in each node, but the interconnection among each node is gigabit ethernet which is quite slow. "Whale" is powerful and fast enough for most simulations we did in this thesis. However, in the Kelvin wave case with $800 \times 800 \times 50$ resolution and 0.5 s time step, it takes a extremely long time to finish using 16 CPUs. When we increase the number of CPUs to 64 the time needed is not shortened significantly, because of the slow interconnection speed. Another SHARCNET machine "requin" uses a faster interconnection method quadrics elan4, so our future high resolution work is scheduled to run on "requin" instead of "whale".

5.1 Case I: $C = -\alpha^2 < 0$

In the MITgcm model we could not find a way to linearize the density equation, so the model does not solve the exact linear equations. For now we name the system with the linear momentum equations and the nonlinear density equation "quasi-linear". However, it approximates to a linear problem when the wave amplitude is small.

To begin with, the analytical solution of the linear system is verified for a case with a constant N. Then two cases with a non-constant $N(z)$ are considered. When the model is set to be "quasi-linear", the linear solution is verified. When the nonlinear advection terms in the horizontal momentum equations are turned on, the system becomes fully nonlinear, in which the nonlinear effects are investigated using different setups for waves with larger amplitudes.

5.1.1 Constant N

Recall that section 4.4.1 gives the initial condition for the temperature T and the horizontal velocities u and v. In this run, we use the setup parameters in Table 5.1.

Table 5.1: Setup parameters for case I with a constant N

$nx \times ny \times nz$	grid points in x, y, z direction	200×200×20
Δt	time step	10 s
V_h, V_z	horizontal and vertical viscosity	0 m^2/s
D_h, D_z	horizontal and vertical diffusivity	0 m^2/s
	free surface or rigid lid?	rigid lid
$\mathbf{u} \cdot \vec{\nabla} \mathbf{u}$	momentum advection included?	no
	temperature advection scheme	33
ω	wave frequency	1.29075×10^{-4} s^{-1}
T_{period}	wave period	13.5 hours
η_0	wave amplitude	2.5 m

We use "winisk" with one processor to run this simulation. It approximately takes six hours to finish a two days simulation. First we look at the temperature at each cross-section. At $z = -11.25$ m (Fig. 5.1), from $t = 0$ to $t = 2$ hrs to $t = 4$ hrs, the initial temperature profile rotates counterclockwise without changing its shape. After 27 hrs, which is approximately 2 periods, the structure is nearly identical to the initial state (compare Fig. 5.1(d) and Fig. 5.1(a)). At $x = 20$ km (Fig. 5.2) and $y = 20$ km (Fig. 5.3) cross-sections, the waves move up and down periodically. Observing the waves in the x and y cross-sections is not the best way to follow the rotating waves, so we pick a circular vertical cross-section around the lake centered at the lake centre $(L/2, L/2)$ with a radius of $0.9r_0$, where r_0 is the

radius of the lake and L is the length of the square domain which is the diameter of the lake. (shown in Fig. 5.1(a) as the red circle), and θ is set to be zero on the interval $x \in [L/2, L]$ and increases counterclockwise. Then we flatten this hollow cylinder on a plane and plot the extracted data with respect to θ and z. In Fig. 5.4 the waves are clearly propagating around the lake without changing the shape with an approximately 13.5 hour period. Besides the temperature, we now discuss the velocities. Fig. 5.5, 5.6, and 5.7 show that the velocities u, v, and w rotate around the lake without changing their shapes and the period is approximately 13.5 hours. Therefore, we can conclude that they are indeed solutions for constant N case I with "quasi-linear" setups.

Figure 5.1: T at $z = -11.25$ m (5th layer) for case I with a constant N at different times: (a) $t = 0$, (b) $t = 2$ hrs, (c) $t = 4$ hrs, and (d) $t = 27$ hrs (approximately 2 periods). The red circle in (a) indicates the circular vertical cross-section picked in Fig. 5.4, $r = 0.9r_0$.

Figure 5.2: T at $x = 20$ km for case I with a constant N at different times: (a) $t = 0$, (b) $t = 2$ hrs, (c) $t = 4$ hrs, and (d) $t = 27$ hrs (approximately 2 periods).

Figure 5.3: T at $y = 20$ km for case I with a constant N at different times: (a) $t = 0$, (b) $t = 2$ hrs, (c) $t = 4$ hrs, and (d) $t = 27$ hrs (approximately 2 periods).
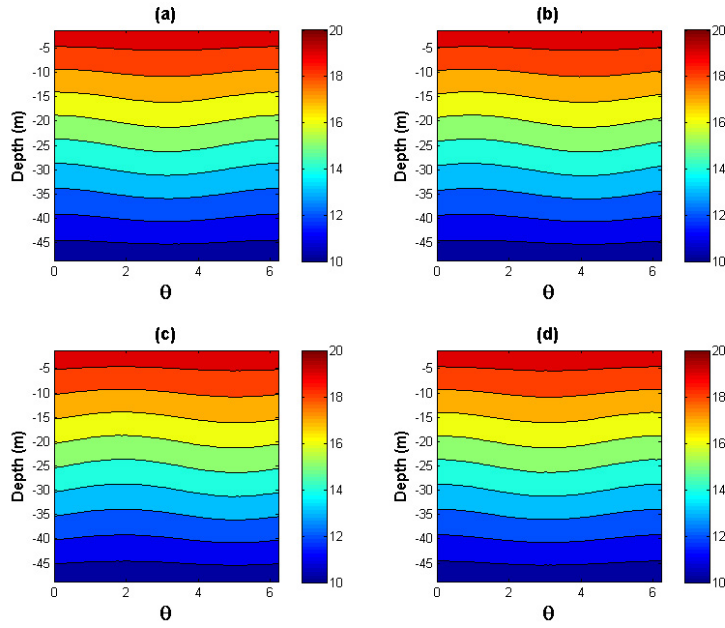
Figure 5.4: T at a circular vertical cross-section (radius $0.9r_0 = 18$ km) for case I with a constant N at different times: (a) $t = 0$, (b) $t = 2$ hrs, (c) $t = 4$ hrs, and (d) $t = 27$ hrs (approximately 2 periods).
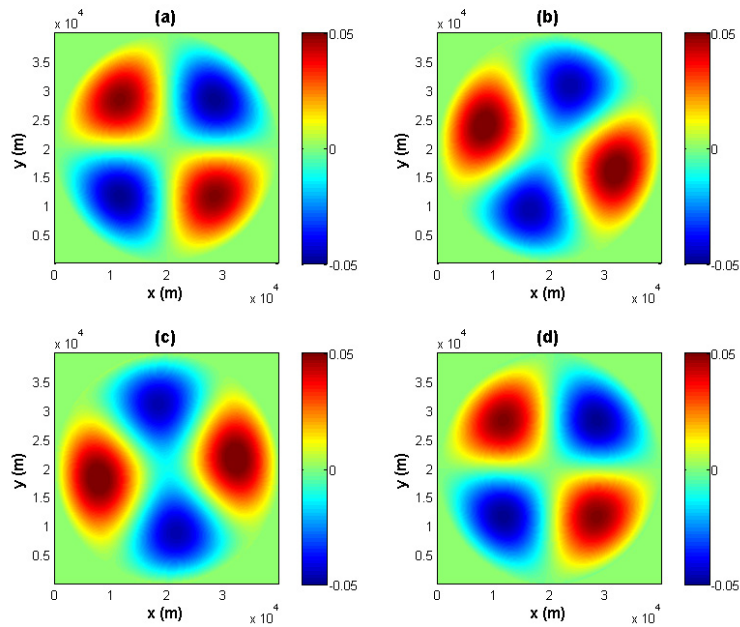
Figure 5.5: u at $z = -11.25$ m (5th layer) for case I with a constant N at different times: (a) $t = 0$, (b) $t = 2$ hrs, (c) $t = 4$ hrs, and (d) $t = 27$ hrs (approximately 2 periods).
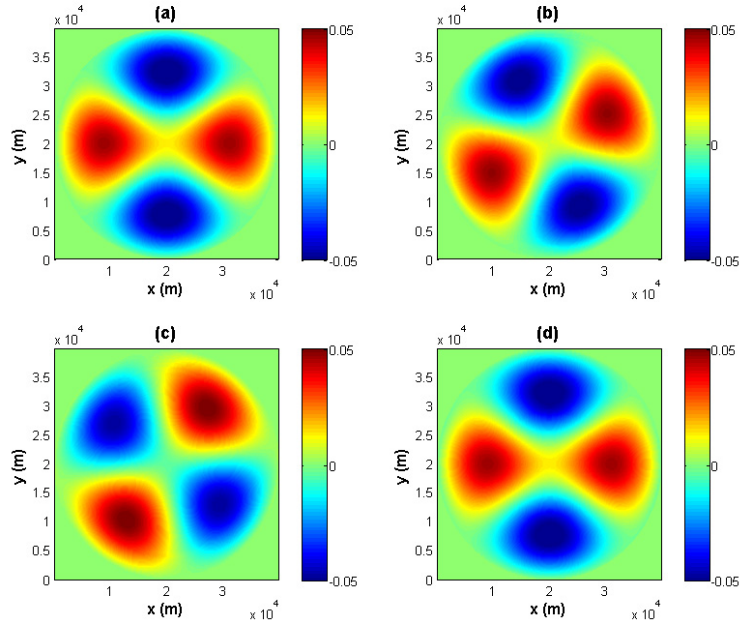
Figure 5.6: v at $z = -11.25$ m (5th layer) for case I with a constant N at different times: (a) $t = 0$, (b) $t = 2$ hrs, (c) $t = 4$ hrs, and (d) $t = 27$ hrs (approximately 2 periods).
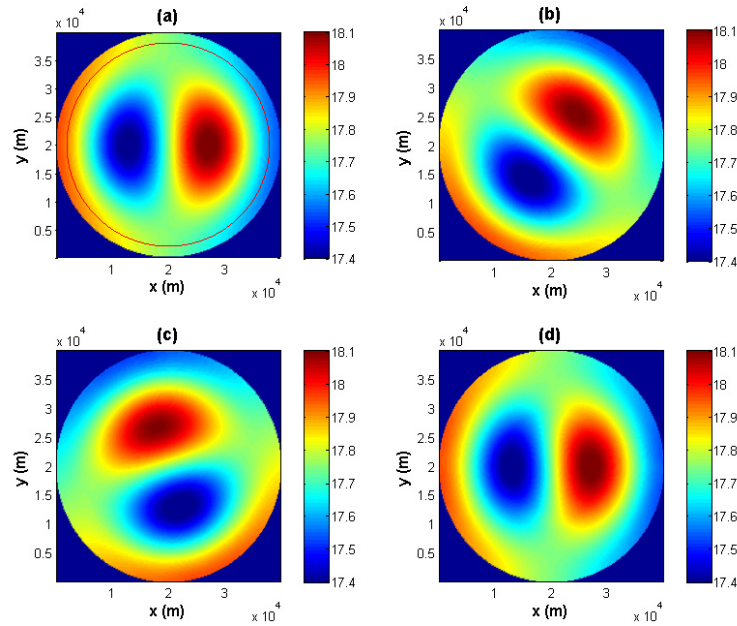

Figure 5.7: w at $z = -10$ m for case I with a constant N at different times: (a) $t = 0$, (b) $t = 2$ hrs, (c) $t = 4$ hrs, and (d) $t = 27$ hrs (approximately 2 periods). The 5th layer is at -10 m instead of -11.25 m due to using of a C-grid.

5.1.2   Non-constant $N(z)$

For a non-constant $N(z)$ two cases are considered. When the model is set to be "quasi-linear", the linear solution is found to be verified. As the amplitude of the waves increases, the density equation can no longer be approximated linearly. In this case, several runs are made to test the nonlinearity of the waves.

"Quasi-linear" case with small amplitudes

In the "quasi-linear" case, we use the setup parameters in Table 5.2.

Table 5.2: Setup parameters for case I with a non-constant $N(z)$, "quasi-linear"

nx, ny, nz	grid points in x, y, z direction	200×200×50
Δt	time step	5 s
V_h, V_z	horizontal and vertical viscosity	0 m^2/s
D_h, D_z	horizontal and vertical diffusivity	0 m^2/s
	free surface or rigid lid?	rigid lid
$\mathbf{u} \cdot \vec{\nabla}\mathbf{u}$	momentum advection included?	no
	temperature advection scheme	33
ω	wave frequency	1.50459×10^{-4} s^{-1}
T_{period}	wave period	11.6 hours
η_0	wave amplitude	1.9 m

We use "winisk" with four CPUs to perform the run in this case. It approximately takes 20 hours to finish five day simulation. Similar to the constant N case, plots of T, u, v, and w are made at different cross-sections. At horizontal cross-sections, the temperature T (Fig. 5.8), the velocities u (Fig. 5.12), v (Fig. 5.13), and w (Fig. 5.14) again rotate counterclockwise without changing their shapes with an approximate period of 11.6 hours. Temperature plots at $x = 20$ km (Fig. 5.9), $y = 20$ km (Fig. 5.10) cross-sections, and one circular vertical cross-section (with a radius $0.9r_0$, Fig. 5.11) confirm our conclusion.

Figure 5.8: T at $z = -14.5$ m for case I with a non-constant $N(z)$ in the "quasi-linear" setup at different times: (a) $t = 0$, (b) $t = 1$ hr, (c) $t = 2$ hrs, and (d) $t = 23$ hrs (approximately 2 periods). The red circle in (a) indicates the circular vertical cross-section picked in Fig. 5.11, $r = 0.9r_0$.
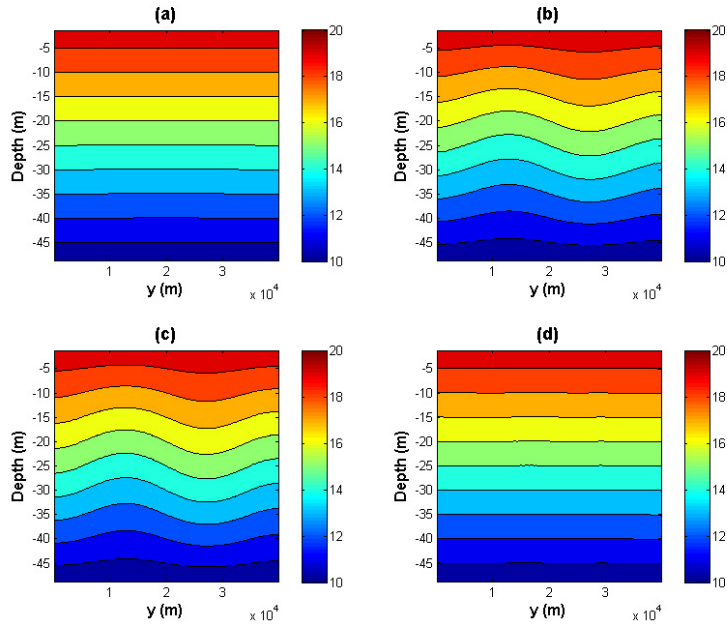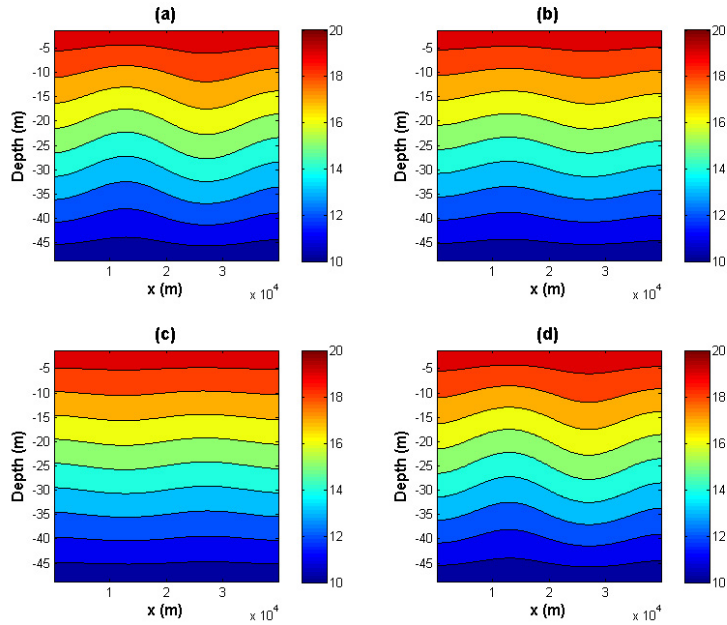

Figure 5.9: T at $x = 20$ km for case I with a non-constant $N(z)$ in the "quasi-linear" setup at different times: (a) $t = 0$, (b) $t = 1$ hr, (c) $t = 2$ hrs, and (d) $t = 23$ hrs (approximately 2 periods).

Figure 5.10: T at $y = 20$ km for case I with a non-constant $N(z)$ in the "quasi-linear" setup at different times: (a) $t = 0$, (b) $t = 1$ hr, (c) $t = 2$ hrs, and (d) $t = 23$ hrs (approximately 2 periods).

Figure 5.11: T at a circular vertical cross-section (radius $0.9r_0 = 18$ km) for case I with a non-constant $N(z)$ in the "quasi-linear" setup at different times: (a) $t = 0$, (b) $t = 1$ hr, (c) $t = 2$ hrs, and (d) $t = 23$ hrs (approximately 2 periods).
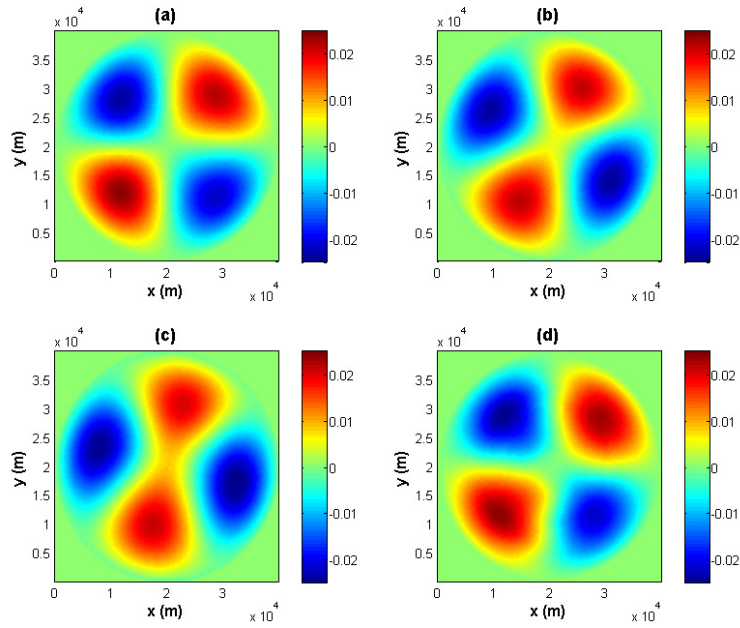
Figure 5.12: u at $z = -19.5$ m for case I with a non-constant $N(z)$ in the "quasi-linear" setup at different times: (a) $t = 0$, (b) $t = 1$ hr, (c) $t = 2$ hrs, and (d) $t = 23$ hrs (approximately 2 periods).
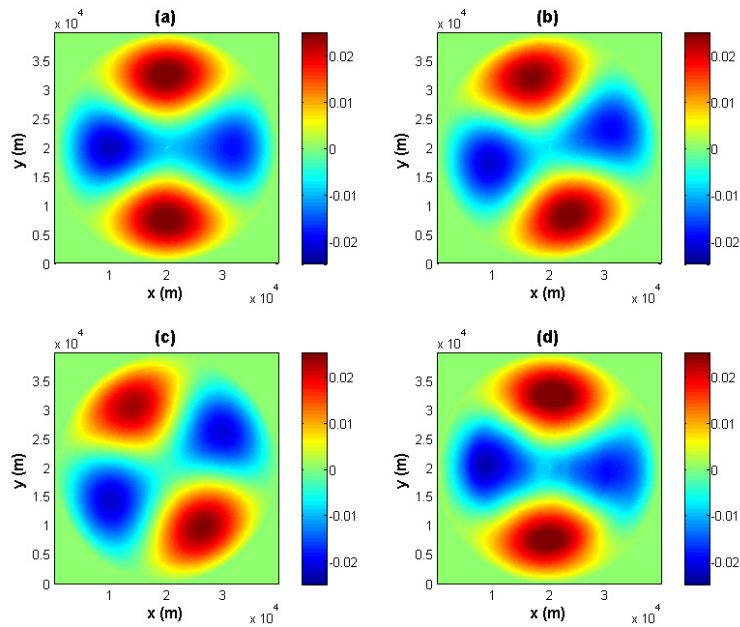
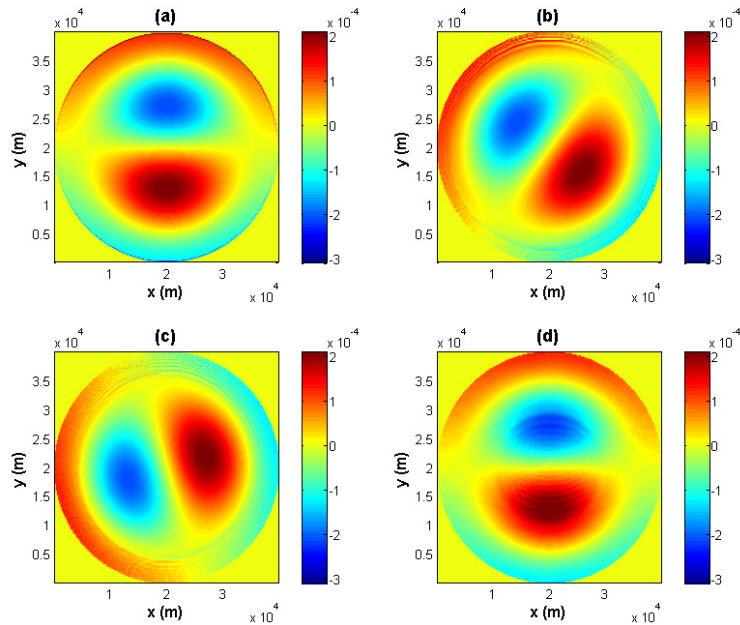Figure 5.13: v at $z = -19.5$ m for case I with a non-constant $N(z)$ in the "quasi-linear" setup at different times: (a) $t = 0$, (b) $t = 1$ hr, (c) $t = 2$ hrs, and (d) $t = 23$ hrs (approximately 2 periods).
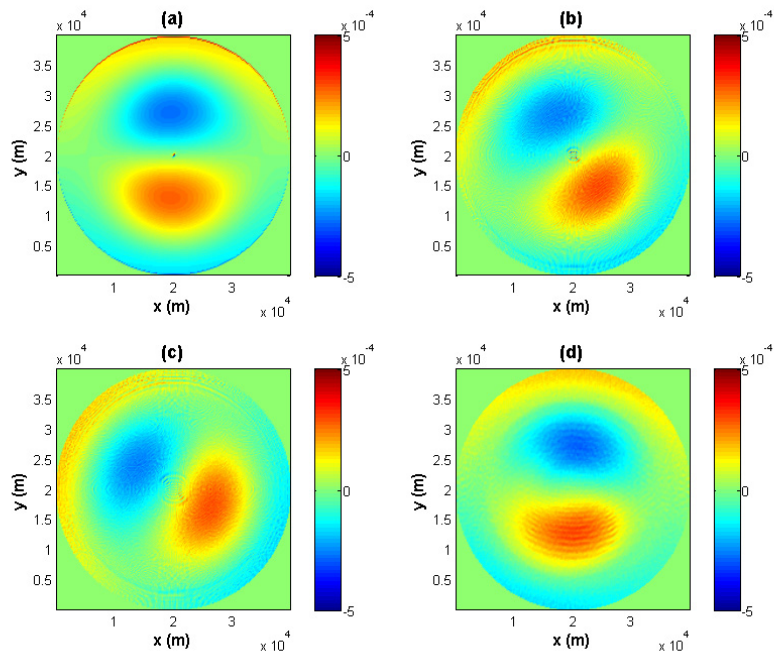
Figure 5.14: w at $z = -19$ m for case I with a non-constant $N(z)$ in the "quasi-linear" setup at different times: (a) $t = 0$, (b) $t = 1$ hr, (c) $t = 2$ hrs, and (d) $t = 23$ hrs (approximately 2 periods).

Fully nonlinear cases with larger amplitudes

As the wave amplitude increases, the waves become more nonlinear. The setup parameters are identical to the 'quasi-linear" case in Table 5.2, except with a larger amplitude 11.6 m and a non-zero viscosity 10^{-4} m^2/s which is added to stabilize the model. With the non-zero viscosity, we apply free slip boundary conditions at the sides and bottom boundaries.

We use "whale" with 4 CPUs to run this case in $200 \times 200 \times 50$ resolution. It approximately takes 20 hours to finish a five day simulation. In $400 \times 400 \times 50$, we use "whale" with 16 CPUs and it takes about three days to finish three day simulation. As usual to begin with, we make a plot of T at the horizontal cross-section $z = -14.5$ m (Fig. 5.15). Because of the nonlinearity the horizontal structure no longer holds its shape while rotating. As can be seen from the circular vertical cross-section with a radius of $0.9r_0$ in Fig. 5.16, the wave clearly steepens at $t = 11$ hrs, and it seems there are solitary-like waves appearing after the steepening. The model resolution is too coarse to confirm the solitary waves. Moreover, we observed that the wave is not degenerated to solitary-like waves completely, as we still see the large parent internal wave later on at $t = 2$ day 12 hrs (Fig. 5.16(f)). This confirms the conclusion in de la Fuente et al. (2008), who state that a basin-scale Poincaré wave in a rotating lake does steepen and form waves with shorter wavelengths, but most energy contained in these waves is transferred back and forth between the parent wave and its subharmonics. Fig. 5.17 gives the circular vertical cross-section with a radius of $r = 0.9r_0$ at a higher horizontal resolution of $400 \times 400 \times 50$. The steepening and degeneration are now clearer as the noise is reduced.

In summary, the analytical solution of the linear system is verified for both a constant N and a non-constant $N(z)$ using the "quasi-linear" setup. As the waves become more nonlinear, they steepen and generate solitary-like waves. However, the energy appears to transfer back and forth between the parent basin-scale wave and the solitary-like waves.
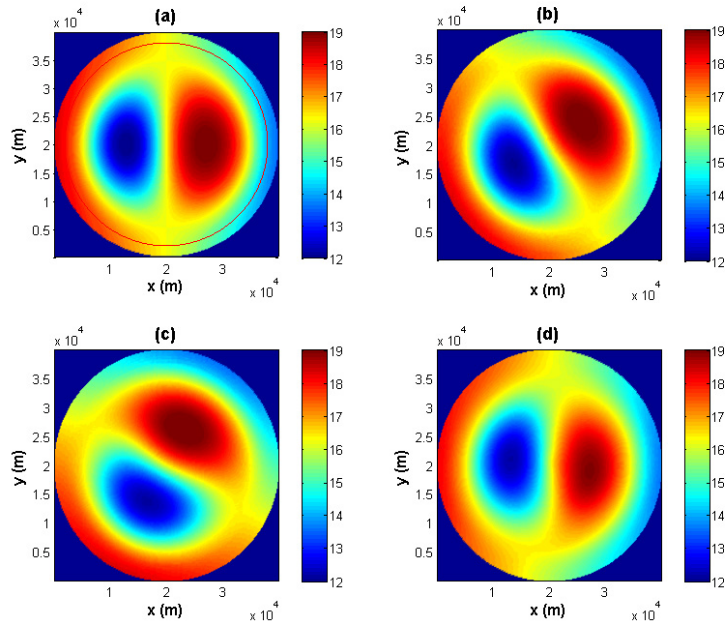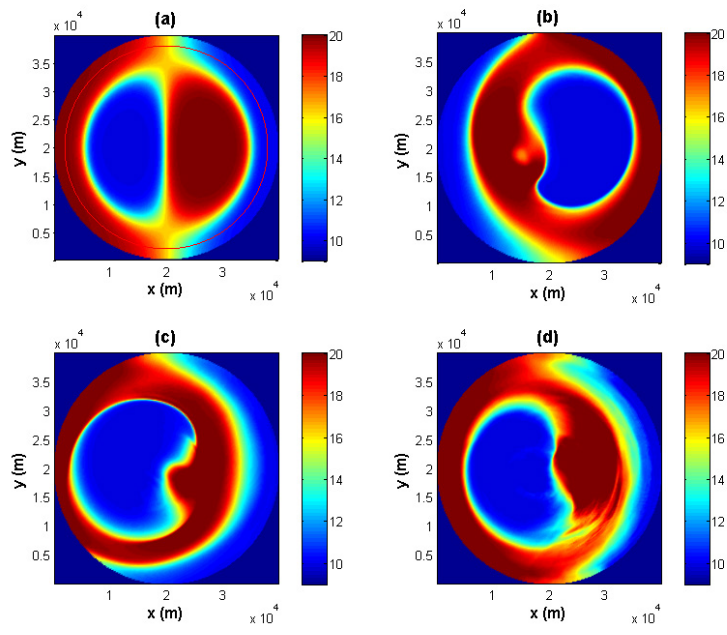
Figure 5.15: T at $z = -14.5$ m for case I with a non-constant $N(z)$ in the fully nonlinear setup at different times: (a) $t = 0$, (b) $t = 6$ hrs, (c) $t = 11$ hrs, and (d) $t = 23$ hrs (approximately 2 periods). The red circle in (a) indicates the circular vertical cross-section picked in Fig. 5.16, $r = 0.9r_0$.
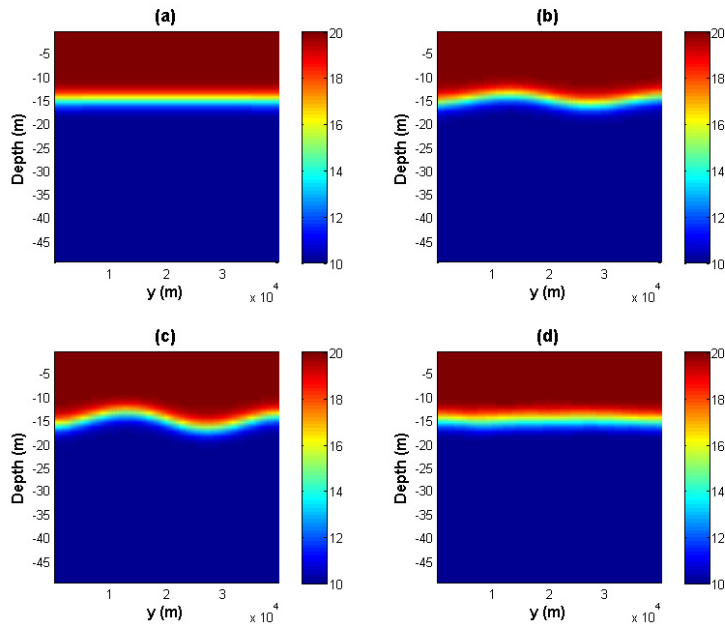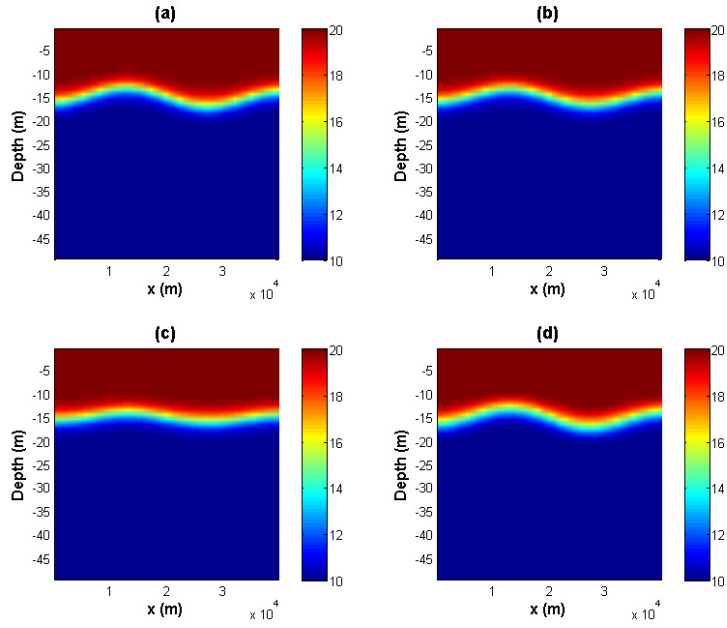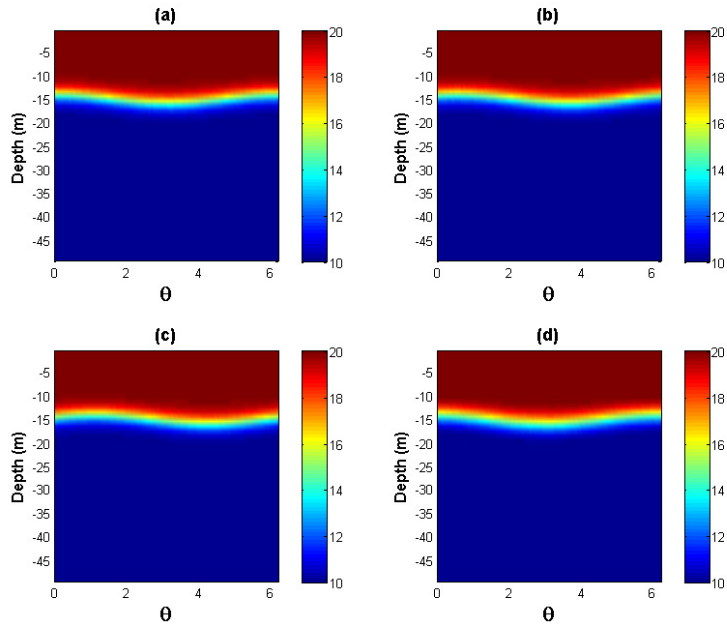
Figure 5.16: T at a circular vertical cross-section (radius $0.9r_0 = 18$ km) for case I with a non-constant $N(z)$ in the fully nonlinear setup at different times (res: $200 \times 200 \times 50$): (a) $t = 0$, (b) $t = 6$ hrs, (c) $t = 11$ hrs, (d) $t = 1$ day 11 hrs, (e) $t = 2$ days 7 hrs, and (f) $t = 2$ days 12 hrs.
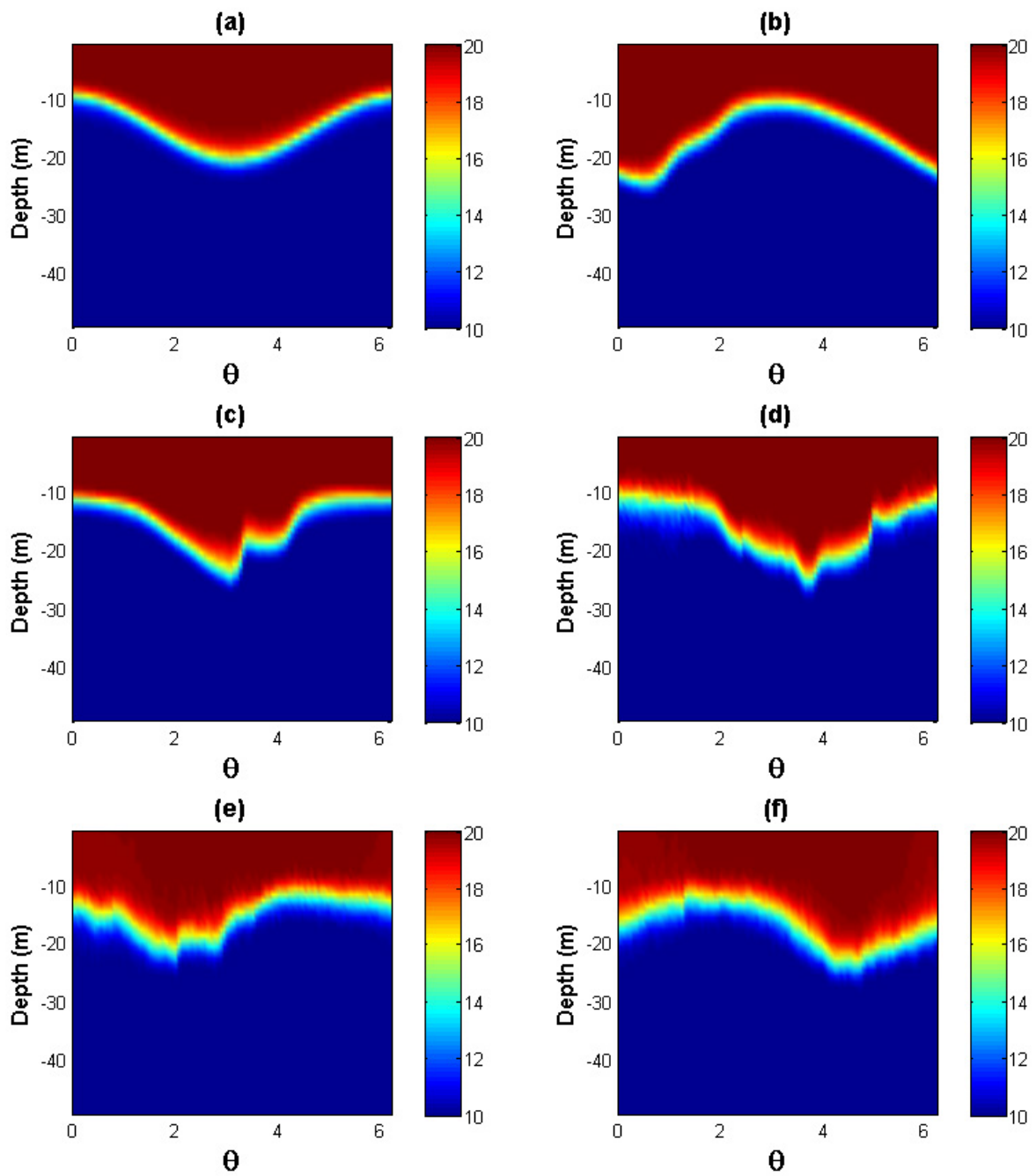
Figure 5.17: Same as Fig. 5.16 but with resolution of $400 \times 400 \times 50$.

5.2 Case II: $C = \beta^2 > 0$

Internal Kelvin waves are investigated in this section. Similar to case I, first the analytical solution of the linear system is verified in the "quasi-linear" setup if N is a constant. Next, for non-constant $N(z)$ two cases again are considered. When the wave amplitude is small, solutions are verified in the "quasi-linear" setup, and when the amplitude increases, the nonlinear effects are studied.

5.2.1 Constant N

When N is constant, we use the setup parameters in Table 5.3. We use "winisk" with four CPUs and it takes about one day to finish 11 day simulation. From the temperature plot at $z = -11.25$ m horizontal cross-section (Fig. 5.18), waves are clearly trapped. From $t = 0$ to $t = 10$ hrs to $t = 20$ hrs, the kelvin wave is rotating counterclockwise. However, there are small waves generated at the lake boundary propagate towards the centre. We will discuss it more in the non-constant $N(z)$ case. At $t = 205$ hrs which is approximately 2 periods, the temperature profile is similar as the one at $t = 0$ except that there are small waves generated at the boundary and propagate in the r direction. The velocities u (Fig. 5.22) and v (Fig. 5.23), plotted at $z = -11.25$ m, basically hold their shapes while rotating counterclockwise. At the $x = 20$ km (Fig. 5.19) and $y = 20$ km (Fig. 5.20) vertical cross-sections, the small propagating waves in the radial direction are clearly shown. In the circular vertical cross-section (with a radius of $0.9r_0$ in Fig. 5.21), the Kelvin wave is propagating around the lake with an approximate period of 101.7 hrs. Therefore, except the small waves in the radial direction, the analytical solution for the linear system is verified. We will analyze these small waves more in the fully nonlinear case.

Table 5.3: Setup parameters for case II with a constant N

$nx \times ny \times nz$	grid points in x, y, z direction	200×200×20
Δt	time step	5 s
V_h, V_z	horizontal and vertical viscosity	0 m^2/s
D_h, D_z	horizontal and vertical diffusivity	0 m^2/s
	free surface or rigid lid?	rigid lid
$\mathbf{u} \cdot \vec{\nabla} \mathbf{u}$	momentum advection included?	no
	temperature advection scheme	33
ω	wave frequency	1.71675×10^{-5} s^{-1}
T_{period}	wave period	101.7 hours
η_0	wave amplitude	2 m
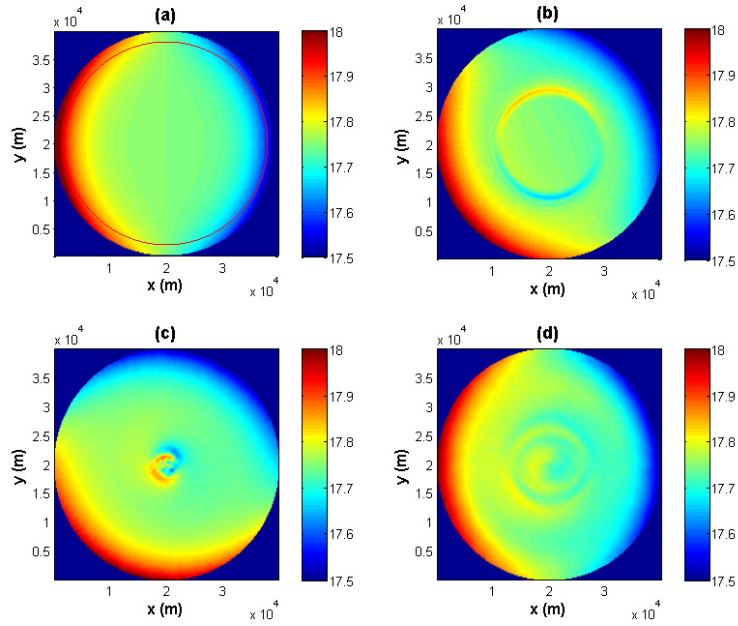
Figure 5.18: T at $z = -11.25$ m for case II with a constant N at different times: (a) $t = 0$, (b) $t = 10$ hrs, (c) $t = 20$ hrs, and (d) $t = 205$ hrs (approximately 2 periods). The red circle in (a) indicates the circular vertical cross-section picked in Fig. 5.21, $r = 0.9r_0$.
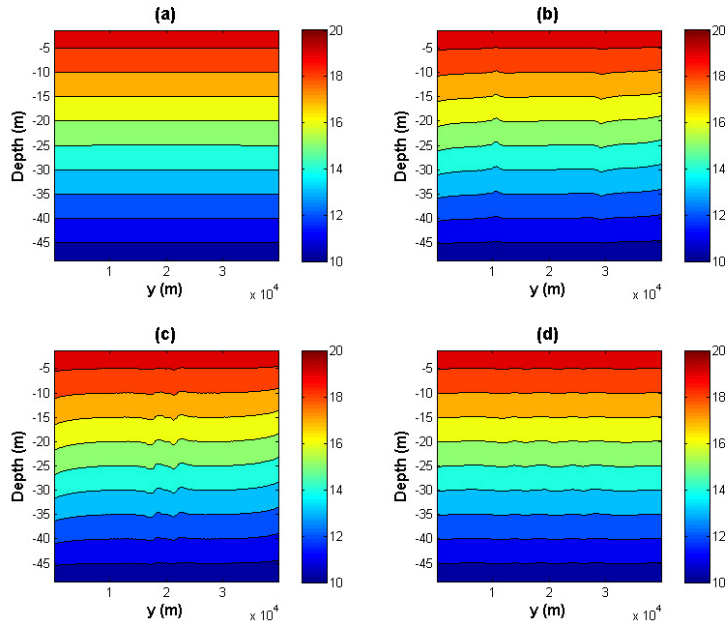

Figure 5.19: T at $x = 20$ km for case II with a constant N at different times: (a) $t = 0$, (b) $t = 10$ hrs, (c) $t = 20$ hrs, and (d) $t = 205$ hrs (approximately 2 periods).
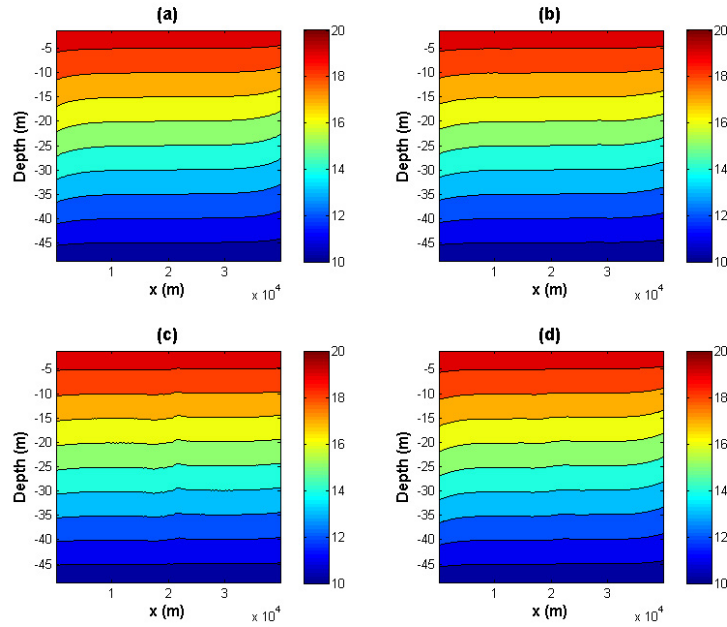
Figure 5.20: T at $y = 20$ km for case II with a constant N at different times: (a) $t = 0$, (b) $t = 10$ hrs, (c) $t = 20$ hrs, and (d) $t = 205$ hrs (approximately 2 periods).
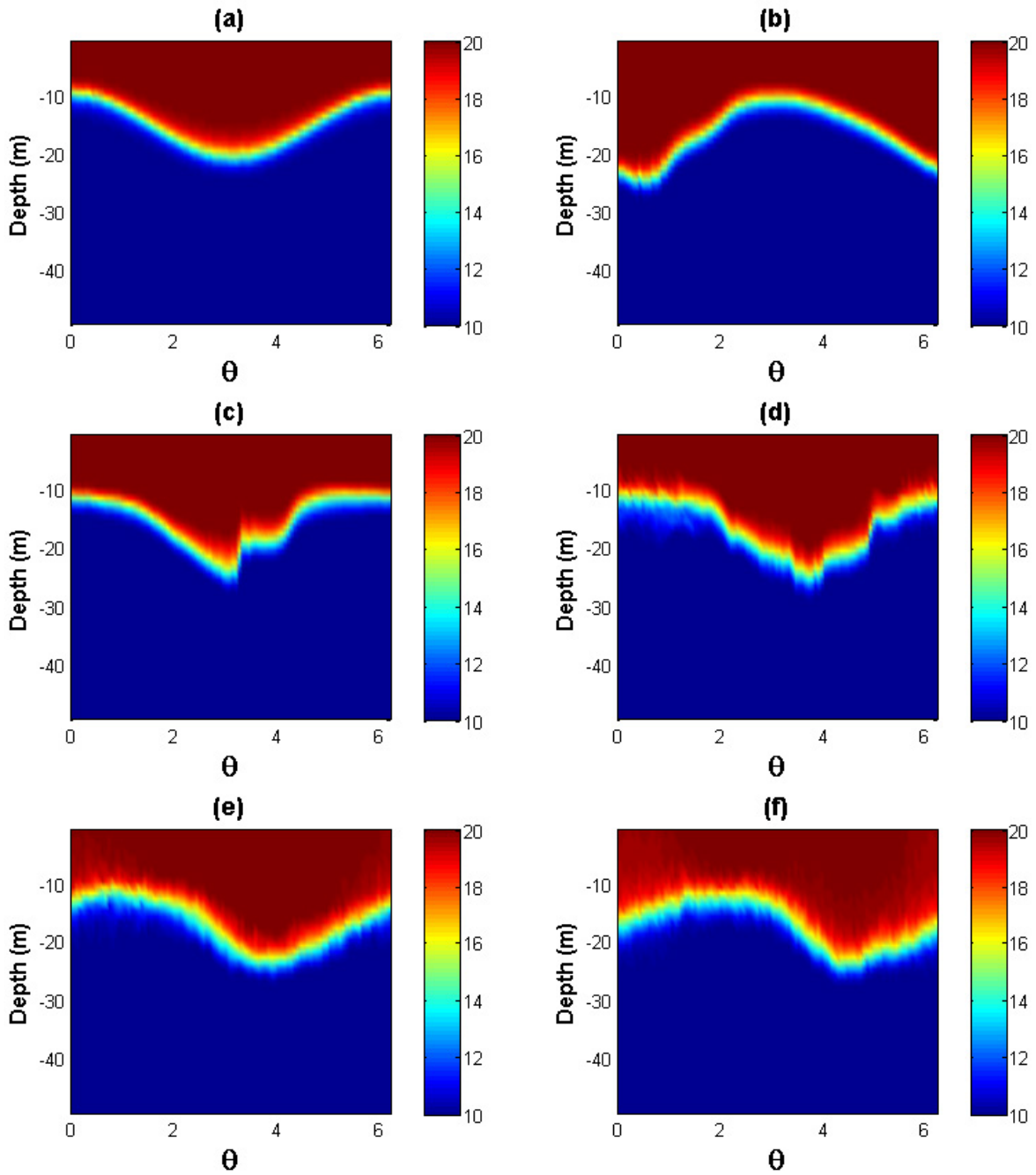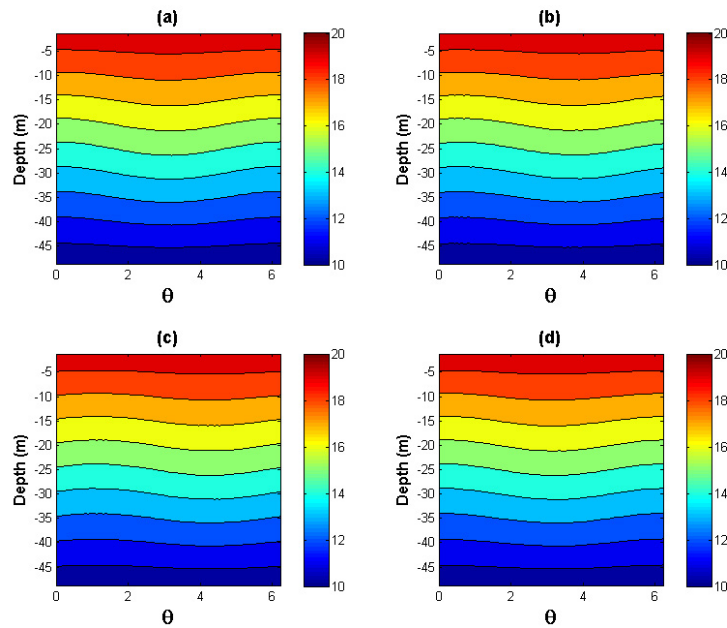

Figure 5.21: T at a circular vertical cross-section (radius $0.9r_0 = 18$ km) for case II with a constant N at different times: (a) $t = 0$, (b) $t = 10$ hrs, (c) $t = 20$ hrs, and (d) $t = 205$ hrs (approximately 2 periods).
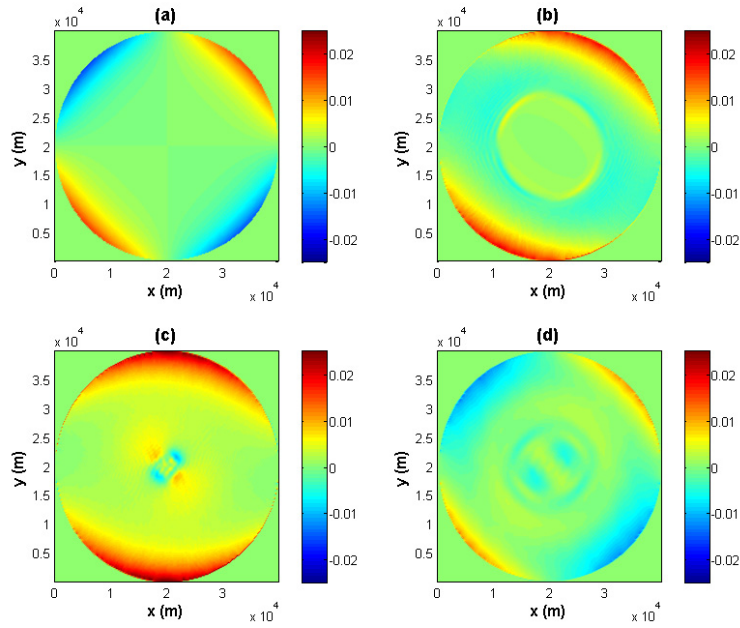
Figure 5.22: u at $z = -11.25$ m for case II with a constant N at different times: (a) $t = 0$, (b) $t = 10$ hrs, (c) $t = 20$ hrs, and (d) $t = 205$ hrs (approximately 2 periods).
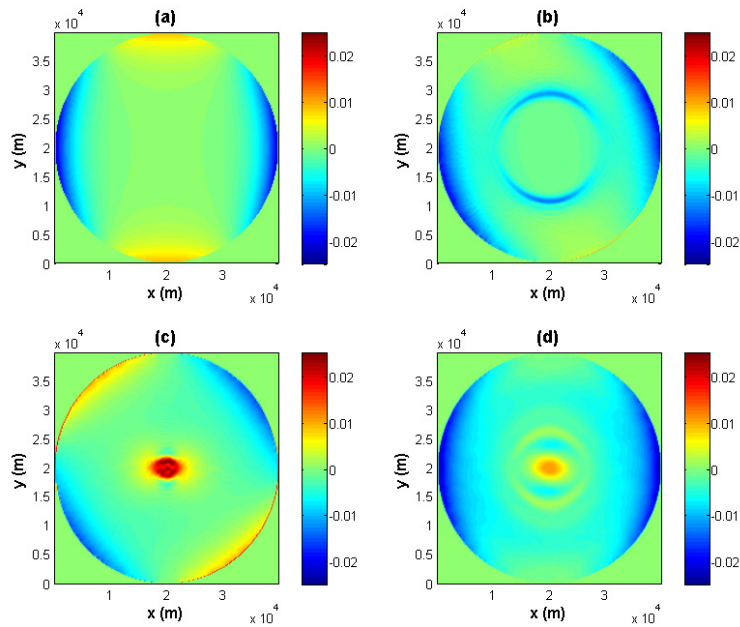
Figure 5.23: v at $z = -11.25$ m for case II with a constant N at different times: (a) $t = 0$, (b) $t = 10$ hrs, (c) $t = 20$ hrs, and (d) $t = 205$ hrs (approximately 2 periods).

5.2.2 Non-constant $N(z)$

"Quasi-linear" case with small amplitudes

For the "quasi-linear" case, we use the setup parameters in Table 5.4.

Table 5.4: Setup parameters for case II with a non-constant $N(z)$, "quasi-linear"

nx, ny, nz	grid points in x, y, z direction	200×200×50
Δt	time step	5 s
V_h, V_z	horizontal and vertical viscosity	0 m^2/s
D_h, D_z	horizontal and vertical diffusivity	0 m^2/s
	free surface or rigid lid?	rigid lid
$\mathbf{u} \cdot \vec{\nabla}\mathbf{u}$	momentum advection included?	no
	temperature advection scheme	33
ω	wave frequency	2.43961×10^{-5} s^{-1}
T_{period}	wave period	71.5 hours
η_0	wave amplitude	1.6 m

We use "winisk" with four CPUs and it takes about one day to finish 8 day simulation. Similar to the constant N case, plots of T, u, and v are made at different cross-sections. At horizontal cross-sections, the temperature T (Fig. 5.24), the velocities u (Fig. 5.28), and v (Fig. 5.29) again rotate counterclockwise without changing their shapes with an approximate period of 71.5 hours. Temperature plots at $x = 20$ km (Fig. 5.25), $y = 20$ km (Fig. 5.26) cross-sections, and one circular vertical cross-section (with a radius of $0.9r_0$ in Fig. 5.27) confirm our conclusion.
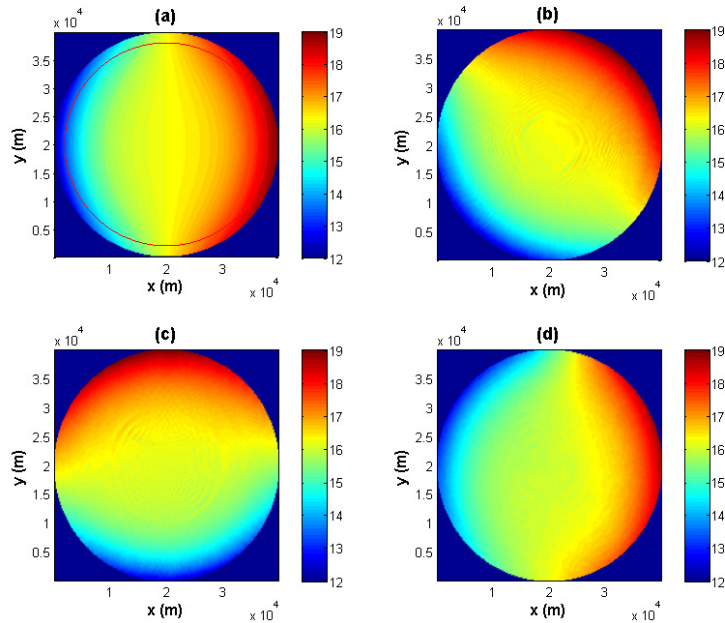
Figure 5.24: T at $z = -14.5$ m for case II with a non-constant $N(z)$ in the "quasi-linear" setup at different times: (a) $t = 0$, (b) $t = 10$ hrs, (c) $t = 20$ hrs, and (d) $t = 142$ hrs (approximately 2 periods). The red circle in (a) indicates the circular vertical cross-section picked in Fig. 5.27, $r = 0.9 r_0$.
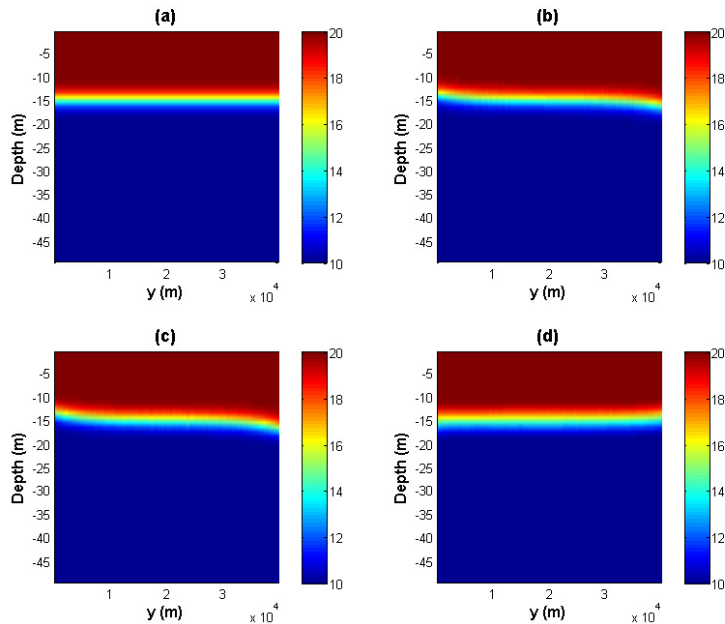
Figure 5.25: T at $x = 20$ km for case II with a non-constant $N(z)$ in the "quasi-linear" setup at different times: (a) $t = 0$, (b) $t = 10$ hrs, (c) $t = 20$ hrs, and (d) $t = 142$ hrs (approximately 2 periods).

92
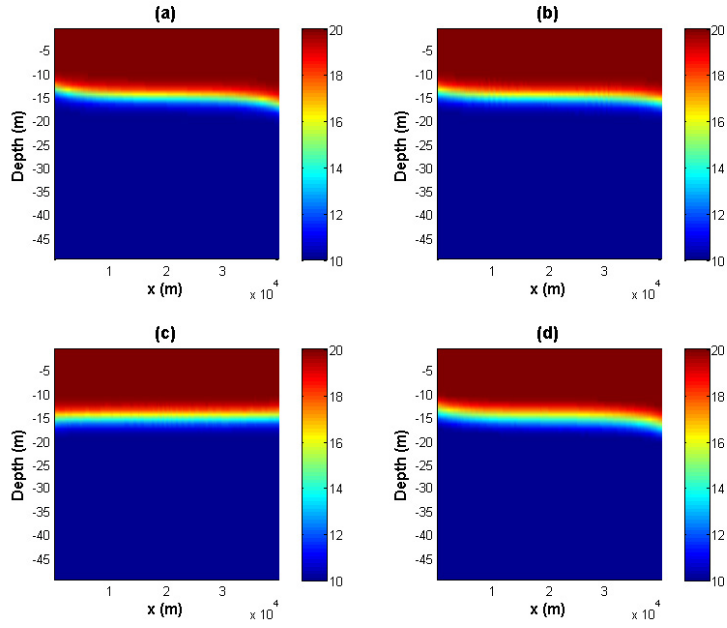
Figure 5.26: T at $y = 20$ km for case II with a non-constant $N(z)$ in the "quasi-linear" setup at different times: (a) $t = 0$, (b) $t = 10$ hrs, (c) $t = 20$ hrs, and (d) $t = 142$ hrs (approximately 2 periods).
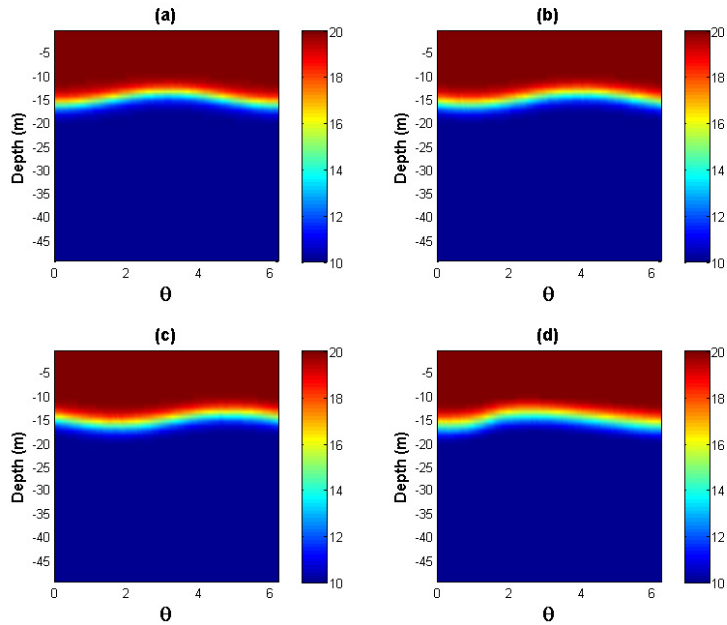
Figure 5.27: T at a circular vertical cross-section (radius $0.9r_0 = 18$ km) for case II with a non-constant $N(z)$ in the "quasi-linear" setup at different times: (a) $t = 0$, (b) $t = 10$ hrs, (c) $t = 20$ hrs, and (d) $t = 142$ hrs (approximately 2 periods).
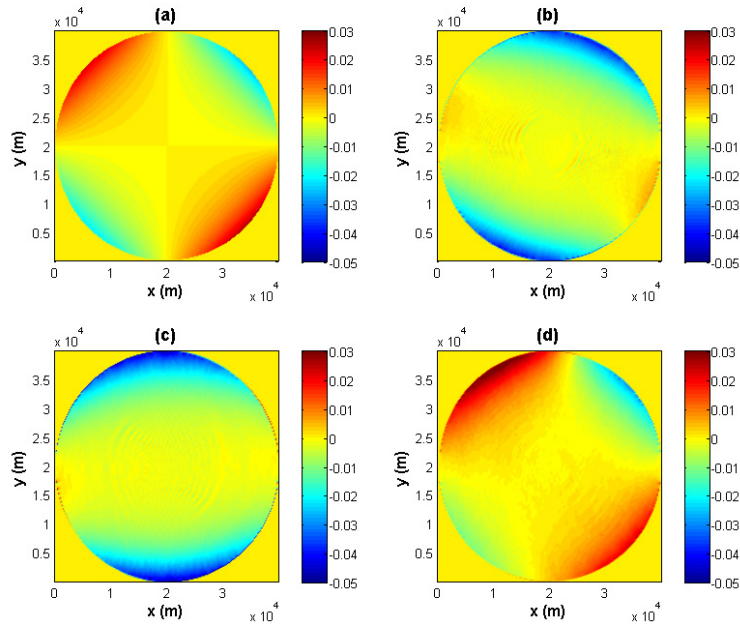
Figure 5.28: u at $z = -4.5$ m for case II with a non-constant $N(z)$ in the "quasi-linear" setup at different times: (a) $t = 0$, (b) $t = 10$ hrs, (c) $t = 20$ hrs, and (d) $t = 142$ hrs (approximately 2 periods).
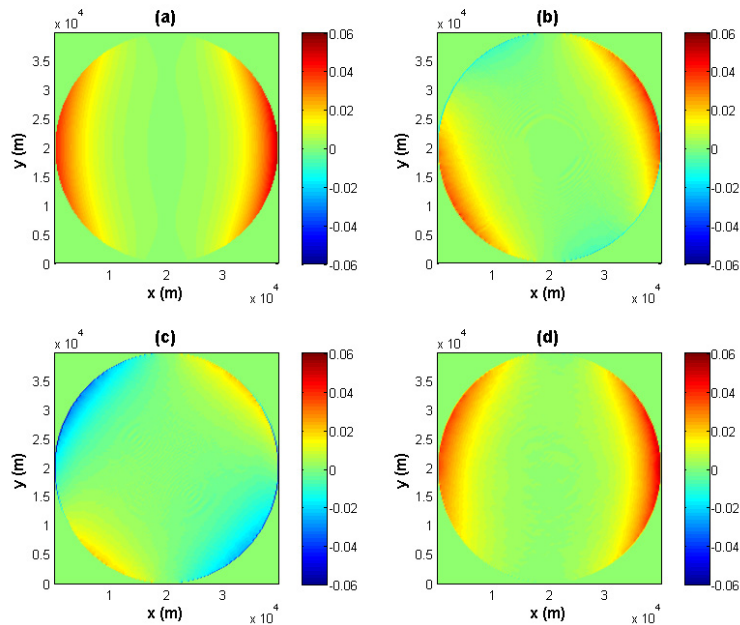
Figure 5.29: v at $z = -4.5$ m for case II with a non-constant $N(z)$ in the "quasi-linear" setup at different times: (a) $t = 0$, (b) $t = 10$ hrs, (c) $t = 20$ hrs, and (d) $t = 142$ hrs (approximately 2 periods).

Fully nonlinear with larger amplitudes

For the fully nonlinear case with larger amplitudes, we use the same parameters as the "quasi-linear" case in Table 5.4, except with a larger amplitude 5.5 m and a non-zero viscosity 10^{-4} m^2/s. With the non-zero viscosity, we apply free slip boundary conditions at the sides and bottom boundary.

We use "whale" with 16 CPUs and it approximately takes nine days to finish six day simulation in $200 \times 200 \times 50$ resolution. First we have a look at the horizontal cross-section at $z = -14.5$ m (Fig. 5.30). The temperature profile rotates around the lake counterclockwise as before, but no longer holds its shape due to the nonlinearity. At $t = 6$ hrs in Fig. 5.30(b), the small waves propagating towards the center appear as seen in the constant case N earlier in section 5.2.1. As time increases the basin-scale wave becomes steeper, as evidenced by the temperature fronts visible in Fig. 5.30(c) to Fig. 5.30(f). In Fig. 5.30(e) and Fig. 5.30(f), we observe another interesting phenomenon. Ripples emerge across the lake starting at the location where the steepening happens. Nonlinear waves analysis tells us that the larger the amplitude of the nonlinear wave is, the faster it travels. Therefore, the waves near the wall travel faster than the ones away from the wall. This confirms the observations in Maxworthy (1983). At the circular vertical cross-section with a radius of $0.9r_0$ in Fig. 5.31, wave steepening is clearly observed and in subplots Fig. 5.31(e) and Fig. 5.31(f) it looks as though solitary-like waves are on the verge of forming, although the resolution is too coarse to tell. Unlike the degeneration of Poincaré waves in the previous section, there is no sign of the energy being transfered back and forth between the parent wave and the solitary-like waves. This again confirms the conclusion in de la Fuente et al. (2008).

Next we increase the resolution to $400 \times 400 \times 50$. We use "whale" with 16 CPUs and it approximately takes one day to finish six day simulation. At $z = -14.5$ m cross-section in Fig. 5.32, the amplitude and wavelength of the small waves in the radial direction become smaller. At the circular vertical cross-section in Fig. 5.33, the solitary-like waves behind the steepening becomes clearer. To confirm our conclusion further, we increase the resolution to $800 \times 800 \times 50$. We use "whale" with 16 CPUs in this simulation. To avoid the blowout, we had to decrease the time step to 0.5 s. As a result, it takes a really long time to finish. When we increase the number of CPUs to 64 the time needed is not shortened as it should due the slow interconnection speed. Fig. 5.34 shows the temperature in $z = -14.5$ m cross-section in the first 19 hours when the solitary-like waves do not appear yet. Again the amplitude and wavelength of the small radial waves decrease as we expect. Hence the small waves are brought by the grid setup. One reason is that we use square grids to approximate a circular lake and waves could be generated at the corner of the grids. We also notice that almost no such small waves appear in the Poincaré wave case. This is probably due to the different initial condition structures they have. Kelvin waves have the maximum amplitude and velocities at the boundary while Poincaré waves' maximum amplitude and velocities are located in the middle of the lake. Hence the grids at the boundary will affect the Kelvin

waves more. Another SHARCNET machine "requin" use a very fast interconnection method quadrics elan4, so our future high resolution work is scheduled to run on "requin" instead of "whale".

In summary, in this section we verified the analytical solution of the linear system numerically in the "quasi-linear" setup, except that there are small waves generated at the boundary and propagating in the radial direction. In the fully nonlinear case, similar small waves appear, but the amplitude and wavelength of these waves decrease as we refine the horizontal resolution. From the circular vertical cross-section we observed that the Kelvin wave steepens and is degenerated to solitary-like waves with shorter wavelength, although more evidences in higher resolutions are needed to confirm. The energy of the waves is transferred to the solitary-like waves and we do not see a sign of the energy being transfered back to the basin-scale waves like in the Poincaré waves case.
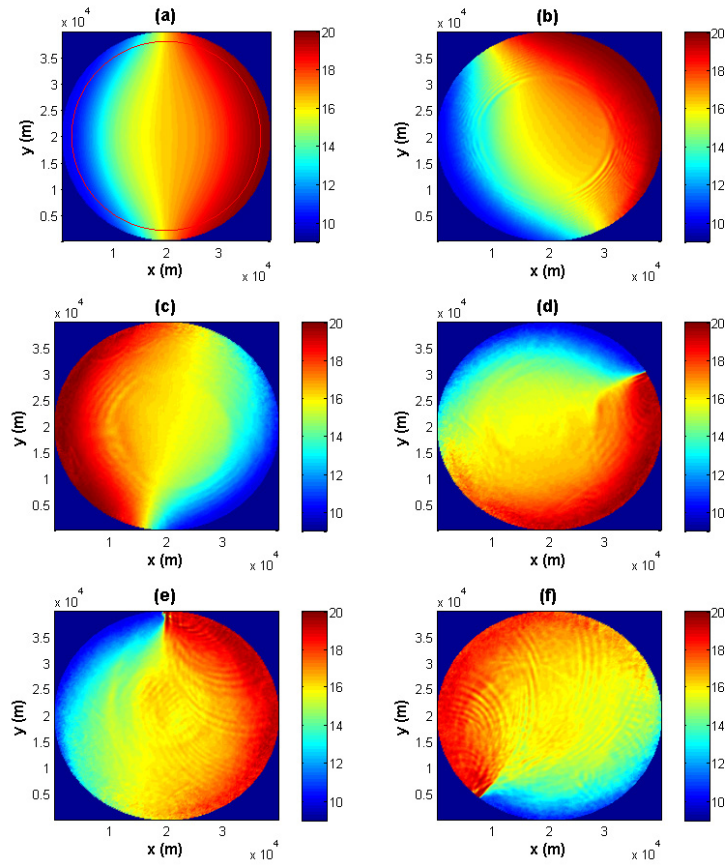
Figure 5.30: T at $z = -14.5$ m for case II with a non-constant $N(z)$ in a fully nonlinear setup at different times (res: $200 \times 200 \times 50$): (a) $t = 0$, (b) $t = 6$ hrs, (c) $t = 33$ hrs, (d) $t = 60$ hrs, (e) $t = 71.5$ hrs (approximately 1 period), and (f) $t = 101$ hrs. The red circle in (a) indicates the circular vertical cross-section picked in Fig. 5.31, $r = 0.9r_0$.
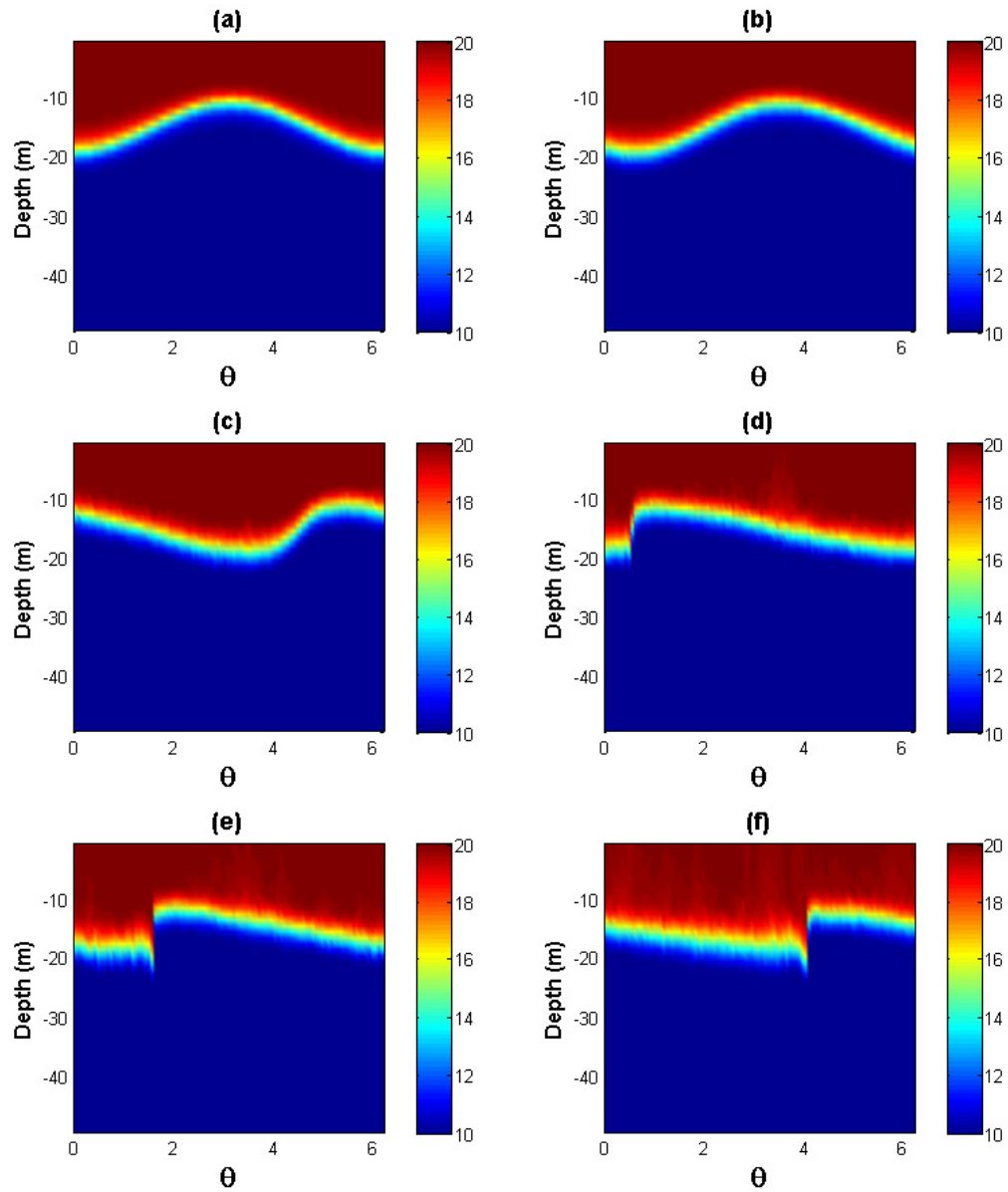
Figure 5.31: T at a circular vertical cross-section (radius $0.9r_0 = 18$ km) for case II with a non-constant $N(z)$ in a fully nonlinear setup at different times (res: $200 \times 200 \times 50$): (a) $t = 0$, (b) $t = 6$ hrs, (c) $t = 33$ hrs, (d) $t = 60$ hrs, (e) $t = 71.5$ hrs (approximately 1 period), and (f) $t = 101$ hrs.
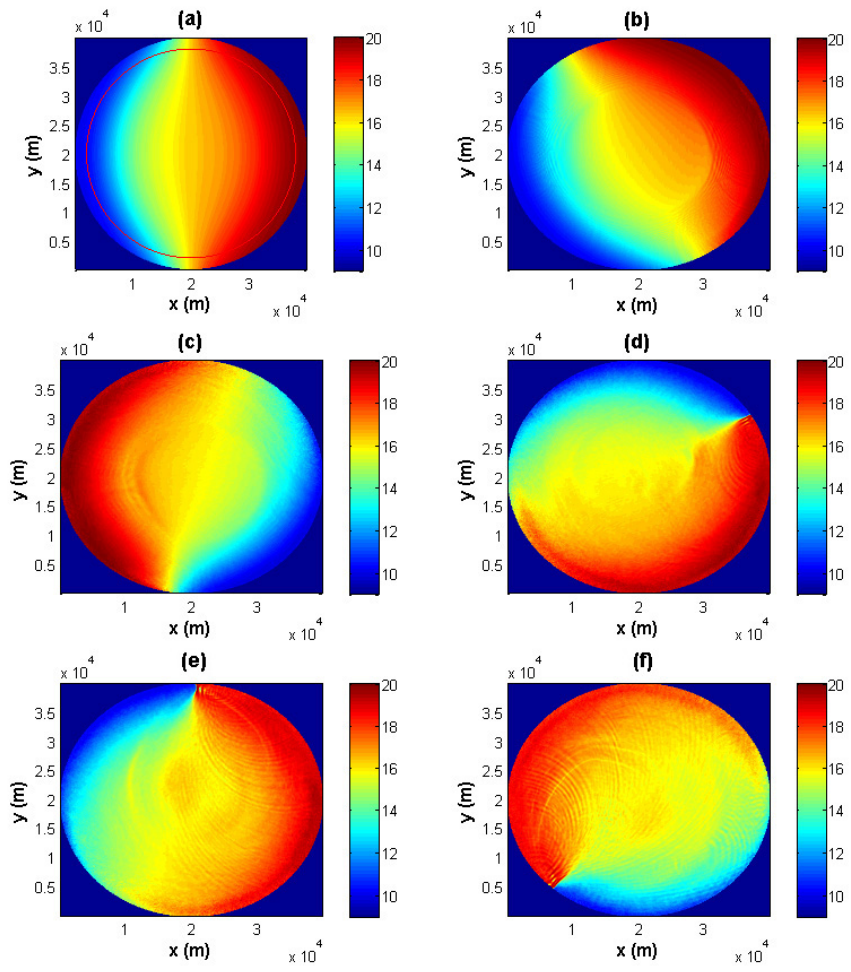
Figure 5.32: Same as Fig. 5.30 but with resolution of $400 \times 400 \times 50$.
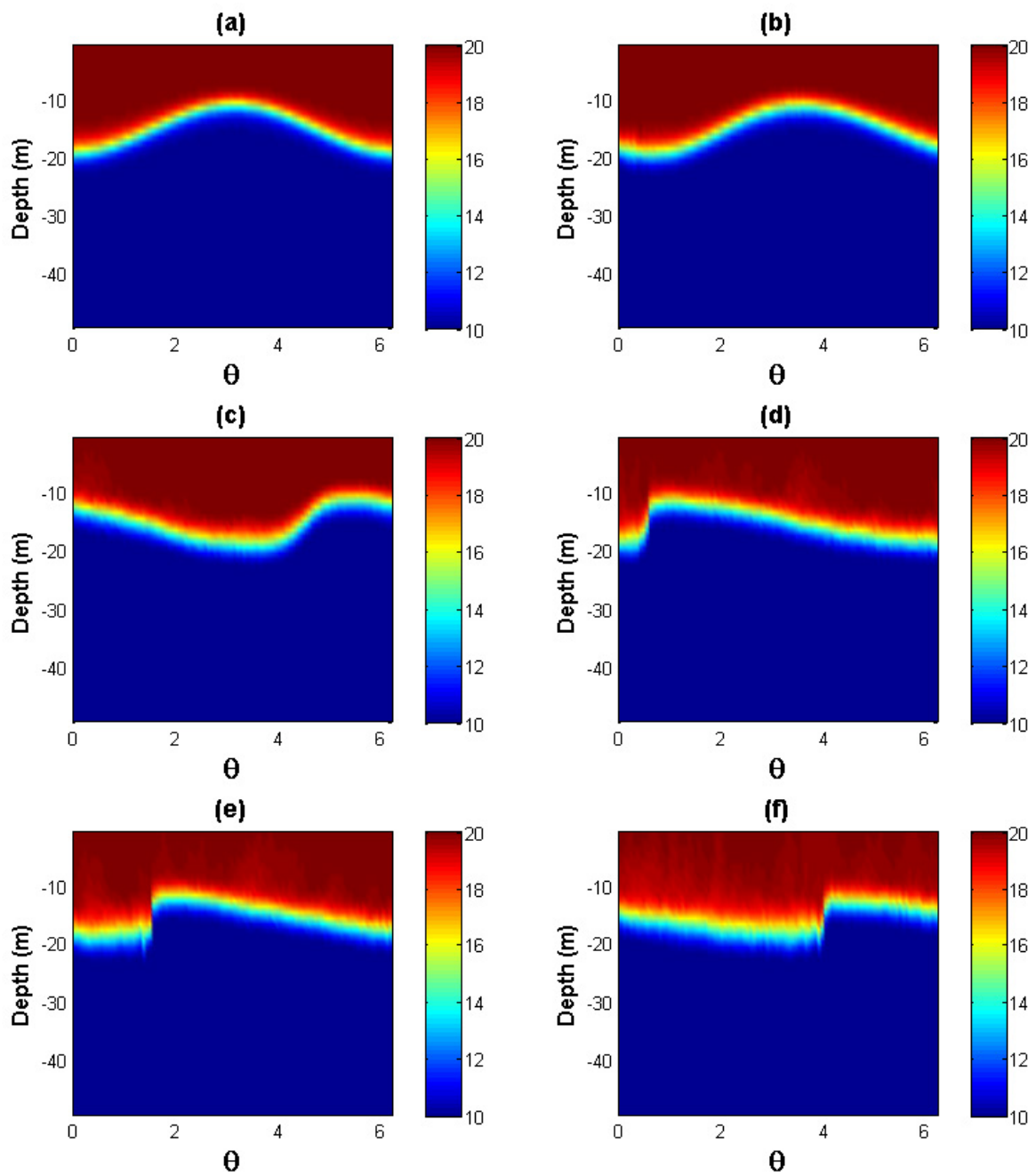
Figure 5.33: Same as Fig. 5.31 but with resolution of $400 \times 400 \times 50$.
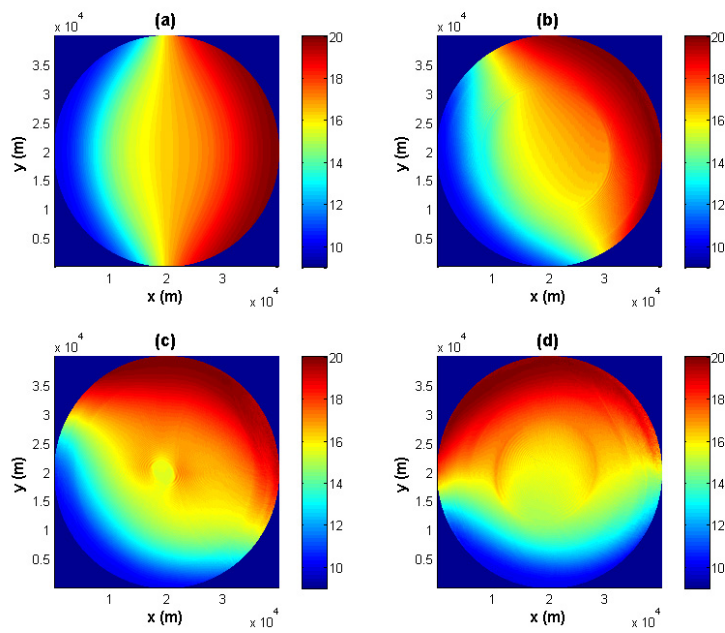
Figure 5.34: T at $z = -14.5$ m for case II with a non-constant $N(z)$ in a fully nonlinear setup at different times (res: $800 \times 800 \times 50$): (a) $t = 0$, (b) $t = 6$ hrs, (c) $t = 12$ hrs, and (d) $t = 19$ hrs.

Chapter 6

Conclusions

6.1 Summary

In this thesis, we derived the analytical solution of the linearized equations governing fluid motions in a rotating, circular lake with a flat bottom. We assumed that the wave solution is propagating around the lake in the angular, θ, direction. After substituting the proposed solution into the governing equations, the method of separation of variables was applied, which introduces a constant C. Different signs of C lead to two cases to investigate: $C > 0$ giving internal Poincaré waves and $C < 0$ giving internal Kelvin waves. When $C = 0$ there appears to be no solutions of the linear problem.

The analytical solution of the linear system is verified for Poincaré waves and Kelvin waves with the buoyancy frequency N either a constant or dependent on z using the MITgcm, in a lake with radius of 20 km and depth of 50 m. The result of Poincaré waves simulations is what we expected. However, in the Kelvin waves case, small waves are generated at the side boundary and propagate in the radial direction. As the horizontal resolution increases, both the amplitude and wavelength of these small waves decrease. One possible reason is that the use of square grids to approximate the circular lake. When the amplitude of the waves increases, nonlinear and non-hydrostatic effects were studied. Poincaré waves steepen and form solitary-like waves with shorter wavelengths, but most energy is transferred back and forth between the parent wave and the solitary-like waves. Kelvin waves, on the other hand, steepen and lose their energy to solitary-like waves which are formed after the steepening. The appearance of the solitary-like waves is not absolutely clear and higher resolution is required to study such waves further. This conclusion agrees with de la Fuente et al. (2008).

Meanwhile, we tested all the temperature advection schemes in the MITgcm using the tilted tank simulation and concluded that schemes 2 and 33 are better choices in this type of computation. We also ran this simulation using the IGW model and the result in IGW is almost the same as the simulation we did using

the MITgcm when scheme 2 was used. The only difference is that the waves travel faster in the MITgcm than in IGW, something we will continue to study in the future.

6.2   Future Work

There are many obvious extensions to this work. First of all, in the tilted tank simulation we found out that internal waves travel faster in the MITgcm than in IGW, which is an interesting phenomenon to continue investigating. One problem in the Kelvin waves simulations is the appearance of small waves generated at the side boundary and traveling in the radial direction. Although we have shown that the amplitude and wavelength of these waves become smaller as the horizontal resolution increases, we need to find out the cause of the waves. One reason for the appearance of the short waves is that we use square grids to approximate a circular lake, and hence waves could be generated at the corners. The solitary-like waves in the Kelvin waves case is not absolutely convincing in $400 \times 400 \times 50$ resolution, so we need to repeat the experiment at higher resolutions. Using the $800 \times 800 \times 50$ resolution, we have to use a tiny time step (0.5 s), which results in an extremely long running time. Further studies are needed to investigate the model to determine if it can be run at higher resolutions using a much larger time step. Since the wind is one of the most important energy sources to generate internal waves, we certainly need to add wind in the simulations. We have already used the MITgcm to reproduce Kelvin waves and full upwelling in the flat bottom case in Beletsky et al. (1997) where POM and DieCAST were used, and we will present the results in future work although for now a slight problem in the position of Kelvin waves needs to be solved. Moreover, the energy transfer among internal waves is also an important topic to discuss further. Using a similar method as the one in Hodges et al. (2000), an analogical regime to Fig. 4.4 for rotating internal waves would be very useful. Finally, the lake we are working on is an idealized model, so adding realistic topography is a plan for the future studies.

Appendices

Appendix A

Running MITgcm

A.1 Directory structure

Each simulation directory has the following subdirectories:

code: Contains the code particular to the simulation. This directory includes at least the following files:

packages.conf: Declares the list of packages or package groups to be used, e.g., geophysical fluid dynamics package, external forcing package, Shapiro filters package etc.

CPP OPTIONS.h: declares CPP (the C pre-processor to use) keys related to the numerical model part of the code. The non-hydrostatic balance is set here using

```
define ALLOW_NONHYDROSTATIC
```

SIZE.h: Declares size of underlying computational grid. Below is a sample code of *SIZE.h*.

```
C      Name: SIZE.h
C      sNx - No. X points in sub-grid.
C      sNy - No. Y points in sub-grid.
C      OLx - Overlap extent in X.
C      OLy - Overlat extent in Y.
C      nSx - No. sub-grids in X.
C      nSy - No. sub-grids in Y.
C      nPx - No. of processes to use in X.
C      nPy - No. of processes to use in Y.
C      Nx  - No. points in X for the total domain.
C      Ny  - No. points in Y for the total domain.
C      Nr  - No. points in Z for full process domain.
       INTEGER sNx
       INTEGER sNy
```

```
      INTEGER OLx
      INTEGER OLy
      INTEGER nSx
      INTEGER nSy
      INTEGER nPx
      INTEGER nPy
      INTEGER Nx
      INTEGER Ny
      INTEGER Nr
      PARAMETER (
     &            sNx =  200,
     &            sNy =  200,
     &            OLx =   2,
     &            OLy =   2,
     &            nSx =   1,
     &            nSy =   1,
     &            nPx =   1,
     &            nPy =   1,
     &            Nx  = sNx*nSx*nPx,
     &            Ny  = sNy*nSy*nPy,
     &            Nr  =   20)
C     MAX_OLX  - Set to the maximum overlap region size of any array
C     MAX_OLY    that will be exchanged. Controls the sizing of exch
C                routine buufers.
      INTEGER MAX_OLX
      INTEGER MAX_OLY
      PARAMETER ( MAX_OLX = OLx,
     &            MAX_OLY = OLy )
```

input: Contains the input data files required to run the program. This directory includes at least the following files:

data: Written as a namelist, specifies the main parameters for the simulation. The sample code is shown below.

data.pkg: Contains parameters related to the packages used in the simulation.

eedata: This file contains execution environment data.

```
# Name: data
# Model parameters
# Continuous equation parameters
 &PARM01
 tRef=,
 sRef=20*0.,
 viscAz=0.,
 viscAh=0.,
 no_slip_sides=.FALSE.,
```

```
 no_slip_bottom=.FALSE.,
 diffkhT=0.,
 diffKzT=0.,
 momAdvection=.FALSE.,
 f0=1.0E-4,
 beta=0,
 tAlpha=2.0E-4,
 sBeta =0.,
 gravity=9.81,
 useConstantF=.TRUE.,
 momForcing=.FALSE.,
 saltStepping=.FALSE.,
 staggerTimeStep=.TRUE.,
 rigidLid=.TRUE.,
 implicitFreeSurface=.FALSE.,
 nonHydrostatic=.TRUE.,
 eosType='LINEAR',
 readBinaryPrec=64,
 &
# Elliptic solver parameters
 &PARM02
 cg2dMaxIters=1000,
 cg2dTargetResidual=1.E-7,
 &
# Time stepping parameters
 &PARM03
 startTime=0,
 endTime=2.0E5,
 deltaTmom=10.0,
 deltaTtracer=10.0,
 abEps=0.1,
 pChkptFreq=25920000000000000.0,
 chkptFreq=120000000000000.0,
 dumpFreq=3600.0,
 monitorFreq=3600.0,
 &
# Gridding parameters
 &PARM04
 usingCartesianGrid=.TRUE.,
 usingSphericalPolarGrid=.FALSE.,
 delX=200*200,
 delY=200*200,
 delZ=20*2.5,
 &
 &PARM05
```

```
 bathyFile='topog.box',
 hydrogThetaFile='tRefFile.bin',
 hydrogSaltFile=,
 zonalWindFile=,
 meridWindFile=,
 uVelInitFile='uVelInit.bin',
 vVelInitFile='vVelInit.bin',
#pSurfInitFile='SurfInit.bin',
#pLoadFile='pInit.bin',
 &
```

A.2 Compiling and running

A.2.1 Single processor

First an option file *winisk* in */tools/build_options* need to be created for the specific hardware and operation system. Next, compile the code which is simply built in the */input* directory here.

```
../../../tools/genmake2 -mods=../code
 -of ../../../tools/build_options/winisk
make depend
make
```

After compiling, an executable file *mitgcmuv* is generated which can be run by the following command,

```
./mitgcmv > out.txt
```

A.2.2 Multiple processors: MPI

MPI (Message Passing Interface) is a specification for an API (Application Programming Interface) that allows many computers to communicate with one another. MITgcm can use MPI to perform jobs using multiple processors. *SIZE.h* in */code* need to be modified to specify the number of processors accordingly. Different option file *winisk_mpi* in */tools/build_options* need to be created. Building in the input directory follows,

```
../../../tools/genmake2 -mods=../code
 -of ../../../tools/build_options/winisk_mpi -mpi
make depend
make
```

The executable file *mitgcmuv* can be run by the command if four processors are used,

```
mpirun -n -4 ./mitgcmv
```

A.3   Viewing output

The traditional output files are generated by the *mdsio* package. The instantaneous state of the model is stored at a specified frequency,

U.000nIter: zonal component of velocity field (m/s).
V.000nIter: meridional component of velocity field (m/s).
W.000nIter: vertical component of velocity field (m/s).
T.000nIter: potential teperature (°C).
S.000nIter: salinity (psu).
Eta.000nIter: surface elevation (m).

The chain *00000nIter* consists of ten figures that specify the iteration number at which the output is stored. The *mdsio* model data are written to "data/meta" format. The .data file contains the data written in binary form and the .meta file is a "header" file that contains information about the size and the structure of the .data file. MITgcm provides a script *rdmds.m* to read the data, e.g.,

```
T=rdmds('T',0);contourf(T(:,:,2));colorbar;
```

MITgcm also supports NetCDF output files by mnc package and we do not explain more details here.

Appendix B

Matlab Scripts

B.1 Initialization in case I with a constant N

Below is the Matlab code for the Initialization in case I with a constant N which we used in section 4.4.1).

```
ieee='b';accuracy='real*8';
%resolution 200*200*20
nx=200;ny=200;nz=20;
%A is the parameter which varies the wave amplitude
%L is the diameter of the lake and H is the depth
A=3e-2;L=40000;H = 50;
%center of the lake
cx=L/2;cy=L/2;
dx=L/nx;dy=L/ny;dz=H/nz;
%Please see detals about the C-grids in Figure 4.14
xCN=0:dx:(L-dx);%xCN: x points at the sides of grids
yCN=0:dy:(L-dy);%yCN: y points at the sides of grids
xHF=dx/2:dx:L;%xCHF: x points at the middles of grids
yHF=dy/2:dy:L;%yCHF: y points at the middles of grids
zCN=0:(-dz):(-H+dz);%zCN: z points at the sides of grids
z=-dz/2:(-dz):(-H);%z: z points at the middles of grids
G=numgrid('D',nx);%Generate the approximate circular lake

%Talpha is the coefficient of thermal expansion.
g = 9.8;rho0 = 999.8;Talpha = 2e-4;n=1;m=pi/H;
omega = 1.290746491E-4;f=1E-4;N = 1.98E-2;
alpha = sqrt(m^2*(omega^2-f^2)/(N^2-omega^2));
%Surface temperature Ts and bottom temperature Tb
Ts=20; Tb=10;
%h(x,y) is the depth at (x,y), which is used to generate the topography
```

```matlab
h=zeros(nx,ny);
%r and theta at the center and on the sides of the grids
rC = zeros(nx,ny);rU = zeros(nx,ny);rV = zeros(nx,ny);
thetaC = zeros(nx,ny);thetaU = zeros(nx,ny);thetaV = zeros(nx,ny);
%urU and UthetaU is the the velocities at (xCN,yHF) where u is initialized
%urV and UthetaV is the the velocities at (xHF,yCN) where v is initialized
urU = zeros(nx,ny,nz);urV = zeros(nx,ny,nz);
uthetaU = zeros(nx,ny,nz);uthetaV = zeros(nx,ny,nz);
u = zeros(nx,ny,nz);v = zeros(nx,ny,nz);w = zeros(nx,ny,nz);
%p is the pressure perturbation and rho_p is the density perturbation.
p = zeros(nx,ny,nz);rho_p = zeros(nx,ny,nz);
%T_p is the temperature perturbation and T_LG is the total temperature.
T_p = zeros(nx,ny,nz);T_LG=zeros(nx,ny,nz);

%Generate the topography
for i=1:nx
    for j=1:ny
        if (G(ny+1-j,i)>0)%The order of G(i,j) is different than the one
                            %we used for the grids.
            rC(i,j) = sqrt((xHF(i)-cx)^2+(yHF(j)-cy)^2);
            rU(i,j) = sqrt((xCN(i)-cx)^2+(yHF(j)-cy)^2);
            rV(i,j) = sqrt((xHF(i)-cx)^2+(yCN(j)-cy)^2);
            thetaC(i,j) = atan2(yHF(j)-cy,xHF(i)-cx);
            thetaU(i,j) = atan2(yHF(j)-cy,xCN(i)-cx);
            thetaV(i,j) = atan2(yCN(j)-cy,xHF(i)-cx);
            h(i,j)=-H;%h(x1,y1) = zero means there is no water at (x1,y1).
        end
    end
end
%Generate the topography file topog.box.
fid=fopen('topog.box','w',ieee); fwrite(fid,h,accuracy); fclose(fid);
%Initial velocities
for i=1:nx
    disp(i)
    for j=1:ny
        for k=1:nz
            if (G(ny+1-j,i)>0)
                %Below are the points in the lake which do not include the
                %points on the boundaries.
                if (G(ny+1-j-1,i)>0 && G(ny+1-j+1,i)>0 ...
                        && G(ny+1-j,i-1)>0 && G(ny+1-j,i+1)>0)
                    urU(i,j,k)=A*(1/(f^2-omega^2))...
                        *(f*besselj(1,alpha*rU(i,j))/rU(i,j) ...
                        - omega*alpha*(-besselj(2,alpha*rU(i,j))...
                        + besselj(1,alpha*rU(i,j))/(alpha*rU(i,j))))...
```

```
                         *sin(n*thetaU(i,j))*cos(m*z(k));
            urV(i,j,k)=A*(1/(f^2-omega^2))...
                *(f*besselj(1,alpha*rV(i,j))/rV(i,j) ...
                - omega*alpha*(-besselj(2,alpha*rV(i,j))...
                + besselj(1,alpha*rV(i,j))/(alpha*rV(i,j))))...
                         *sin(n*thetaV(i,j))*cos(m*z(k));
            uthetaU(i,j,k)=A*(1/(f^2-omega^2))...
                *(-omega*besselj(1,alpha*rU(i,j))/rU(i,j) ...
                + f*alpha*(-besselj(2,alpha*rU(i,j))...
                +besselj(1,alpha*rU(i,j))/(alpha*rU(i,j))))...
                         *cos(n*thetaU(i,j))*cos(m*z(k));
            uthetaV(i,j,k)=A*(1/(f^2-omega^2))...
                *(-omega*besselj(1,alpha*rV(i,j))/rV(i,j) ...
                + f*alpha*(-besselj(2,alpha*rV(i,j))...
                + besselj(1,alpha*rV(i,j))/(alpha*rV(i,j))))...
                         *cos(n*thetaV(i,j))*cos(m*z(k));
    %u is calculated using urU and uthetaU, which are obtained
    %from points (xCN,yHF). The same method applies to v.
            u(i,j,k) = urU(i,j,k)*cos(thetaU(i,j)) ...
                - uthetaU(i,j,k)*sin(thetaU(i,j));
            v(i,j,k) = urV(i,j,k)*sin(thetaV(i,j)) ...
                + uthetaV(i,j,k)*cos(thetaV(i,j));
     elseif(G(ny+1-j-1,i)>0 && G(ny+1-j+1,i)>0 ...
            && G(ny+1-j,i-1)==0 && G(ny+1-j,i+1)>0)%left boundary
            u(i,j,k) = 0;
      elseif(G(ny+1-j-1,i)>0 && G(ny+1-j+1,i)>0 ...
            && G(ny+1-j,i-1)>0 && G(ny+1-j,i+1)==0)%right boundary
            u(i+1,j,k) = 0;
      elseif(G(ny+1-j-1,i)>0 && G(ny+1-j+1,i)==0 ...
            && G(ny+1-j,i-1)>0 && G(ny+1-j,i+1)>0)%bottom boundary
            v(i,j,k) = 0;
      elseif((G(ny+1-j-1,i)==0 && G(ny+1-j+1,i)>0 ...
            && G(ny+1-j,i-1)<0 && G(ny+1-j,i+1)>0))%top boundary
            v(i,j+1,k) = 0;
      end
      w(i,j,k) = -A*alpha^2*omega*besselj(1,alpha*rC(i,j))...
          /((f^2 - omega^2)*m)*sin(n*thetaC(i,j))*sin(m*zCN(k));
      p(i,j,k)= A*besselj(n,alpha*rC(i,j))...
          *cos(n*thetaC(i,j))*cos(z(k));
      p(i,j,k) = p(i,j,k)*rho0;
      rho_p(i,j,k) = N^2/(omega*g)*(-A)*alpha^2*omega...
          *besselj(1,alpha*rC(i,j))/((f^2 - omega^2)*m)...
                  *cos(n*thetaC(i,j))*sin(m*z(k));
      T_p(i,j,k) = -rho_p(i,j,k)/Talpha;
end
```

```
        end
    end
end

%Next we generate Tref file
delta = N^2/(g*Talpha)*H/nz;
T0 = (Ts-delta/2):(-delta):Tb;%background density
for k=1:nz
    T_LG(:,:,k) = T0(1,k) +T_p(:,:,k);
end
T_LGX100 = zeros(ny,nz);T_LGX100(:,:)=T_LG(nx/2,:,:);
T_LGY100 = zeros(nx,nz);T_LGY100(:,:)=T_LG(:,ny/2,:);
v_X100 = zeros(ny,nz);v_X100(:,:)=v(nx/2,:,:);
v_Y100 = zeros(ny,nz);v_Y100(:,:)=v(:,ny/2,:);
figure(1)
contourf(yHF(2:end-1),z,T_LGX100(2:(ny-1),:)');caxis([10 20]);colorbar;
title('Initial T at x=20000 m');xlabel('x (m)');ylabel('Depth (m)');
figure(2)
contourf(xHF(2:end-1),z,T_LGY100(2:(nx-1),:)');caxis([10 20]);colorbar;
title('Initial T at y=20000 m');xlabel('y (m)');ylabel('Depth (m)');
figure(3)
pcolor(xHF,yHF,T_LG(:,:,5)'),shading interp;caxis([17.4 18.1]);colorbar;
title('Initial T at Z=-11.25 m');xlabel('x (m)');ylabel('y (m)');
figure(4)
pcolor(xCN,yHF,u(:,:,5)'),shading interp;caxis([-0.05 0.05]);colorbar;
title('Initial U at Z=-11.25 m');xlabel('x (m)');ylabel('y (m)');
figure(5)
pcolor(xHF,yCN,v(:,:,5)'),shading interp;caxis([-0.046 0.046]);colorbar;
title('Initial V at Z=-11.25 m');xlabel('x (m)');ylabel('y (m)');
figure(6)
pcolor(xHF,yCN,w(:,:,5)'),shading interp;caxis([-2E-4 2E-4]);colorbar;
title('Initial W at Z=-10 m');xlabel('x (m)');ylabel('y (m)');
figure(7)
pcolor(yCN(2:end-1),z,v_X100(2:(ny-1),:)');shading interp;
caxis([-0.069 0.069]);colorbar;
title('Initial V at x=20000 m');xlabel('x (m)');ylabel('Depth (m)');
figure(8)
pcolor(xHF(2:end-1),z,v_Y100(2:(nx-1),:)');shading interp;
caxis([-0.057 0.057]);colorbar;
title('Initial V at y=20000 m');xlabel('y (m)');ylabel('Depth (m)');
%Generate the inital velocities files uVelInit.bin and vVelInit.bin,
%and the initial temperature file tRefFile.bin.
fid=fopen('uVelInit.bin','w',ieee); fwrite(fid,u,accuracy); fclose(fid);
fid=fopen('vVelInit.bin','w',ieee); fwrite(fid,v,accuracy); fclose(fid);
fid=fopen('tRefFile.bin','w',ieee); fwrite(fid,T_LG,accuracy); fclose(fid);
```

B.2 Initialization in case I with non-constant $N(z)$

gendata.m is the Matlab code for Initialization in case I with non-constant $N(z)$ in Lagrangian formulation in section 4.4.1). rsh.m and Gbessel.m are the subfunctions used in gendata.m.

(a): gendata.m

```
ieee='b';accuracy='real*8';
nx=200;ny=200;nz=50;
A=5.0e-4;L=40000;H = 50;g = 9.8;rho0 = 999.8; alphaT = 2.0e-4; n=1;
cx=L/2;cy=L/2;
dx=L/nx;dy=L/ny;dz=H/nz;
xCN=0:dx:(L-dx);
yCN=0:dy:(L-dy);
xHF=dx/2:dx:L;
yHF=dy/2:dy:L;
z=-dz/2:(-dz):(-H);
G=numgrid('D',nx);

omega = 1.5045876E-4;
alpha = 2.600620346E-4;
f=1E-4; Tb = 10; Ts = 20; z0 = -15; d = 2;
h=zeros(nx,ny);rC = zeros(nx,ny);rU = zeros(nx,ny);rV = zeros(nx,ny);
thetaC = zeros(nx,ny);thetaU = zeros(nx,ny);thetaV = zeros(nx,ny);
urU = zeros(nx,ny,nz);urV = zeros(nx,ny,nz);
uthetaU = zeros(nx,ny,nz);uthetaV = zeros(nx,ny,nz);
u = zeros(nx,ny,nz);v = zeros(nx,ny,nz);
zstar = zeros(nx,ny,nz);T_LG = zeros(nx,ny,nz);

phi0=[0 1];zspan=[0 -H];
[zz,phi]=ode45('rsh',zspan,phi0,[],omega,alpha);
phiNormal = phi(:,1)/max(abs(phi(:,1)));
phiNormalDER = diff(phiNormal)./diff(zz);
phiNormalDER_ADD = [phiNormalDER' phiNormalDER(end)]';

N2Z = g*alphaT*((Ts-Tb)/(2*d))*(sech((z-z0)/d)).^2;
N1Z = (g*alphaT*((Ts-Tb)/(2*d))*(sech((z-z0)/d)).^2).^0.5;
Tbar = Tb + (Ts - Tb)/2*(1+tanh((z-z0)/d));
%Topography and initial height
for i=1:nx
    for j=1:ny
        if (G(ny+1-j,i)>0)
            rC(i,j) = sqrt((xHF(i)-cx)^2+(yHF(j)-cy)^2);
            rU(i,j) = sqrt((xCN(i)-cx)^2+(yHF(j)-cy)^2);
```

```matlab
            rV(i,j) = sqrt((xHF(i)-cx)^2+(yCN(j)-cy)^2);
            thetaC(i,j) = atan2(yHF(j)-cy,xHF(i)-cx);
            thetaU(i,j) = atan2(yHF(j)-cy,xCN(i)-cx);
            thetaV(i,j) = atan2(yCN(j)-cy,xHF(i)-cx);
            h(i,j)=-H;
        end
    end
end
fid=fopen('topog.box','w',ieee); fwrite(fid,h,accuracy); fclose(fid);
%Initial velocities
for i=1:nx
  disp(i)
  for j=1:ny
    for k=1:nz
        if (G(ny+1-j,i)>0)
            xi_temp = (1/omega)*A*besselj(n,alpha*rC(i,j))...
                        *cos(n*thetaC(i,j));
            z_temp = z(k);
            Q=min(z_temp+30,0):(-H/1000):max(z_temp-30,-H);
            interpQ = interp1(zz,phiNormal,Q);
            lenQ = length(Q);
            for iter = 1:lenQ
                if (abs(z_temp - Q(iter) - xi_temp*interpQ(iter))<5E-2)
                    zstar(i,j,k) = Q(iter);
                    break
                end
            end
        T_LG(i,j,k) = Tb + (Ts - Tb)/2*(1+tanh((zstar(i,j,k)-z0)/d));
        if (G(ny+1-j-1,i)>0 && G(ny+1-j+1,i)>0 ...
                && G(ny+1-j,i-1)>0 && G(ny+1-j,i+1)>0)
        inter_der_temp = interp1(zz,phiNormalDER_ADD,zstar(i,j,k));
        urU(i,j,k) =A/(rU(i,j)*omega*alpha^2)*((omega-f)*n...
            *besselj(n,alpha*rU(i,j)) - omega*alpha*rU(i,j)...
            *besselj(n+1,alpha*rU(i,j)))*sin(n*thetaU(i,j))...
            *inter_der_temp*(1+xi_temp*inter_der_temp);
        urV(i,j,k) = A/(rV(i,j)*omega*alpha^2)*((omega-f)*n...
            *besselj(n,alpha*rV(i,j)) - omega*alpha*rV(i,j)*...
            besselj(n+1,alpha*rV(i,j)))*sin(n*thetaU(i,j))*...
            inter_der_temp*(1+xi_temp*inter_der_temp);
        uthetaU(i,j,k) =A/(rU(i,j)*omega*alpha^2)*((omega-f)*n...
            *besselj(n,alpha*rU(i,j)) + f*alpha*rU(i,j)*...
            besselj(n+1,alpha*rU(i,j)))*cos(n*thetaU(i,j))...
            *inter_der_temp*(1+xi_temp*inter_der_temp);
        uthetaV(i,j,k) =A/(rV(i,j)*omega*alpha^2)*((omega-f)*n...
            *besselj(n,alpha*rV(i,j)) + f*alpha*rV(i,j)*...
```

```
                besselj(n+1,alpha*rV(i,j)))*cos(n*thetaU(i,j))...
                    *inter_der_temp*(1+xi_temp*inter_der_temp);
            u(i,j,k) = urU(i,j,k)*cos(thetaU(i,j))...
                        - uthetaU(i,j,k)*sin(thetaU(i,j));
            v(i,j,k) = urV(i,j,k)*sin(thetaV(i,j))...
                        + uthetaV(i,j,k)*cos(thetaV(i,j));
          elseif(G(ny+1-j-1,i)>0 && G(ny+1-j+1,i)>0 ...
                && G(ny+1-j,i-1)==0 && G(ny+1-j,i+1)>0)%left
            u(i,j,k) = 0;
          elseif(G(ny+1-j-1,i)>0 && G(ny+1-j+1,i)>0 ...
                && G(ny+1-j,i-1)>0 && G(ny+1-j,i+1)==0)%right
            u(i+1,j,k) = 0;
          elseif(G(ny+1-j-1,i)>0 && G(ny+1-j+1,i)==0 ...
                && G(ny+1-j,i-1)>0 && G(ny+1-j,i+1)>0)%down
            v(i,j,k) = 0;
          elseif((G(ny+1-j-1,i)==0 && G(ny+1-j+1,i)>0 ...
                && G(ny+1-j,i-1)<0 && G(ny+1-j,i+1)>0))%up
            v(i,j+1,k) = 0;
          end
          end
      end
  end
end
T_LGY100 = zeros(nx,nz);T_LGY100(:,:)=T_LG(:,ny/2,:);
T_LGX100 = zeros(ny,nz);T_LGX100(:,:)=T_LG(nx/2,:,:);
v_X100 = zeros(ny,nz);v_X100(:,:)=v(nx/2,:,:);
v_Y100 = zeros(ny,nz);v_Y100(:,:)=v(:,ny/2,:);
u_X100 = zeros(ny,nz);u_X100(:,:)=u(nx/2,:,:);
u_Y100 = zeros(ny,nz);u_Y100(:,:)=u(:,ny/2,:);
figure(1)
pcolor(yHF(2:end-1),z,T_LGX100(2:(ny-1),:)');shading interp;
caxis([10 20]);colorbar;
title('Initial T at x=20 km');xlabel('x (m)');ylabel('Depth (m)');
figure(2)
pcolor(xHF(2:end-1),z,T_LGY100(2:(nx-1),:)');shading interp;
caxis([10 20]);colorbar;
title('Initial T at y=20 km');xlabel('y (m)');ylabel('Depth (m)');
figure(3)
pcolor(xHF,yHF,T_LG(:,:,15)'),shading interp;caxis([12 19]);colorbar;
title('Initial T at Z=-10 m');xlabel('x (m)');ylabel('y (m)');
figure(4)
pcolor(xCN,yHF,u(:,:,10)'),shading interp;caxis([-0.037 0.037]);colorbar;
title('Initial U at Z=-10 m');xlabel('x (m)');ylabel('y (m)');
figure(5)
pcolor(xHF,yCN,v(:,:,10)'),shading interp;caxis([-0.027 0.043]);colorbar;
```

```
title('Initial V at Z=-15 m');xlabel('x (m)');ylabel('y (m)');
figure(6)
pcolor(yCN(2:end-1),z,v_X100(2:(ny-1),:)');shading interp;
caxis([-0.06 0.026]);colorbar;
title('Initial V at x=20 km');xlabel('x (m)');ylabel('Depth (m)');
figure(7)
pcolor(xHF(2:end-1),z,v_Y100(2:(nx-1),:)');shading interp;
caxis([-0.02 0.05]);colorbar;
title('Initial V at y=20 km');xlabel('y (m)');ylabel('Depth (m)');

fid=fopen('uVelInit.bin','w',ieee); fwrite(fid,u,accuracy); fclose(fid);
fid=fopen('vVelInit.bin','w',ieee); fwrite(fid,v,accuracy); fclose(fid);
fid=fopen('tRefFile.bin','w',ieee); fwrite(fid,T_LG,accuracy); fclose(fid);
```

(b): rsh.m

```
function rsh=rsh(z,phi,dummy,omega,alpha)
g=9.8;
alphaT=2.0e-4;
f=1.0e-4;
Ts=20; Tb=10;
d=2;z0=-15;
Nsquare = g*alphaT*((Ts-Tb)/(2*d))*(sech((z-z0)/d))^2;
rsh=[phi(2);
     -(( Nsquare - omega^2)/(omega^2-f^2))*alpha^2*phi(1)];
```

(c): Gbessel.m

```
function result = Gbessel(omega,alpha)
f=1.0e-4;
r0=20000.0;
result = f/r0*besselj(1,alpha*r0) - omega*alpha*(besselj(0,alpha*r0) ...
    - besselj(1,alpha*r0)/(alpha*r0));
```

117

Bibliography

A. Adcroft, C. Hill, and J. Marshall. Representation of topography by shaved cells in a height coordinate ocean model. *Mon. Wea. Rev.*, 125:2293–2315, 1997. 37

A. Adcroft, J. Campin, S. Dutkiewicz, C. Evangelinos, D. Ferreira, G. Forget, B. Fox-Kemper, P. Heimbach, C. Hill, E. Hill, H. Hill, O. Jahn, M. Losch, J. Marshall, G. Maze, D. Menemenlis, and A. Molod. *MITgcm Manual*. MIT Department of EAPS, November 2008. 37, 38

D. Beletsky, W. O'Connor, D. Schwab, and D. Dietrich. Numerical simulation of internal kelvin waves and coastal upwelling fronts. *J. Phys. Oceanogr.*, 27: 1197–1215, 1997. 3, 18, 103

J. Bell and B. Marcus. A second-order projection method for variable-density flows. *J. Comput. Phys.*, 101:334–348, 1992. 2

J. Bell, P. Collela, and H. Glaz. A second-order projection method for the incompressible navier-stokes equations. *J. Comput. Phys.*, 85:257–283, 1989a. 2

J. Bell, J. Solomon, and W. Szymczak. A second-order projection method for the incompressible navier-stokes equations on quadrilateral grids. In *AIAA 9th Computational Fluids Dynamics Conference*, American Institute of Aeronautics and Astronautics, Buffalo, New York, 1989b. 2

J. Bennett. a theory of large-amplitude kelvin waves. *J. Phys. Oceanogr.*, 3:57–60, 1973. 3

L. Boegman, G. Ivey, and J. Imberger. The degradation of internal waves in lakes with sloping topography. *Limnol. Oceanogr.*, 50(5):1620–1637, 2005. 3, 38

G. Csanady. Motion in a model great lake due to a suddenly imposed wind. *J. Geophys. Res.*, 73:6435–6447, 1968. 3, 18

B. Cushman-Roisin. *Introduction to Geophysical Fluid Dynamics*. Prentice Hall, 1994. 5, 7, 17

T. Davenport. Lakes: Physical processes. `http://www.waterencyclopedia.com/Hy-La/Lakes-Physical-Processes.html`, 2008. 1

A. de la Fuente, K. Shimizu, J. Imberger, and Y. Nino. The evolution of internal waves in a rotating stratified circular basin and the influence of weakly nonlinear and non-hydrostatic accelerations. Unpublished paper, 2008. iii, 4, 18, 72, 83, 95, 102

D. Farmer. Observation of long nonlinear waves in a lake. *J. Phys. Oceanogr.*, 8: 63–73, 1978. 3

A. Fedorov and W. Melville. Propagation and breaking of nonlinear kelvin wave. *J. Phys. Oceanogr.*, 25:2518–2531, 1995. 3

A. Gill. *Atmosphere-Ocean Dynamics.* Academic Press, 1982. 6

N. Heaps and A. Ramsbottom. Wind effects in the water in a narrow two layered lake. *Phil. Trans. R. Soc. Lond.*, A(259):391–439, 1966. 3

B. Hodges, J. Imberger, A. Saggio, and K. Winters. Modeling basin-scale internal waves in a stratified lake. *Limnol. Oceanogr.*, 45(7):1603–1620, 2000. 3, 103

E. Hopfinger. Turbulence in stratified fluids: a review. *J. Geophys. Res.*, 92:5287–5303, 1987. 3

D. Horn, J. Imberger, and G. Ivey. The degradation of long-scale interfacial gravity waves in lakes. *J. Fluid Mech.*, 434:181–207, 2001. 3, 38, 39

I. Imberger. Flux paths in a stratified lake: a review. In *Coastal and Estuarine Studies*, volume 41, pages 1–17. Amer. Geophys., 1998. 3

G. Ivey and J. Imberger. On the nature of turbulence in a stratified fluid, part 1: The energetics of mixing. *J. Phys. Oceanogr.*, 21:650–658, 1991. 3

P. Kundu and I. Cohen. *Fluid Mechanics.* Academic Press, third edition, 2004. 5, 12

K. Lamb. Numerical experiments of internal wave generation by strong tidal flow across a finite amplitude bank edge. *J. Geophys. Res.*, 99:843–864, 1994. 2

J. Marshall, A. Adcroft, C. Hill, L. Perelman, and C. Heisey. A finite-volume, incompressible navier stokes model for studies of the ocean on parallel computers. *J. Geophysical Res.*, 102(C3):5753–5766, 1997a. 37

J. Marshall, C. Hill, L. Perelman, and A. Adcroft. Hydrostatic, quasi-hydrostatic, and nonhydrostatic ocean modeling. *J. Geophysical Res.*, 102(C3):5733–5752, 1997b. 37

J. Marshall, A. Adcroft, J. Campin, C. Hill, and A. White. Atmosphere-ocean modeling exploiting fluid isomorphisms. *Mon. Wea. Rev.*, 132:2882–2894, 2004. 37

T. Maxworthy. Experiments on solitary internal kelvin waves. *J. Fluid Mech.*, 129: 365–383, 1983. 95

S. Monismith. Wind-forced motions in stratified lakes and their effect on mixed layer shear. *Limnol. Oceanogr.*, 30:771–783, 1985. 4

S. Monismith. An experimental study of the upwelling response of stratified reservoirs to surface shear stress. *J. Fluid Mech.*, 171:407–439, 1986. 3, 18

C. Mortimer. Water movement in lakes during summer stratification; evidence from the distribution of temperature in windermere. *Phil. R. Soc. Lond. Ser B.*, 236: 355–398, 1952. 4

M. Munnich, A. $\ddot{W}$Suest, and D. Imboden. Observation of the second vertical model of the initial seiche in and alphine lake. *Limnol. Oceanogr.*, 37:1705–1719, 1992. 4

I. Ostrovsky, Y. Yacobi, P. Walline, and I. Kalikhman. Seiche induced mixing: Its impact on lake productivity. *Deep-Sea Res.*, 41:323–332, 1996. 3

O. Phillips. *The dynamics of upper ocean.* Cambridge University Press, 1977. 3

R. Romea and J. Allen. The effect of friction and topography on coastal internal kelvin waves at low latitudes. *Tellus*, 36A:384–400, 1984. 3

R. Spigel and J. Imberger. The classification of mixed layer dynamics in lakes of small to medium size. *J. Phys. Oceanogr.*, 10:1104–1121, 1980. 3, 4

R. Stocker and I. Imberger. Energy partitioning and horizontal dispersion in a stratified rotating lake. *J. Phys. Oceanogr.*, 33:512–529, 2003. 4, 18

R. Thompson and J. Imberger. Response of a numerical model of a stratified lake to wind stress. In *Second Intl. Symp. on Stratified Flows, Trondheim*, Tadir, Trondheim, 1980. 38

S. Thorpe. Some dynamical effects of the sloping sides of lakes. In J. Imberger, editor, *Physical processes in lakes and oceans*, volume 54 of *Coastal and Estuarine Studies*. American Geophysical Union, 1998. 3

R. Wetzel. *Limnology: Lake and River Ecosystems.* Academic Press, third edition, 2001. 1